Development of optimised algorithms to calculate equation-of-state data in many-particle systems consisting of hard, anisotropic particles

Cumulative Dissertation

to
obtain the degree
doctor rerum naturalium (Dr. rer. nat.)
of the Faculty of Mathematics and Natural Sciences
at the University of Rostock

submitted by
Philipp Marienhagen, born on 08.10.1993 in Hamburg
from Rostock

Rostock, March 2022

https://doi.org/10.18453/rosdok_id00003901

Referees:
Prof. Dr. Joachim Wagner, Institut für Chemie, Universität Rostock
Prof. Dr. Karsten Meier, Institut für Thermodynamik, Helmut-Schmidt-Universität
Prof. Dr. Ronald Redmer, Institut für Physik, Universität Rostock

Date of submission: March 17, 2022
Date of scientific colloquium: June 28, 2022

This dissertation was researched and written in the time between October 2018 and March 2022 at the Department of Chemistry of the University of Rostock, at the chair of Physical Chemistry under the supervision of Prof. Dr. Joachim Wagner.

Zusammenfassung

In der vorliegenden Arbeit werden Zustandsgleichungen harter, anisotroper Partikel mit den komplementären Verfahren der Virialreihe und Monte Carlo Simulationen untersucht. Um Zugang zu Virialkoeffizienter höherer Ordnung zu erhalten, wird ein für harte Körper optimierter, auf Mayer Sampling basierender Algorithmus entwickelt. Hiermit werden Virialkoeffizienten der Ordnung drei bis acht von harten Linsen und harten, oblaten Rotationsellipsoiden in Abhängigkeit des Aspektverhältnisses berechnet. Die Methode wird auf Hypersphärozylinder im vierdimensionalen Raum erweitert, womit erstmals Virialkoeffizienten anisometrischer Objekte im vierdimensionalen Raum berechnet werden. Die Entwicklung eines Cluster Monte Carlo Algorithmus für Linsen und Rotationsellipsoide macht im (N, p, T)-Ensemble hochgenaue Zustandsdaten mit vergleichsweise geringem Rechenaufwand zugänglich. Die hiermit erhaltenen Zustandsdaten der isotropen Phase des Harte-Linsen-Fluids und des Harte-Ellipsoid-Fluids werden mit der Virialreihe verglichen und Korrekturen für Abbrucheffekte der Virialreihe analysiert. Obwohl sich die Zustandsdaten harter Linsen und harter Ellipsoide unterscheiden, kann eine in erster Näherung universelle Abhängigkeit vom Exzessanteil des Ausschlussvolumens beobachtet werden.

Abstract

In this work, equations of state of hard, anisotropic particles are studied employing the complementary methods of virial theory and Monte Carlo simulations. To calculate higher-order virial coefficients, an algorithm based on Mayer Sampling is developed and optimised for hard particles. Using this algorithm, third- to eighth-order virial coefficients of hard lenses and hard, oblate ellipsoids of revolution are calculated in dependence on their aspect ratio. The method is extended to hard hyperspherocylinders in the four-dimensional space to allow the calculation of virial coefficients of anisometric objects in the four-dimensional space for the first time. The development of a cluster Monte Carlo algorithm gives access to precise equation-of-state data for hard lenses and oblate ellipsoids of revolution in the (N, p, T) ensemble with comparatively small computational effort. The thus obtained equation-of-state data of the isotropic phases is compared to the virial series and truncation corrections for so-far-unknown virial coefficients are analysed. Although the equation-of-state data of the hard-lens fluid and hard-ellipsoid fluid differ, in first approximation a universal dependence on the excess part of the mutual excluded volume is observed.

Table of Contents

1 Introduction

1.1 Motivation

The investigation of colloidal systems has been a focus of both fundamental and applied science. With their widespread application in liquid-crystal displays (LCDs), pigments, cosmetics as well as areas where surface effects are relevant, colloids play an important role in everyday life.

In colloid science and statistical physics colloids often function as a model system for condensed matter. They are analogues of atoms or molecules at enlarged scales of space and time. Due to typical sizes comparable to optical wavelengths, quasielastic scattering methods using coherent laser light as a probe or confocal video microscopy are comparatively simple experiments to investigate structure-dynamics relations in these systems. The relevance of colloidal soft matter as a model is not limited to the mesoscale, but physical insights can be transferred to the molecular as well as the macroscopic scale of granular material.

A variety of colloidal geometries such as ellipsoids [1], spindles [2], rods [3], and even concave dumbbells [4] are known. In recent years, numerous unorthodox colloidal or nanocrystalline geometries, partly with tunable interactions, have been synthesised [5, 6] even exhibiting chiral phases [7]. A precondition for experimental studies promoting fundamental insights in many-particle physics is the availability of highly defined particles with small polydispersity and preferably tunable topological parameters.

To theoretically describe experimental findings with means of statistical mechanics, different potentials such as the solely repulsive hard-particle model have been suggested. At small distances, hard particle interactions have the dominant contribution to the potential of realistic systems leading to pronounced scientific interest.

Onsager predicted the existence of a nematic phase by solely theoretical means in a system of infinitely thin hard needles and platelets [8]. Sparked by this seminal work and the availability of computational methods, molecular simulations of hard-particle systems emerged [9, 10]. While the computationally less demanding study of two-dimensional ellipses of Vieillard-Baron in 1972 identified an isotropic-nematic phase transition [11], Frenkel followed with the identification of the same transition in a three-dimensional model fluid in 1982 [12]. This study on infinitely thin platelets thereby provided a qualitative confirmation of Onsager's prediction. Starting with ellipsoids of revolution, a variety of finite geometries were studied in the following years [13]. The model systems studied such as hard ellipsoids and hard spherocylinders thereby exhibit a complex phase behaviour including nematic, plastic crystalline, smectic, columnar and crystalline phases.

The crystallisation of the hard-sphere system was not immediately accepted in the scientific community [14]. After vast theoretical studies experimental methods were able to confirm this transition with some experiments even per-

formed in microgravity on space shuttles [15–17]. As an example for anisotropic experimental systems the group of Zumbusch has recently confirmed theoretical predictions for ellipsoidal particles [18–20].

The self-organisation and therewith related confinement of translational and orientational degrees of freedom for solely repulsive hard particles is only determined by entropy. The crystallisation of an entropy-driven system might first appear paradox, with a mere phenomenological perception of entropy. However, as can be seen from Boltzmann's pioneering equation $S = k_\mathrm{B} \ln \Omega$, originally written by Boltzmann as $S = k \log W$, the entropy is determined by the number of accessible microstates Ω. For hard particles, this is the accessible volume and purely entropic effects are hence also known as excluded-volume effects.

The virial series based on the N-particle excluded volume is therefore a complementary approach to investigate the equations of state of hard body systems in the isotropic phase. Virial coefficients have been calculated concurrently for a wide range of model systems.

1.2 Hard particles as a model system for condensed matter

The extensively studied hard-sphere model can easily be extended to anisotropic systems. Let $\underline{\mathbf{r}}_{ij}$ be the center-of-mass distance vector of two particles i and j with orientations defined by the unit vectors $\underline{\hat{\mathbf{u}}}_i$ and $\underline{\hat{\mathbf{u}}}_j$. Let further $r_c(\underline{\hat{\mathbf{r}}}_{ij})$ be the contact distance for a configuration in dependence on the particles orientations $\underline{\hat{\mathbf{u}}}_i$ and $\underline{\hat{\mathbf{u}}}_j$ and the direction $\underline{\hat{\mathbf{r}}}_{ij}$ of the distance vector. Assuming hard-body interaction, the interparticle potential reads as

$$U(\underline{\mathbf{r}}_{ij}, \underline{\hat{\mathbf{u}}}_i, \underline{\hat{\mathbf{u}}}_j) = \begin{cases} \infty & : \quad |\underline{\mathbf{r}}_{ij}| < r_c(\underline{\hat{\mathbf{r}}}_{ij}, \underline{\hat{\mathbf{u}}}_i, \underline{\hat{\mathbf{u}}}_j) \\ 0 & : \quad |\mathbf{r}_{ij}| \geq r_c(\underline{\hat{\mathbf{r}}}_{ij}, \underline{\hat{\mathbf{u}}}_i, \underline{\hat{\mathbf{u}}}_j) \end{cases} , \tag{1.1}$$

i.e., infinite in the case of an overlap and zero otherwise. Based on this model, the self-organisation of many-particle systems with various geometric shapes have been investigated. Introducing the aspect ratio ν defined as the quotient of the large to the short dimension, the impact of anisometry can be quantified.

In the following, research on many-particle systems consisting of hard ellipsoids of revolution, hard lenses, and hard spherocylinders, which all approach hard spheres in the limit $\nu \to 1$, are shortly revised.

In the first studies of the phase diagram of hard ellipsoids of revolution by Frenkel, Mulder, and McTague four distinct phases were identified depending on the aspect ratio and density, namely isotropic, nematic, plastic crystalline, and crystalline phases [13, 21, 22]. They subsequently published the equation-of-state data obtained and compared it to model predictions [22, 23]. After this pioneering work the focus switched to the isotropic-nematic phase transition incorporating Onsager-type theory and the extension to biaxial ellipsoids [24–29].

First equation-of-state data for hard spherocylinders was calculated by Vieil-

lard-Baron in 1974 [30]. Additional investigations complemented by virial coefficients were calculated in subsequent years [31–35]. There have also been detailed investigations of the phase diagram [33, 36–38].

Previous work on ellipsoids was based on the assumption that the maximum packing fraction of ellipsoids is equivalent to that of spheres with $\varphi_{\max} \approx 0.7405$ in an affine transformation of a FCC-crystal (stretched-FCC). Inspired by an experiment using M&M candies, Donev *et al.* showed in simulations that the maximum jammed packings of ellipsoids approach the maximum packing fraction of spheres surprisingly close. This was later experimentally confirmed by investigations with a granular model [39–41]. They suggested a novel crystalline structure with a maximum packing fraction as high as $\varphi_{\max} \approx 0.7707$ instead [40] sparking new interest in the uniaxial hard ellipsoid system.

Schilling *et al.* investigated the stability differences between Frenkel's SFCC phase and a simple monoclinic SM2 phase, generalised from the structures suggested by Donev *et al.* For highly anisotropic aspect ratios they identified a direct nematic-solid transition into the SM2 phase while moderately anisotropic ellipsoids exhibit a solid-solid phase transition from the SFCC phase to the SM2 phase [42, 43]. Using a replica-exchange algorithm, Odriozola and Co-Workers systematically determined the phase diagram of hard ellipsoids for ensembles of roughly 100 particles based on the SM2 structure [44–46]. Especially for moderate anisotropies, ellipsoids show a variety of phase transitions with increasing density from the isotropic phase via a plastic crystalline and SFCC phase to the close-packed SM2 phase. The phases isotropic, nematic, SM2 and plastic crystalline are visualised for small ensembles of oblate ellipsoids in Fig. 1.1.

Parallel to simulations, the calculation of virial coefficients of hard particles have been a research interest. Virial coefficients of hard spheres have been calculated up to order 12 [47, 48]. The virial coefficients B_i of hard ellipsoids have been calculated up to order $i = 8$ [49–52] where the eighth order virial coefficients are erroneous since only a subset of diagrams was considered [53].

The simple Carnahan-Starling equation of state [54] based on the approximation of virial coefficients is a widely used, fairly accurate description of the fluid phase of hard spheres. This approach has been generalised to anisotropic particles by Parsons [55] and modified by Vega [50]. Based only on the knowledge of low-order coefficients, Nezbeda, Boublík as well as Song and Mason suggested expressions to describe anisotropic particles equations of state [56–58] with increasing deviations for higher anisotropies.

Specific equation-of-state simulation studies of the isotropic phase of hard ellipsoids based on the pioneering work of Frenkel, Mulder, and McTague [22] were performed by McBride and Lomba in 2007 [59]. They complemented their data with Vega's virial coefficients and equation of state considering virial coefficients up to order $i = 5$.

Hard lenses have not been studied as extensively. The phase diagram was mapped out by Cinacchi and Torquato [60]. In the subsequent work, the focus was on metastable, glassy, and maximally random jammed packings of lenses

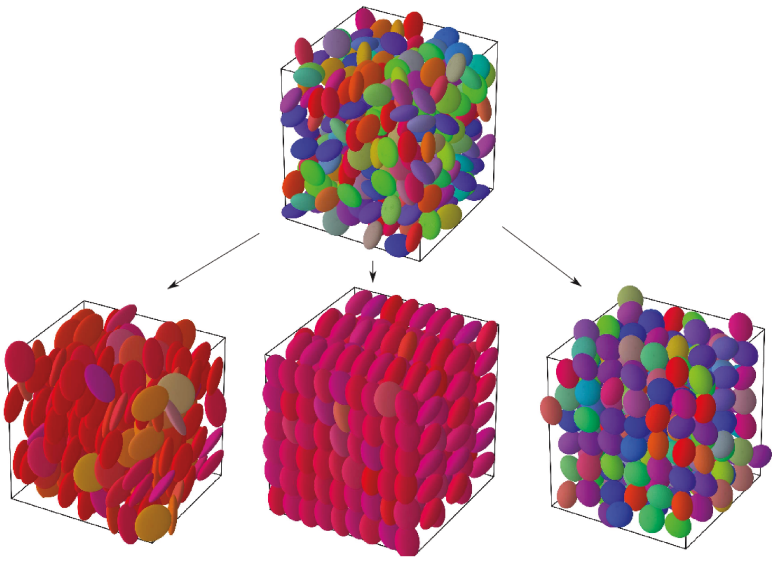

Fig. 1.1: Simulation snapshots of oblate ellipsoids of revolution of comparatively small ensembles in different phases exhibiting different length-scale dependent translational and orientational correlations. Orientations of the particles are visualised by different colours. The top box is an isotropic phase and can transition into three different phases depending on the anisotropy. Highly anisotropic particles form a nematic phase (bottom left), near-spherical ellipsoids form a plastic crystal (bottom right), while moderately anisotropic particles transition directly into the monoclinic SM2 crystal.

[61, 62]. Neither equations of state nor higher virial coefficients of lenses have been calculated, the second virial coefficient can be found in Ref. [63].

1.3 Concept and outline of this thesis

The aim of this dissertation is to investigate the equations of state of the isotropic phase of hard particles combining the virial series and numerical simulations based on an efficient cluster Monte Carlo algorithm. This methodology is applied to two different geometries to obtain information about the detailed influence of the particles' shape on the equation of state.

For the calculation of virial coefficients, the Mayer Sampling approach [64] is optimised specifically for hard-particle systems allowing the calculation of virial coefficients of order three to eight. Additionally, a complementary Monte Carlo simulation algorithm employing the cluster technique [65] is developed giving access to highly accurate equation-of-state data for hard particle systems from comparatively large ensembles of typically 1000 particles. Simultaneously, the phase boundaries of the isotropic phase are determined.

This allows a systematic investigation of the equations of state of hard oblate ellipsoids of revolution and hard lenses. By using two complementary methods,

a systematic investigation of the contribution of higher-order virial coefficients to the equation of state is possible. Additionally, insights may be gained on translational and orientational correlations in the isotropic phase of these many-particle systems.

The two geometries are thereby chosen as a similar phase behaviour has been observed [46, 60]. However, differences are expected as they differ significantly in their surface curvature. The lens has a two-dimensional singularity which has a significant impact on the second virial coefficient [63].

This thesis is thereby organised as follows: Chapter 1 contains a general motivation for the investigation of hard particles and an overview of the relevant research on this subject.

In Chapter 2, the theoretical background for the methods employed is explained. This includes Sec. 2.1 on the virial series, Sec. 2.2 on simulation techniques comprising the framework of statistical mechanics, the Metropolis approach [9] as well as its implications on the cluster technique followed by Sec. 2.3, showing general concepts to describe the equations of state of hard particles.

In Chapter 3, the results of three publications as first-author [66–68] as well as one publication as co-author [69] are compiled. First, in Sec. 3.1 the required geometry specific overlap and closest-surface-distance algorithms are presented and validated. Thereafter in Sec. 3.2 the refinement of the Mayer-Sampling algorithm is presented, the implementation is validated, and results are analysed. This is all based on Publication I. The method developed is extended to four-dimensional space for hard hyperspherocylinders and the results of the publication as co-author (Publication III) are presented in Sec. 3.2.5. Subsequently, in Sec. 3.3, the implemented cluster algorithm is explained and validated, followed by a presentation of the results based on the work in Publication II on oblate ellipsoids of revolution and Publication IV on lenses. Finally, the previous work on virial coefficients is combined with the simulation results in Sec. 3.4 allowing a detailed investigation of the equations of state of the shapes investigated combining the work in Publication I, Publication II, and Publication IV.

The main part of this thesis is concluded by Chapter 4 comprising a summary of the work presented and offering an outlook on possible future challenges. The corresponding publications including the supplemental material, if applicable, can be found in Sec. 5.

2 Theoretical Background

2.1 Calculation of virial coefficients

2.1.1 Virial series

The virial series expansion of the real gas factor Z in terms of the particle number density ϱ reads as

$$\begin{aligned} Z = \frac{p}{\varrho k_\mathrm{B} T} &= 1 + B_2 \varrho + B_3 \varrho^2 + ... \\ &= 1 + \sum_{i=2}^{\infty} B_i \, \varrho^{i-1} \end{aligned}$$

and was originally proposed by Kammerlingh-Onnes as a heuristic approach to describe experimental equation-of-state data with the expansion coefficients B_i named virial coefficients [70]. For hard particles, it is suitable to introduce reduced virial coefficients B_i^* and develop the virial series in terms of the volume fraction $\varphi = \varrho V_\mathrm{P}$ instead, which leads to the expression

$$Z = 1 + \sum_{i=2}^{\infty} B_i^* \, \varphi^{i-1} \quad \text{with} \quad B_i^* = \frac{B_i}{V_\mathrm{P}^{i-1}} \ , \tag{2.1}$$

V_P denoting the particle volume. Following the groundbreaking work of Mayer, Born was able to link the empiric virial coefficients with means of statistical thermodynamics to the configuration integral of the studied system and thus the potential of i-particle clusters [71, 72]. Therefore the virial coefficients can be interpreted as correction factors for i-particle interactions, for hard particles equivalent to the i-particle mutual excluded volume.

Assuming a pairwise additive many-particle potential

$$\mathcal{U}^{(i)} \approx \sum_i \sum_{j>i} \mathcal{U}_{ij} \tag{2.2}$$

which is exact for hard particles and defining the Mayer f-function

$$f_{ij} = \exp\left(-\beta \mathcal{U}_{ij}\right) - 1 \ , \tag{2.3}$$

the virial coefficients of order i can be calculated via

$$B_i = -\frac{i-1}{i!} \sum_{G \in \mathbb{M}_i^\mathrm{L}} S_G \tag{2.4}$$

as the summation over all integrals S_G of the product of Mayer f-functions of all Mayer diagrams G. In these Mayer diagrams G each vertex represents a particle and each edge a Mayer f-function while the set $\mathbb{M}_i^\mathrm{L}$ contains all

labelled, biconnected (non-separable) Mayer graphs of order i. In the case of hard particles, the Mayer f-function has the value -1 in the case of an overlap of two particles and zero if no overlap is present.

For the second to fourth virial coefficients, this leads to the expressions

$$B_2 = -\frac{1}{2}\int f_{12}\,\mathrm{d}\mathbf{r}_{12} = -\frac{1}{2}$$ (2.5a)

$$B_3 = -\frac{1}{3}\iint f_{12}f_{23}f_{13}\,\mathrm{d}\mathbf{r}_{12}\,\mathrm{d}\mathbf{r}_{13} = -\frac{1}{3}$$  (2.5b)

$B_4 = -\frac{1}{8}$ 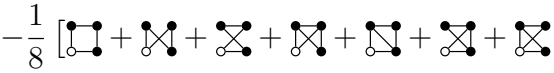 . (2.5c)

In the above representation, the first node is in the lower left corner and the graphs are labelled counterclockwise. The Mayer graphs of order i thereby contain between i and $i(i-1)/2$ edges, *i.e.* between 4 and 6 edges for the order $i = 4$. Beginning with order 5, graphs containing the same number of edges can be distinguished into different topological classes by comparing the bond order of the nodes and neighbouring nodes. For example, the two graphs

with five nodes and six bonds both have nodes with orders $(3, 3, 2, 2, 2)$. However, when considering the next neighbours they can be distinguished into the classes $(3_{322}, 3_{322}, 2_{33}, 2_{32}, 2_{32})$ and $(3_{222}, 3_{222}, 2_{33}, 2_{33}, 2_{33})$.

The total number of possible graphs with i vertices is given by $2^{i(i-1)/2}$, the set consisting of unconnected, singly-connected (articulated), and biconnected classes. With increasing i the amount of Mayer graphs and thus the integrand in the set $\mathbb{M}_i^{\mathrm{L}}$ rapidly increase with the set $\mathbb{M}_8^{\mathrm{L}}$ already containing 166 537 616 labelled Mayer graphs for order $i = 8$ (see Table 2.1). As a comparison the number of unlabelled Mayer diagrams $\mathbb{M}_i^{\mathrm{U}}$ are also listed, reduced by the amount of permutations of topologically equivalent diagrams.

This number can be reduced for $i \geq 4$ by using the reformulation of Ree and Hoover (see Table 2.1) [73–75]. An additional factor $e_{ij} - f_{ij} = 1$ is introduced so that all graphs are fully connected, whereby roughly two thirds cancel out. The obtained Ree-Hoover reformulation

$$B_i = -\frac{i-1}{i!}\sum_{G\in\mathbb{R}_i^{\mathrm{L}}} c_G S_G \tag{2.6}$$

is a summation over the set of integrated Ree-Hoover graphs $\mathbb{R}_i^{\mathrm{L}}$ weighted by the factors c_G called Ree-Hoover star contents. For the order $i = 4$ the equation

$B_4 = -\frac{1}{8}\Big[-2$ 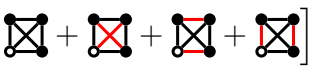 (2.7)

Table 2.1: Number of unlabelled and labelled Mayer and Ree-Hoover diagrams in the sets $\mathbb{M}_i^{\mathrm{U}}$, $\mathbb{M}_i^{\mathrm{L}}$, $\mathbb{R}_i^{\mathrm{U}}$ and $\mathbb{R}_i^{\mathrm{L}}$ respectively (numbers from Ref. [53]).

	Mayer		Ree and Hoover	
i	unlabelled	labelled	unlabelled	labelled
2	1	1	1	1
3	1	1	1	1
4	3	10	2	4
5	10	238	5	68
6	56	11 368	23	3 053
7	468	1 014 888	171	297 171
8	7 123	166 537 616	2 606	56 671 216

results where the red lines represent e-bonds.

For hard particles, the product of a Ree-Hoover diagrams' integrand is only non-zero if all multipliers are non-zero and therefore all f-bonded particles overlap ($f_{ij} = -1$) and all e-bonded particles do not ($e_{ij} = 1$). As a consequence, for any given configuration, only a single graph has a non-zero contribution to the integrand of $c_G\,(-1)^{n_f}$, the exponent n_f being the number of f-Bonds [76].

Hellmann and Bich introduced a variant using hypertrees which intrinsically considers nonadditive many-body potentials and additionally results in fewer diagrams for orders $i \geq 6$ than the approach of Ree and Hoover [77]. For hard particles, however, several diagrams contribute to the integrand and thus the method of Ree and Hoover is the preferable approach. For virial coefficients of order $i > 10$ the method of Wheatley has to be considered [48].

2.1.2 Analytic calculation of virial coefficients

Calculating virial coefficients analytically has been a topic of profound scientific interest in the past with the fourth virial coefficient of hard spheres already being calculated by van Laar in 1899 [78]. In recent years, the virial coefficients up to order B_4 have additionally been calculated in up to twelve dimensions [79, 80].

For hard, convex particles, Isihara and Hadwiger could independently show, that the second virial coefficient can be calculated via

$$B_2^* = 1 + \frac{S_{\mathrm{P}}\tilde{R}_{\mathrm{P}}}{V_{\mathrm{P}}} \tag{2.8}$$

from the particles geometric measures surface area S_{P}, volume V_{P} and mean radius of curvature $\tilde{R}_{\mathrm{P}}$ [81–84]. Herold, Hellmann, and Wagner utilised this approach to investigate the influence of one-dimensional and two-dimensional singularities of the surface curvature on solids of revolution such as ellipsoids,

lenses, spindles, spherocylinders, cylinders, and double cones [63].

2.1.3 Numerical methods to calculate virial coefficients

The use of Monte Carlo methods for the calculation of virial coefficients of hard disks and spheres up to order five was already implemented by Metropolis *et al.* as well as Rosenbluth and Rosenbluth in the early 1950s [9, 10]. Although biased MC had previously been utilised to calculate virial coefficients [85], the umbrella-sampling approach of Singh and Kofke called Mayer Sampling, was a major breakthrough in the numerical calculation of virial coefficients [64].

A biased sampling distribution π is introduced requiring the simultaneous calculation of a reference system so that the virial coefficient of interest

$$B_i = I_{i,\mathrm{ref}} \frac{\langle \gamma / \pi \rangle_\pi}{\langle \gamma_{\mathrm{ref}} / \pi \rangle_\pi} \tag{2.9}$$

is determined from the ratio of the simulation averages of the integrand of interest γ and reference integrand γ_{ref}, scaled by the integral of the reference system $I_{i,\mathrm{ref}}$. The acceptance of a trial configuration is thereby determined by the acceptance criteria $\min(1, \pi_{\mathrm{new}}/\pi_{\mathrm{old}})$.

While Singh and Kofke only used the ring cluster of hard spheres as a reference integrand to calculate the virial coefficients of the Lennard-Jones model as well as the SPCE water model, Jäger *et al.* preferred to use all hard-sphere clusters in their *ab initio* argon study [64, 86]. For higher-dimensional geometries other techniques are viable [76]. In principle, any reference integral can be used as long as the phase space of the reference is a subset of the phase space of the system of interest [87].

The Mayer sampling method is especially valuable for complex integrands and therefore higher-order virial coefficients.

2.2 Simulation algorithms to calculate equations of state

2.2.1 Overview of applicable simulation algorithms

Molecular dynamics simulations as a standard technique to investigate molecular systems numerically integrate the deterministic equations of motion, usually based on a force field of the system. This classically time-driven standard has problems with accuracy and efficiency for hard particle systems [88], which can be circumvented by utilizing an event-driven approach that for hard particles is on the basis of particle collisions. These event-driven molecular simulations can be extended to anisotropic systems as shown by Donev and Co-Workers [88, 89], the collision algorithms, however, have to additionally deal with the geometry-dependent angular momentum.

The alternative approach of Monte Carlo simulations is based on the ergodic hypothesis by calculating time averages via ensemble averages. This limits the investigation to static averages with dynamic properties such as diffusion

coefficients out of reach. Standard Monte Carlo schemes generate random configurations according to a probability density based on the investigated phase space and accept these with a specific acceptance probability.

A variety of refined Monte Carlo approaches have been suggested over the years all with the aim of a more efficient exploration of phase space. Replica exchange MC, for instance, samples numerous replicas at different temperatures or pressures allowing swap trials between the subsystems. This approach has been applied to hard-sphere and hard-ellipsoid systems [44–46, 90].

Alternatively, a bias can be introduced so that larger differences exist between trial moves leading to a better exploration of phase space. Different cluster algorithms have thereby been proposed such as multiparticle moves [91] or the extension to cluster formation during volume fluctuations [65]. Almarza used this method to investigate equations of state of crystalline hard spheres [65], a generalisation to anisotropic hard rhombic platelets has been performed to explore the phase behaviour of such systems [92].

Adopting an event-driven approach in a Monte Carlo scheme, hard disks and spheres have been investigated utilizing event-chain Monte Carlo simulations [93–95]. Both molecular dynamics simulations and stochastic Monte Carlo steps can also be coupled to Hybrid Monte Carlo schemes, which have been extended to event-driven algorithms [96].

There are generally two fundamental options to start a simulation. One option is to initialize the simulation from a specific crystal and expand the box to the equilibrium pressure. The ensemble can possibly recrystallise into a preferable structure if the barriers of the potential energy surface allow. Alternatively, a random disordered low-density configuration can be compressed to equilibrium. For small systems under certain circumstances a crystallisation may occur (see Ref. [61]), commonly the systems of hard particles reach a metastable branch which can be compressed up to the maximum random closed packing density depending on the speed of compression.

There are a variety of methods to predict crystal structures from first principles [97]. Many have limitations when investigating hard particles. For hard particles, the densest packed crystal is the most stable phase at infinite pressure, at finite pressure, this may deviate. The identification of such densest packings is possible using very small ensembles in the floppy-box Monte Carlo algorithm [98]. However, severe distortions of the simulation box occur which have to be compensated by using lattice reduction techniques [99].

2.2.2 Canonical (N, V, T) ensemble

To increase the readability in the following sections, the theory is formulated for spherically symmetric systems which can be systematically extended to anisotropic systems by additionally introducing angular coordinates. In statistical mechanics, a variety of statistical ensembles exist. They allow the calculation of thermodynamic properties of a macroscopic system from the microscopic states of a model system via a thermodynamic potential. In the

standard canonical (N, V, T) ensemble, all possible energetic states of the set are represented by subsystems with N particles in a fixed volume V in thermodynamic equilibrium with an external reservoir (heat bath) at fixed temperature T making the ensemble a closed system.

The classical statistical mechanical definition of the canonical partition function $Q_{N,V,T}$ of N indistinguishable particles as

$$Q_{N,V,T} = \frac{1}{N! h^{3N}} \iint \mathrm{e}^{-\beta \mathcal{H}\left(\underline{\mathbf{r}}^N, \underline{\mathbf{p}}^N\right)} \, \mathrm{d}\underline{\mathbf{r}}^N \mathrm{d}\underline{\mathbf{p}}^N \tag{2.10}$$

depends on the Hamiltonian $\mathcal{H}\left(\underline{\mathbf{r}}^N, \underline{\mathbf{p}}^N\right)$ integrating over the phase space of N particle positions $\underline{\mathbf{r}}^N$ and momenta $\underline{\mathbf{p}}^N$. The thermodynamic potential of the canonical ensemble is thereby defined as $F = -\beta^{-1} \ln Q_{N,V,T}$ with the independent variables N, V, and T. The free energy F is given in units of thermal energy $\beta^{-1} = k_\mathrm{B} T$. Powers of Planck's constant h guarantee that the partition function is dimensionless and thus allows a transition to the corresponding quantum statistic connecting quantum states and classical phase space.

The Hamiltonian $\mathcal{H}\left(\underline{\mathbf{r}}^N, \underline{\mathbf{p}}^N\right) = \mathcal{U}\left(\underline{\mathbf{r}}^N\right) + \mathcal{K}\left(\underline{\mathbf{p}}^N\right)$ can be separated into contributions of the kinetic energy $\mathcal{K}$ and potential energy $\mathcal{U}$ allowing an integration over the momenta if the potential energy is only determined by the particle positions. The integration over the momenta results in a factor $(2\pi m k_\mathrm{B} T)^{1/2}$ per particle and translational degree of freedom. By introducing the thermal de Broglie wavelength $\Lambda = h\,(2\pi m k_\mathrm{B} T)^{-1/2}$, the canonical partition function can be written as

$$Q_{N,V,T} = \frac{1}{N! \Lambda^{3N}} \int \mathrm{e}^{-\beta \mathcal{U}\left(\underline{\mathbf{r}}^N\right)} \, \mathrm{d}\underline{\mathbf{r}}^N \tag{2.11}$$

with the canonical configuration integral

$$Z_{N,V,T} = \int \mathrm{e}^{-\beta \mathcal{U}\left(\underline{\mathbf{r}}^N\right)} \, \mathrm{d}\underline{\mathbf{r}}^N \ . \tag{2.12}$$

On this basis, the normalised probability of a specific configuration $\left(\underline{\mathbf{r}}^N\right)$ can be written as

$$p_{N,V,T}\left(\underline{\mathbf{r}}^N\right) = \frac{e^{-\beta \mathcal{U}\left(\underline{\mathbf{r}}^N\right)}}{Z_{N,V,T}} \tag{2.13}$$

leading to the expression

$$\langle A \rangle = \frac{\int A\left(\underline{\mathbf{r}}^N\right) e^{-\beta \mathcal{U}\left(\underline{\mathbf{r}}^N\right)} \mathrm{d}\underline{\mathbf{r}}^N}{Z_{N,V,T}} \tag{2.14}$$

for the canonical average of an arbitrary observable A.

2.2.3 Isobaric-isothermal (N, p, T) ensemble

Guggenheim [100] originally introduced the isobaric and isothermal (N, p, T) ensemble with the independent variables N, p, and T and the Gibbs free energy $G = -\beta^{-1} \ln Q_{N,p,T}$ as the thermodynamic potential. The closed ensemble thereby consists of N-particle subsystems with fixed pressure p and fixed temperature T. As the volume fluctuates, the heat-conducting walls of the subsystems are flexible.

The analogue partition function $Q_{N,p,T}$ in a fixed laboratory system, defined by

$$\begin{aligned} Q_{N,p,T} &= \frac{1}{N! h^{3N}} \int \frac{1}{V} \iint \mathrm{e}^{-\beta \mathcal{H}\left(\underline{\mathbf{r}}^N, \underline{\mathbf{p}}^N\right)} \, \mathrm{d}\underline{\mathbf{r}}^N \mathrm{d}\underline{\mathbf{p}}^N \, \mathrm{e}^{-\beta p V} \, \mathrm{d}V \\ &= \frac{1}{N! \Lambda^{3N}} \iint \frac{1}{V} \mathrm{e}^{-\beta \left[\mathcal{U}\left(\underline{\mathbf{r}}^N\right) + pV\right]} \, \mathrm{d}\underline{\mathbf{r}}^N \mathrm{d}V \, , \end{aligned} \tag{2.15}$$

of N particles includes an additional volume integration. The argument of the exponential is thereby the reduced enthalpy. The volume scale V^{-1} guarantees a dimensionless partition function again enabling the transition to the corresponding quantum statistic. A historic overview of the partly controversial discussion of the volume scale can be found in Refs. [101, 102].

One can define an analogue configuration integral

$$Z_{N,p,T} = \iint V^{N-1} \mathrm{e}^{-\beta \left[\mathcal{U}\left(\underline{\mathbf{s}}^N\right) + pV\right]} \, \mathrm{d}\underline{\mathbf{s}}^N \, \mathrm{d}V \tag{2.16}$$

introducing the scaled coordinates $\mathrm{d}\underline{\mathbf{s}} = \mathrm{d}\underline{\mathbf{r}}/V$. The normalised probability of a specific configuration $\left(\underline{\mathbf{s}}^N, V\right)$ then reads as

$$p_{N,p,T}\left(\underline{\mathbf{s}}^N, V\right) = \frac{V^{N-1}}{Z_{N,p,T}} \mathrm{e}^{-\beta \left[\mathcal{U}\left(\underline{\mathbf{s}}^N\right) + pV\right]} \tag{2.17}$$

in the isobaric-isotherm ensemble.

2.2.4 Metropolis Monte Carlo algorithm

The calculation of thermodynamic properties according to Eq. (2.14) for a spherically symmetric system requires a $3\,(N-1)$-dimensional integration and is therefore already highly challenging for tiny particle numbers with conventional integration schemes. In general, only specific observables are of interest and not the actual value of the partition function, configuration integral, or probability distribution.

Importance sampling Monte Carlo methods provide an alternative approach preferably evaluating the integrand in regions of phase space with a significant

contribution by using a sampling distribution that ideally resembles the actual integrand thereby evaluating each state with the corresponding probability.

The acclaimed Metropolis-Hastings algorithm is based on this idea generating a trial sequence named Markov chain, which has to fulfil two conditions. Firstly, each trial has to belong to a finite set of outcomes, and secondly each trial may only depend on the outcome of the previous trial [103]. As a consequence, the initial configuration is irrelevant. A sufficient but not necessary condition which complies with these requirements is termed detailed balance: Let $\mathcal{N}(x)$ be the probability of finding a system in the configuration x and $\pi(x'|x)$ that of transitioning from state x to state x'. In equilibrium, the number of transitions from state x to x' shall be equal to the number of reverse transitions. The condition of detailed balance then reads

$$\mathcal{N}(x)\pi(x'|x) = \mathcal{N}(x')\pi(x|x') \ . \tag{2.18}$$

This condition thereby preserves the correct distribution of states once equilibrium is reached. The transition probability $\pi(x'|x)$ depends on the proposal probability $\omega(x'|x)$ for a transition from x to x' and the acceptance of that trial $P_{\mathrm{Acc}}(x'|x)$. Considering the transition probability $\pi(x'|x) = \omega(x'|x)P_{\mathrm{Acc}}(x'|x)$ leads to

$$\mathcal{N}(x)\omega(x'|x)P_{\mathrm{Acc}}(x'|x) = \mathcal{N}(x')\omega(x|x')P_{\mathrm{Acc}}(x|x') \tag{2.19}$$

for the condition of detailed balance. In the original Metropolis algorithm, the probability of a proposed trial is independent of the configuration and thus ω is symmetric with $\omega(x'|x) = \omega(x|x')$. Additionally with Eq. (2.13)

$$\frac{P_{\mathrm{Acc}}(x'|x)}{P_{\mathrm{Acc}}(x|x')} = \frac{\mathcal{N}(x')}{\mathcal{N}(x)} = \exp\left\{-\beta\left[\mathcal{U}(x') - \mathcal{U}(x)\right]\right\} \tag{2.20}$$

results for the acceptance criteria, only dependent on the relative probability between the states and not the absolute probability requiring the configuration integral. Metropolis *et al.* chose the acceptance ratio as

$$P_{\mathrm{Acc}}(\underline{\mathbf{r}}'^N|\underline{\mathbf{r}}^N) = \min\left[1, \exp\left\{-\beta\left[\mathcal{U}(\underline{\mathbf{r}}'^N) - \mathcal{U}(\underline{\mathbf{r}}^N)\right]\right\}\right] \tag{2.21}$$

in the canonical ensemble fulfilling the criteria obtained in Eq. (2.20) [9].

Standard simulations in the canonical ensemble generate these trial configurations via random particle translation or rotation attempts with the maximum displacement or rotation chosen to lead to an acceptance ratio of roughly 50 %. As for hard particle systems the potential energy can only be infinite or zero, overlap-free trial configurations are always accepted while the presence of an overlap leads to a rejection of the proposed configuration.

In the isobaric-isothermal ensemble, additional volume-change attempts have to be introduced to additionally sample the volume of the system. On the basis

of the prior probability distribution (see Eq. (2.17)) the acceptance criteria

$$P_{\mathrm{Acc}}(V'|V,\underline{\mathbf{s}}^N) = \min\left[1, \left(\frac{V'}{V}\right)^{N-1} \frac{\exp\left\{-\beta\left[\mathcal{U}(V',\underline{\mathbf{s}}^N)+pV'\right]\right\}}{\exp\left\{-\beta\left[\mathcal{U}(V,\underline{\mathbf{s}}^N)+pV\right]\right\}}\right] \tag{2.22}$$

for a volume change from V to V' can be obtained for the configuration with volume independent reduced coordinates $(\underline{\mathbf{s}}^N)$. The basic algorithms for Monte Carlo simulations in the isobaric-isothermal ensemble can be found in the monographs of Frenkel and Smit as well as Allen and Tildesley [103, 104].

2.2.5 Cluster Monte Carlo method

For volume changes in hard particle systems, the volume change acceptance of a compression trial is limited by the particles with closest inter-particle distances. Almarza [65] adopted the cluster algorithm of Swendsen and Wang [105], introduced to investigate large near-critical systems, for volume changes of a hard-sphere system. Before volume fluctuations, random rigid pseudo-molecules are formed consisting of especially close particles. Instead of scaling the particles' centres of mass, the center-of-mass position of the cluster is rescaled keeping the particle distances within the cluster constant. This biased MC variant thereby increases the accepted mean volume change $\langle|V'-V|\rangle$ leading to a better exploration of phase space.

A cluster consists of all particles that are directly or indirectly linked via bonds generated by a distance-dependent bond probability function b. Generalised by Tasios [92] from the original center-of-mass distance r_{ij} to the closest surface distance σ_{ij} reading as

$$b(\sigma_{ij}) = \begin{cases} 1-\left(\frac{\sigma_{ij}}{\delta}\right)^2 & : \quad \sigma_{ij} < \delta \\ 0 & : \quad \sigma_{ij} \geq \delta \end{cases}, \tag{2.23}$$

the extension to anisotropic particles is possible. Although this choice for $b(\sigma_{ij})$ is arbitrary, it ensures via the cutoff distance δ that no bonds are generated for distances $\sigma_{ij} \geq \delta$ while simultaneously weighting the surface distance increasing the probability of forming bonds at small distances. The average cluster size can be adjusted during the equilibration phase via the cutoff distance δ.

As the acceptance probability of a volume change trial is directly dependent on the choice of clusters, an additional factor has to be introduced to fulfil the condition of detailed balance (compare Eq. (2.18)). If (χ_c) is a specific cluster realisation defined by the cluster center of mass and the particles relative position thereto, $\omega\left(\chi_c|\underline{\mathbf{s}}'^N, V'\right)$ the probability of choosing the specific cluster realisation from the reduced coordinates $\underline{\mathbf{s}}'^N$ in volume V' and $\omega\left(\chi_c|\underline{\mathbf{s}}^N, V\right)$ the corresponding probability for the same cluster from the coordinates $\underline{\mathbf{s}}^N$ in

volume V, the condition of detailed balance can be written as

$$\frac{P_{\mathrm{Acc}}(V'|V,\chi_c)}{P_{\mathrm{Acc}}(V\ |V',\chi_c)} = \frac{\mathcal{N}(V'|\underline{\mathbf{s}}'^N)\,\omega_c(\chi_c|\underline{\mathbf{s}}'^N,V')\,\omega_V(V|V')}{\mathcal{N}(V|\underline{\mathbf{s}}^N)\,\omega_c(\chi_c|\underline{\mathbf{s}}^N,V)\,\omega_V(V'|V)}\ . \tag{2.24}$$

Again imposing a symmetric proposal probability $\omega_V(V'|V) = \omega_V(V|V')$, the acceptance probability can be obtained as

$$P_{\mathrm{Acc}}(V'|V,\chi_c) = \min\left[1, \left(\frac{V'}{V}\right)^{\tilde{N}-1} \frac{\exp\left\{-\beta\left[\mathcal{U}(\underline{\mathbf{s}}'^N,V')+pV'\right]\right\}}{\exp\left\{-\beta\left[\mathcal{U}(\underline{\mathbf{s}}^N,V)+pV\right]\right\}} \frac{\omega_c(\chi_c|\underline{\mathbf{s}}'^N)}{\omega_c(\chi_c|\underline{\mathbf{s}}^N)}\right] \tag{2.25}$$

for a volume change allowing cluster formation within the Metropolis-Hastings scheme. The apparent number of particles $\tilde{N} \leq N$ is thereby the sum of remaining single particles and clusters in the configuration χ_c. The cluster probability ratio of Eq. (2.25)

$$\frac{\omega_c(\chi_c|\underline{\mathbf{s}}'^N,V')}{\omega_c(\chi_c|\underline{\mathbf{s}}^N,V)} = \prod_{[ij]} \frac{1-b(\sigma'_{ij})}{1-b(\sigma_{ij})} \tag{2.26}$$

can be calculated as the product over all particle permutations $[ij]$ where i and j belong to different clusters [65]. Due to the definition of the bond probability [Eq. (2.23)] only distances $\sigma_{ij} < \delta$ can differ from one, *i.e.* have an effect on the ratio. To increase the numerical stability for larger particle numbers it is advisable to calculate the sum of the ratios' logarithms instead.

Periodic boundary conditions are a useful tool to minimize finite-size effects as well as to avoid surface effects when simulating bulk phases. In this method, the simulation box is treated as a primitive cell replicated by elementary translations onto an infinite lattice. Particles that leave a cell are replaced by their periodic images on the opposite side. However, by allowing cluster formation, a particle may be linked to its periodic image via a chain of bonds. This cluster percolation makes it impossible to rescale the particle coordinates keeping the intra-cluster distances constant and the size of the cluster is infinite. Such configurations have to therefore be rejected. The cutoff distance should be chosen small enough so that rejections due to cluster percolation are limited. The cluster formation routine also has to consider the minimum image convention imposed by periodic boundary conditions.

2.2.6 Technical details

The stability of simulated crystal structures in the isobaric-isothermal ensemble is highly dependent on the simulation box which can stabilize an unfavourable crystalline structure by external tension. To reduce the impact of this effect, additional deformations of the simulation box can be introduced, commonly performed at constant volume for standard acceptance criteria.

A useful approach when using reduced coordinates $\underline{\mathbf{r}}_i = \mathbf{H}.\underline{\mathbf{s}}_i$ is choosing an uppertriangular transformation matrix $\mathbf{H}$. In standard volume fluctuations, the rescaling of the coordinates can thereby be avoided. Fluctuations of the diagonal elements lead to rectangular cuboids while fluctuations of the off-diagonal elements allow nonorthogonal parallelepipeds such as triclinic structures. The volume of the simulation box can be obtained via the parallelepipedal product $V = ||\mathbf{H}||$. For fluid phases, a cubic simulation box can be used based on matrix identity $\mathbf{I}$ as $\mathbf{H} = V^{1/3}\mathbf{I}$.

The procedure for periodic boundary conditions in nonorthogonal simulation boxes is identical when using scaled coordinates $\underline{\mathbf{s}}_i$, the cutoff, however, has to be chosen smaller than half the shortest perpendicular width of the simulation box to fulfil the minimum image convention. This guarantees that only one image is considered in particle interactions and observables determined thereby.

Using a start configuration, a simulation is initialised by an equilibration phase. Therein variables and simulation parameters such as maximal displacements may be adjusted. Once equilibrium is reached and the acceptance criteria are adjusted to the target values, a production phase is started during which the observables of interest are calculated. It is important to note that when rejecting a trial configuration, the initial configuration still contributes to the ensemble average.

The computational expense in dependence on the number of particles N scales with $N(N-1)/2$. The numerical effort can be reduced substantially by calculating Verlet neighbour lists or utilizing a cell method [106, 107].

In principle, phase transitions can be calculated from energy differences to reference systems such as the ideal Einstein crystal [108]. However, possible crystal structures often exhibit small energy differences, have pronounced size effects, and rely on the correct prediction of the crystal parameters. Phase transitions are hence often calculated indirectly by monitoring specific order parameters during compression or expansion simulations.

The orientational correlation of nematic phases can be identified using the nematic order parameter

$$S_2 = \left\langle \frac{1}{2}\left(3x_i - 1\right) \right\rangle \tag{2.27}$$

averaging over the inner product x_i of the particle director and nematic director. Different crystal structures can be distinguished by looking at local bond order parameters Q_l of order l. These are averages of spherical harmonics $Y_{l,m}(\theta, \phi)$ of the center-of-mass distance-vector relative to the laboratory coordinate system (θ, ϕ) defined by

$$Q_6 = \left(\frac{4\pi}{2l+1} \sum_{m=-l}^{l} | \langle Y_{l,m}(\theta, \phi) \rangle |^2 \right)^{1/2} \tag{2.28}$$

considering only distances within a defined cutoff [109]. These parameters can be complemented by pair distribution functions and snapshots of single configurations.

2.3 Generalised equations of state

Although the infinite virial series is exact for gases and overcritical fluids, in practice, the accessible virial coefficients are limited and thus truncation effects arise. Carnahan and Starling [54] suggested approximating the virial coefficients of hard spheres via the integer sequence

$$B_i^{*,\mathrm{CS}} \approx i^2 + i - 2 \tag{2.29}$$

for $i \geq 2$, which for the until then known coefficients of order $i = 5$ leads to the approximation

$$\begin{aligned} Z &= 1 + 4\varphi + 10\varphi^2 + 18.3648\varphi^3 + 28.2245\varphi^4 + 39.8151\varphi^5 + ... && (2.30)\\ &\approx 1 + 4\varphi + 10\varphi^2 + 18\varphi^3 + 28\varphi^4 + 40\varphi^5 + ... \ . && (2.31) \end{aligned}$$

As higher-order coefficients became available, the validity of this approximation was confirmed. Using this approximation the closed expression

$$\begin{aligned} Z^{\mathrm{CS}} &\approx 1 + \sum_{i=2}^{\infty} \left(i^2 + i - 2\right) \varphi^{i-1} && (2.32)\\ &= 1 + \frac{4\varphi - 2\varphi^2}{(1-\varphi)^3} = \frac{1 + \varphi + \varphi^2 - \varphi^3}{(1-\varphi)^3} && (2.33) \end{aligned}$$

can be obtained for the geometric series under the condition $0 \leq \varphi < 1$. The resulting equation of state describes the fluid of hard spheres up to the phase boundary with an accuracy of roughly 1 %. This expression has been modified to allow a better description of the available data [110].

A large variety of expressions have been postulated to describe the hard-sphere real gas factor, a good overview can be found in Ref. [111]. A correlation based on highly accurate simulation data using up to nine parameters was suggested by Kolafa *et al.* [112] and is used as a reference in the presented work.

Concurrent to the description of the hard-sphere system, anisotropic hard systems have been investigated. A simple concept of describing hard anisotropic particles equation of state was suggested by Parsons, which scales the Carnahan-Starling coefficients according to

$$Z = 1 + \frac{B_2^*}{4} \frac{4\varphi - 2\varphi^2}{(1-\varphi)^3} \tag{2.34}$$

by the ratio of reduced second virial coefficients of the investigated system B_2^*

and that of hard spheres $B_2^{*,(\mathrm{HS})} = 4$ [55]. This approach is widely used in classical density functional theory [113, 114]. Vega modified this approach by considering all available virial coefficients up to order $i = 5$ [50]. Generalised for $i_{\max}$ known coefficients, the real gas factor

$$Z = 1 + \sum_{i=2}^{i_{\max}} B_i^* \, \varphi^{i-1} + \frac{B_2^*}{B_2^{*,(\mathrm{HS})}} \sum_{i=i_{\max}+1}^{\infty} (i^2 + i - 2) \, \varphi^{i-1} \; , \tag{2.35}$$

is obtained. For the latter sum a closed expression is still accessible depending on $i_{\max.}$.

3 Results and Discussion

3.1 Overlap algorithms and closest surface distances

The calculation of the potential energy to determine the acceptance of a proposed step in a Monte Carlo simulation as well as the computation of the integrand in the numerical integration of the investigated virial coefficients requires the determination of overlaps and non-overlaps of anisotropic hard particles. For the cluster technique, a further determination of the surface distance is necessary to calculate the bond probability in a cluster move. In the following, the overlap- and surface distance algorithms for the primary geometries of interest, ellipsoids of revolution and lenses are presented. The overlap algorithm is additionally validated.

To identify overlaps between ellipsoids, the established algorithm of Perram and Wertheim is used [115]. As it requires a numerical minimisation, the original Brent routine is substituted by a more efficient Newton-Raphson minimisation [116] considering the first and second derivative of the Perram-Wertheim contact function. This optimisation allows higher efficiency and accuracy.

The calculation of the second virial coefficient [Eq. (2.5a)] as an orientationally dependent average can be used to test the reliability of overlap algorithms of convex geometries as the numerical results can be compared to the analytical coefficients obtained via the Isihara-Hadwiger theorem [Eq. (2.8)]. For the investigated geometries the necessary geometric measures can be found in [63].

The numerical results obtained as well as the relative deviation to the analytic values are illustrated in Fig. 3.1. For a range of aspect ratios, the algorithm could be verified with high accuracy. All values correspond within the uncertainties with the analytical relation.

The closest surface distance $\sigma(\mathbf{A}, \mathbf{B})$ between two ellipsoids $\mathbf{A}$ and $\mathbf{B}$, described by their shape, orientation, and center of mass, can not be calculated directly. Paramonov and Yaliraki [117], however, identified two limits based on the Perram-Wertheim contact function. The upper limit $\sigma_{\mathrm{ul}}(\mathbf{A}, \mathbf{B})$ and lower limit $\sigma_{\mathrm{ll}}(\mathbf{A}, \mathbf{B})$ thereby fulfil the inequality

$$0 < \sigma_{\mathrm{ll}}(\mathbf{A}, \mathbf{B}) \leq \sigma(\mathbf{A}, \mathbf{B}) \leq \sigma_{\mathrm{ul}}(\mathbf{A}, \mathbf{B}) \tag{3.1}$$

for non-overlapping particles. While the upper limit is a good approximation for large distances as in the limit $\sigma_{\mathrm{ul}}(\mathbf{A}, \mathbf{B}) \to \infty$ the orientation of both ellipsoids becomes irrelevant, for small separations $\sigma_{\mathrm{ll}}(\mathbf{A}, \mathbf{B})$ is the preferable choice [117].

Although hard lenses have been investigated, there it no published algorithm to determine the overlap problem. Lenses with aspect ratio $\nu = \nu\, r_{\mathrm{eq}}/r_{\mathrm{eq}}$ are defined as the section of two spheres with radius R_0, where the distance between the centres of the generating spheres d is smaller $2\,R_0$ as illustrated in Fig. 3.2a. The configuration of two lenses can be distinguished into two principle categories: critically inclined and undercritically inclined lenses.

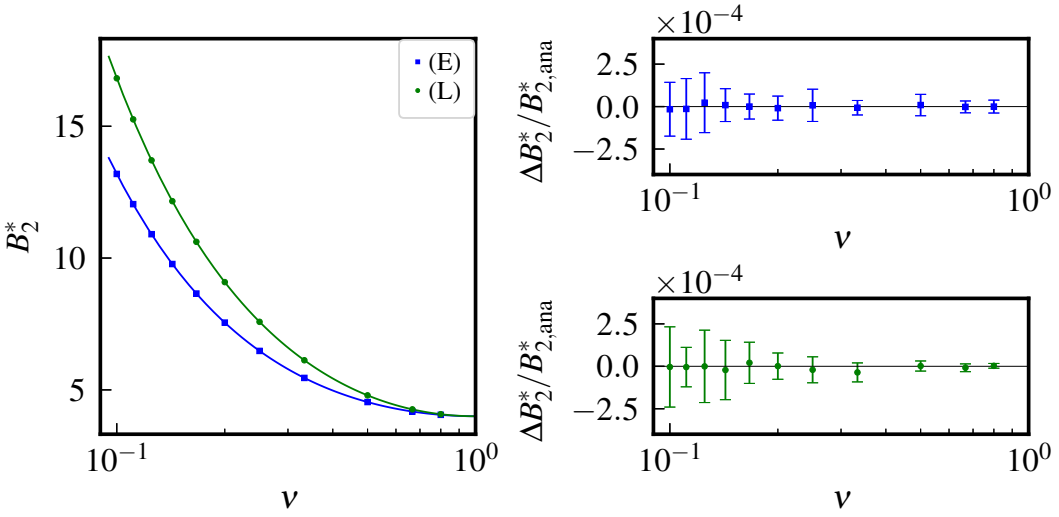

Fig. 3.1: Validation of the overlap algorithms for hard oblate ellipsoids (blue) and lenses (green) by calculation of the second virial coefficient B_2^* in dependence on the aspect ratio ν. The solid lines represent the analytical values $B_{2,\mathrm{ana}}^*$.

Let $\underline{\mathbf{K}}_i$ and $\underline{\mathbf{K}}_j$ denote the centres of the two most distant generating spheres. For undercritically inclined lenses the vector $\underline{\mathbf{K}}_j - \underline{\mathbf{K}}_i$ is contained in both critical cones with aperture ϑ_c and apices in $\underline{\mathbf{K}}_i$ and $\underline{\mathbf{K}}_j$, respectively. This is shown in Fig. 3.2b, the cones are represented by green lines. This case can be reduced to the overlap problem of spheres.

The two possibilities for an intersection of critically inclined lenses are displayed in Fig. 3.2c. Either one of the equatorial singularities intersects with the other lenses generating sphere (blue and red lens) or the two equator circles intersect (blue and green lens). While the first case can be reduced to the closest point on a circle to the generating spheres' center, the latter case is in principle a plane section with two constraints.

A detailed description of the required procedure of the overlap algorithm with further illustrations can be found in [66]. As no numerical minimisation is involved, this method is significantly faster than the implemented ellipsoid routine. The results for the validation of this algorithm based on the calculation of the second virial coefficient are also shown in Fig. 3.1 with a similar accuracy as the ellipsoid algorithm.

The concept of this overlap algorithm can be extended to calculate the closest surface distance of lenses. While in the case of undercritically inclined lenses the surface distance can again be reduced to the closest distance between the lenses generating spheres, for critically inclined lenses different possibilities exist. Either the closest surface distance lies between one of the lenses' generating spheres and the circular singularity of the other lens (two permutations) or it is between the singularities of both lenses. The first case can be solved us-

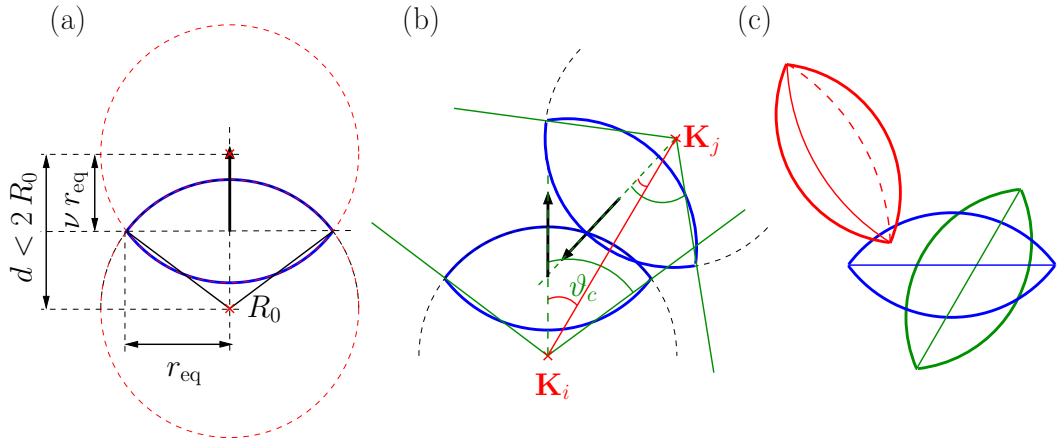

Fig. 3.2: (a) Geometric construction of a lens as the section of two generating spheres with radius R_0.
(b) Intersection of two undercritically inclined lenses.
(c) Two possible types of intersections for critically inclined lenses.

ing parts of the overlap algorithm to calculate the closest point of a circle to a point. In the latter case the closest distance between two circle in three dimensions can be reliably computed using the algorithm of Vranov [118]. Details with figures illustrating the cases can be found in [68].

3.2 Calculation of higher-order virial coefficients

The calculation of virial coefficients according to Eq. (2.6) for anisotropic solids of revolution requires a $5(i-1)$-dimensional integration of a substantially increasing number of graphs needing to be considered (compare Table 2.1). For the investigated systems, the Mayer-sampling algorithm is a suitable numerical approach.

In the case of hard-body interaction, only one Ree-Hoover graph has a nonzero contribution to a specific virial coefficient [76]. The efficient identification of the relevant graph and associated star content is a promising opportunity for optimisation of a hard particle algorithm instead of calculating the sum of products directly as customary for other potentials. The benefit increases with the complexity of the integrand. A novel algorithm based on a bisection search in a sorted list of ordinal numbers is proposed.

Additionally, the use of an optimised reference integral for the Mayer-Sampling algorithm can be investigated. A hard-sphere system with identical volume to the system of interest is an obvious variant. The efficiency of the Mayer-Sampling algorithm increases when the reference is as similar to the system of interest as possible. An anisotropic reference is therefore favourable. When using anisotropic virial coefficients as a reference, only numerical values with limited accuracy are available. As a second significant optimisation an intrinsic

reference integrand based on trees is suggested.

Furthermore, the original Mayer-sampling acceptance criterion is altered for hard particle systems by not only considering the contribution of the system of interest but also that of the reference. An adjustable weighting factor is introduced so that on average the moduli of both integrands have a roughly equal contribution. This guarantees a correct sampling of the complete configuration space of both the reference and system of interest.

3.2.1 Optimisation of the Mayer-Sampling algorithm for hard particles

As Ree-Hoover graphs are fully connected by either f- or e-bonds, they can be represented by the upper triangle of an adjacency matrix with binary elements. In the following f-bonds are represented by 1 and e-bonds by 0. The graphs for the virial coefficient of order i can be written as a binary number requiring $n(n-1)/2$ bits to describe the equivalent number of bonds. For convenient memory allocation, the binary numbers are completed with trailing zeros to multiples of 8, the order $i = 4$ therefore requiring 1 byte, the orders $i = 5$ and $i = 6$ 2 bytes, and so on. This procedure is compiled exemplarily for the graphs of B_4 [Eq. (2.7)] in Table 3.1. The list of binary numbers obtained can be converted to ordinary numbers and sorted. Additionally, the set of graphs can be divided into subclasses in dependence on the number of e-bonds $n_e = i(i-1)/2 - n_f$.

Table 3.1: Matrix representation of the two subclasses of Ree-Hoover graphs of order $i = 4$ in the denoted matrix notation represented as binary numbers with corresponding ordinal numbers. The number of digits of the binary number are filled up with zeros to multiples of 8 for convenient memory allocation, *i.e.* 8 for $i = 4$.

Subclass 0	Subclass 2		
$n_e = 0, n_f = 6$	$n_e = 2, n_f = 4$		
			
$\begin{pmatrix} 0 & \mathbf{1} & \mathbf{1} & \mathbf{1} \\ 1 & 0 & \mathbf{1} & \mathbf{1} \\ 1 & 1 & 0 & \mathbf{1} \\ 1 & 1 & 1 & 0 \end{pmatrix}$	$\begin{pmatrix} 0 & \mathbf{1} & \mathbf{0} & \mathbf{1} \\ 1 & 0 & \mathbf{1} & \mathbf{0} \\ 0 & 1 & 0 & \mathbf{1} \\ 1 & 0 & 1 & 0 \end{pmatrix}$	$\begin{pmatrix} 0 & \mathbf{0} & \mathbf{1} & \mathbf{1} \\ 0 & 0 & \mathbf{1} & \mathbf{1} \\ 1 & 1 & 0 & \mathbf{0} \\ 1 & 1 & 0 & 0 \end{pmatrix}$	$\begin{pmatrix} 0 & \mathbf{1} & \mathbf{1} & \mathbf{0} \\ 1 & 0 & \mathbf{0} & \mathbf{1} \\ 1 & 0 & 0 & \mathbf{1} \\ 0 & 1 & 1 & 0 \end{pmatrix}$
11111100	**10110100**	**01111000**	**11001100**
252	180	120	204

The graph and therewith star content for a random configuration of overlaps and non-overlaps represented in the same manner by an ordinal number can be effectively identified in the list acquired by means of a bisection search. Non-contributing Ree-Hoover graphs with $c_{\mathrm{G}} = 0$ are thereby not elements of the list. The integrand of interest resulting from the specific configuration then reads $(-1)^{n_f} c_{\mathrm{G}}$ with every f-bond contributing a factor of $f_{ij} = -1$.

The bisection search introduced scales with $\log_2 N(i, n_f)$ if $N(i, n_f)$ is the cardinality of the Ree-Hoover subset of graphs with i nodes and n_f f-bonds. This specific optimisation for hard particles requires less numerical effort in comparison with classical integer arithmetic approaches for orders $i \geq 6$ with substantial gains for higher-order virial coefficients.

The approach presented is limited by memory requirements as these are proportional to the number of Ree-Hoover graphs. For example the 21 286 987 064 diagrams for order $i = 9$ each require 5 bytes for the binary representation and 2 bytes for the star contents resulting in roughly 140 GB in total. Using state-of-the-art computers, the presented algorithm is still feasible up to B_9, for higher virial coefficients alternative methods have to be considered [48].

3.2.2 Trees as an intrinsic reference integral

In graph theory trees are a subset of the graphs called hypertrees excluding the subset of graphs containing hyperedges, also known as leaves. In contrast to the biconnected Mayer graphs, the connected graphs are articulated: If one node is removed, the graph decomposes into two graphs as no closed paths exist. Additionally, two edges may only have one common vertex or none. Trees with i nodes have $i - 1$ edges which in the following again represent Mayer f-functions.

The two topological classes for trees with four nodes and three classes for trees with five nodes are shown in Table 3.2. An illustration of the hypertrees up to order $i = 8$ can be found in the work of Hellmann and Bich [77].

As the f-bonds are connected via articulation points, using Eq. (2.5a) the trees of order i can be factorised to powers of the second virial coefficient. A reference integral can therefore be written as

$$I_{\mathrm{ref}} = N_{\mathrm{T}} \left(-2B_2\right)^{i-1} \ , \tag{3.2}$$

if N_{T} denotes the number of trees considered. A random configuration has a contribution to this integrand if the f-bonds of the trees considered are a subset of the non-zero f-bonds of the configuration.

Table 3.2: Unlabelled trees for the order $i = 4$ and $i = 5$ with i nodes and $i - 1$ Mayer f-bonds. For each topological class the cardinality N_{T} based on the orders of the nodes is given.

$i = 4$		$i = 5$		
				
$N_{\mathrm{T}} = 4$	$N_{\mathrm{T}} = 12$	$N_{\mathrm{T}} = 5$	$N_{\mathrm{T}} = 60$	$N_{\mathrm{T}} = 60$
(3,1,1,1)	(2,2,1,1)	(4,1,1,1,1)	(3,2,1,1,1)	(2,2,2,1,1)

Initial calculations demonstrated that the highest branched trees occur most frequently when the Ree-Hoover diagrams are determined. As the reference integral has the sole requirement of being a subset of the system of interest configuration space, any number of these reference diagrams may be used. In the subsequent calculations when determining the virial coefficient of order i therefore only the topological class containing the i highest branched trees with one node of order $i-1$ and $i-1$ nodes with order 1 are considered. The reference integral is then given by Eq. (3.2) with $N_T = i$. The consideration of further trees showed no significant impact in trial calculations.

The use of highly branched trees as an intrinsic reference unites a variety of advantages. First of all, the computational effort is significantly reduced as definitely only one geometry has to be considered and the overlap algorithms are only performed for the system of interest. From the saved overlaps and non-overlaps the contribution of the reference trees can be determined concurrently. Secondly, as the same geometry with same aspect ratio is used, both integrands are determined in the same configuration only differing by the graphs considered. For nonspherical shapes, this guarantees the same orientational subspace. Thirdly, only a few trees have to be considered for the reference integral: In contrast to the use of numerical virial coefficients as reference integrals for higher orders, the limited amount of trees are a minor numerical cost than, for example, Ree-Hoover graphs. Additionally, for convex shapes, as the second virial coefficient is analytically known and trees factorize to its powers, an analytically known reference integral can be used even for higher orders of virial coefficients without error propagation.

3.2.3 Validation of the developed Mayer-Sampling algorithm

A Mayer-Sampling algorithm based on the method described is used to calculate the virial coefficients of hard oblate ellipsoids of revolution and lenses. Calculations of virial coefficients were performed for a variety of aspect ratios from order $i = 2$ up to order $i = 8$ for at least eight independent runs with 2×10^{10} steps each. The results with uncertainties obtained from standard deviations are compiled in Table I - Table III in [66]. As both investigated geometries approach the shape of a sphere for the limit $\nu \to 1^-$, their virial coefficients can be compared to literature values [119]. The relative uncertainties increase from 7×10^{-5} for B_3^* up to 9×10^{-3} for B_8^* and all values for hard spheres are in excellent accordance with the literature data. Although the calculated uncertainties are larger than those of the literature data, this is not a principle limitation of the algorithm presented. The focus of this work is an aspect-ratio-dependent investigation of different geometries. Due to the additional computational expense of the orientation-dependent contact problem, uncertainties arise from comparatively short runs.

Since the orientationally averaged second virial coefficient reproduces the analytic Isihara-Hadwiger relation, the additional extension to orientation-dependent systems is a first validation. Additionally, the values of hard el-

lipsoids were compared to known literature values up to $i = 7$ [51]. Up to the order $i = 6$ the calculated data excellently agrees with the exception of $\nu = 1/10$ for B_6^*. For B_7^* deviations exceed the uncertainty for $\nu \leq 1/4$, a comparison is visualised in Fig. 3.3. The two virial coefficients of order $i = 8$ for ellipsoids in [52] were based on incorrect assumptions [53], a comparison is therefore not worthwhile.

As for lenses, only the second virial coefficient is known, a direct validation is not possible. However, the validation of both the Mayer-Sampling algorithm for anisotropic ellipsoids and the overlap algorithm for lenses are an indication of the reliability of the utilised approach for lenses.

3.2.4 Evaluation of determined virial coefficients

Virial coefficients for hard ellipsoids of revolution and hard lenses are calculated up to order $i = 8$ and compiled in Table II and Table III in [66]. Up to the order $i = 7$ and for moderately anisotropic particles including $i = 8$ these data exhibit a high accuracy. While the virial coefficients for order $i = 8$ of intermediately anisotropic particles exhibit an acceptable accuracy, the uncertainties for the highly anisotropic particles are in the magnitude of the value. Hence, these values are an indication of the values' modulus and not their sign.

Boublík proposed reducing virial coefficients of three-dimensional convex geometries to powers of the second virial coefficient as $\tilde{B}_i = B_i/B_2^{i-1}$ and investigating the dependence on the inverse of the quantity

$$\alpha = \frac{B_2^* - 1}{3} = \frac{S_\mathrm{P}\tilde{R}_\mathrm{P}}{3V_\mathrm{P}} \ . \tag{3.3}$$

The value α is thereby the scaled excess part of the excluded volume, the factor 3 normalizing $\alpha\,(\nu = 1) = 1$ for a sphere. The reduced virial coefficients $\tilde{B}_i$ in dependence on α^{-1} are displayed in Fig. 3.3.

For the virial coefficients of orders $i = 3$ to $i = 5$ a nearly linear dependence can be observed while the higher coefficients up to $\tilde{B}_8$ have a parabolic relationship. The lines in Fig. 3.3 are least-squares fits to the polynomial equation

$$\tilde{B}_i\left(\alpha^{-1}\right) = a_{0,i} + a_{1,i}\alpha^{-1} + a_{2,i}\alpha^{-2} \tag{3.4}$$

confirming this assumption.

Interestingly, both oblate geometries in a first approximation show an identical dependence. However, for small α^{-1} deviations are visible which can also be identified in the different parameters of the fits (compare Table IV in [66]). With the parameters obtained, an interpolation for intermediate aspect ratios is possible, yet a physical significance has not been identified (compare Fig. 10 in [66]).

The most obvious difference between the two shapes investigated is the two-dimensional discontinuity of the surface curvature of the lens. With increasing

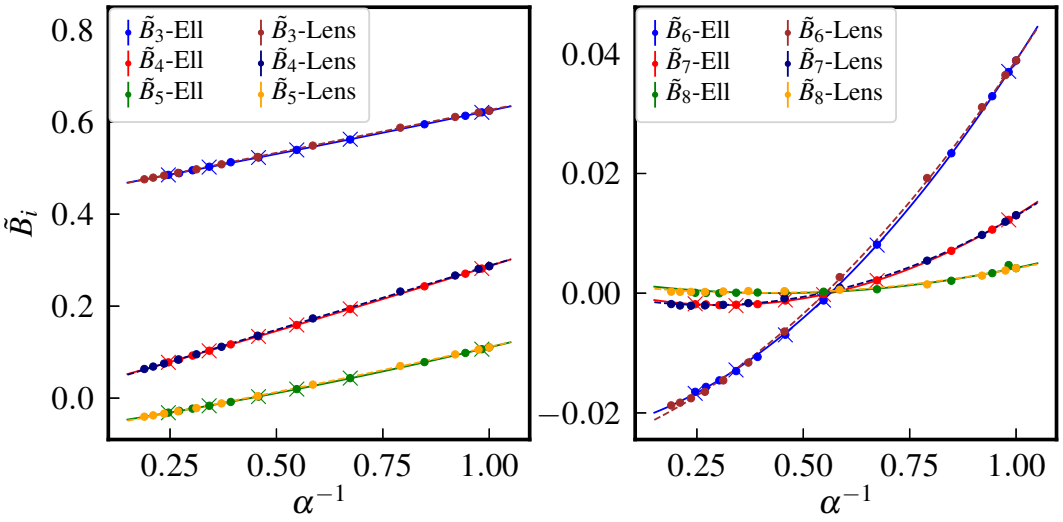

Fig. 3.3: Reduced virial coefficients $\tilde{B}_i$ of hard oblate ellipsoids and lenses in terms of their inverse scaled excess part of the excluded volume α^{-1} [Eq. (3.3)]. Crosses are reduced virial coefficients of oblate ellipsoids from [51] as a reference. Lines represent least-squares fits of the reduced virial coefficients to parabolas [Eq. (3.4)].

anisotropy this singularity has an increasing impact on the second virial coefficient with that of lenses increasingly exceeding the second virial coefficient of oblate ellipsoids of revolution. However, this effect is not apparent in the graphical representation chosen which suggests in first approximation a seemingly universal behaviour of the virial coefficients. This leads to the conclusion that a significant contribution of the impact of anisometry has to be described by the second virial coefficient.

In principle, a virial equation of state can be obtained with the calculated virial coefficients. The resulting equation of state and an exemplary breakdown of the individual coefficients contribution can be found in Fig. 11 to Fig. 15 in [66]. In this work, the virial equation of state obtained will be discussed at a later stage after the complementary simulation method and results are presented.

3.2.5 Extending the Mayer-Sampling algorithm to $\mathbb{R}^4$

For the seemingly, in first approximation universal behaviour of oblate hard particles in three dimensions no direct physical cause could be identified. However a conclusion might be evident when comparing the effect of dimensionality $\mathbb{R}^D$ on the virial coefficients of hard particles.

The effects of the dimensionality on the virial coefficients of hyperspheres in higher dimensions were already studied by Ree and Hoover in 1964 [120] and have been extended up to order $i = 64$ and $D = 100$ [76, 121], where a

primary focus has been on the sign of the hard hyperspheres coefficients. As the investigation of the virial coefficients of an anisotropic geometry in $D > 3$ has not been performed, a complementary study thereon is the focus of the next section.

The Mayer-sampling algorithm can be extended to four-dimensional euclidean space. In principle, the calculation of the integrand based on overlaps and non-overlaps of the geometry of interest is identical to the procedure in $\mathbb{R}^3$. However, the geometry-specific overlap procedure has to be adapted. The extension to the higher dimensional integration space is performed indirectly by adapting the translation and rotation algorithms to $\mathbb{R}^4$.

Hyperspherocylinders were chosen as the first anisotropic convex geometry in $\mathbb{R}^4$ because the overlap algorithm of spherocylinders can easily be extended to higher dimensions. The prolate hyperspherocylinder can be described as a union of hyperspheres with radius r_{eq} located on the line segment $\underline{\mathbf{r}} = \underline{\mathbf{c}} + \lambda\,\underline{\hat{\mathbf{u}}}$ if $\underline{\mathbf{c}}$ denotes the hyperspherocylinders' center of mass and $\underline{\hat{\mathbf{u}}}$ its orientation. The length of the hypercylinders barrel thereby defines the limits of the parameter λ as $-(\nu-1)r_{\mathrm{eq}} \leq \lambda \leq (\nu-1)r_{\mathrm{eq}}$.

Based on the algorithm of Vega and Lago [122], the overlap problem is reduced to the closest distance between the lines $\underline{\mathbf{r}}_1(\lambda) = \underline{\mathbf{c}}_1 + \lambda\,\underline{\hat{\mathbf{u}}}_1$ and $\underline{\mathbf{r}}_2(\mu) = \underline{\mathbf{c}}_2 + \mu\,\underline{\hat{\mathbf{u}}}_2$ under the constraints $|\lambda| \leq (\nu-1)r_{\mathrm{eq}}$ and $|\mu| \leq (\nu-1)r_{\mathrm{eq}}$. An overlap is present if the minimum distance is $|\underline{\mathbf{r}}_1(\lambda_{\min}) - \underline{\mathbf{r}}_2(\mu_{\min})| \leq 2\,r_{\mathrm{eq}}$, otherwise, the two hyperspherocylinders do not overlap.

For the particles necessary random translation and rotation attempts the procedures of the algorithms have to also be extended to $\mathbb{R}^4$. A new particle position is obtained from the previous position by translation along a randomly orientated unit vector $\underline{\hat{\mathbf{u}}}_{\mathrm{r}}$. To achieve a homogeneous exploration of space it is useful to introduce generalised angular coordinates $\boldsymbol{\Omega}(\vartheta, \chi, \varphi)$ with the probability densities

$$p(\vartheta) = \frac{2\sin^2\vartheta}{\pi} \quad \text{with} \quad 0 \leq \vartheta \leq \pi \quad , \tag{3.5a}$$

$$p(\chi) = \frac{\sin\chi}{2} \quad \text{with} \quad 0 \leq \chi \leq \pi \quad , \text{ and} \tag{3.5b}$$

$$p(\varphi) = \frac{1}{2\pi} \quad \text{with} \quad 0 \leq \varphi \leq 2\,\pi \; . \tag{3.5c}$$

Based on the angular coordinates $\boldsymbol{\Omega}_{\mathrm{r}}(\vartheta_{\mathrm{r}}, \chi_{\mathrm{r}}, \varphi_{\mathrm{r}})$ and using the abbreviations

$$d = \sin\vartheta_{\mathrm{r}} \sin\chi_{\mathrm{r}} \cos\varphi_{\mathrm{r}} \tag{3.6a}$$

$$c = \sin\vartheta_{\mathrm{r}} \sin\chi_{\mathrm{r}} \sin\varphi_{\mathrm{r}} \tag{3.6b}$$

$$b = \sin\vartheta_{\mathrm{r}} \cos\chi_{\mathrm{r}} \tag{3.6c}$$

$$a = \cos\vartheta_{\mathrm{r}} \tag{3.6d}$$

a randomly orientated unit vector $\underline{\hat{\mathbf{u}}}_{\mathrm{r}}$ can be written as $\underline{\hat{\mathbf{u}}}_{\mathrm{r}} = (d, c, b, a)^{\mathrm{T}}$. If the probability densities are correctly generated according to Eqs. (3.5) resulting in

a homogeneous distribution on a unit-hyperspheres' hypersurface, a randomly orientated unit vector can be generated allowing an unbiased sampling of the translation.

For the random rotation, an algorithm using the rotation matrix

$$\mathbf{R}(\mathbf{\Omega}_\mathrm{r}) = \begin{pmatrix} a & -b & c & -d \\ b & a & -d & -c \\ -c & d & a & -b \\ d & c & b & a \end{pmatrix} \tag{3.7}$$

based on the Hamilton quaternion [123] and the additional rotation matrix

$$\mathbf{\Psi}(\psi) = \mathbf{R}(\psi, 0, 0) = \begin{pmatrix} \cos\psi & -\sin\psi & 0 & 0 \\ \sin\psi & \cos\psi & 0 & 0 \\ 0 & 0 & \cos\psi & -\sin\psi \\ 0 & 0 & \sin\psi & \cos\psi \end{pmatrix} \tag{3.8}$$

is used. Essentially it transforms an arbitrary unit vector via $\mathbf{R}^\mathrm{T}(\mathbf{\Omega})$ to an invariant coordinate system, performs a rotation by ψ, and finally back-transforms the vector to the original coordinate system. A unit vector $\underline{\hat{\mathbf{u}}}_N$ can therefore be randomly rotated by combining the rotation matrices as

$$\underline{\hat{\mathbf{u}}}_{N+1}(\mathbf{\Omega}_N, \psi) = \mathbf{R}(\mathbf{\Omega}_N).\mathbf{\Psi}(\psi).\mathbf{R}^\mathrm{T}(\mathbf{\Omega}_N).\underline{\hat{\mathbf{u}}}_N \tag{3.9}$$

to obtain the new randomly rotated unit vector $\underline{\hat{\mathbf{u}}}_{N+1}$. The random rotation angle ψ is generated with a uniform probability distribution in $-\Delta_\mathrm{rot} \leq \psi \leq \Delta_\mathrm{rot}$ if the maximum rotation is denoted by Δ_rot. A detailed explanation can be found in the supporting information of Ref. [69].

The rotation algorithm was validated by rotating an arbitrary unit vector for 10^{10} steps and simultaneously calculating the probability densities of the angular coordinates. The probability densities obtained correspond with the theoretical predictions of Eqs. (3.5) (compare Fig. 3 in [69]) allowing a homogeneous exploration of the unit-hypersphere's hypersurface.

As the reference integral for the Mayer-sampling algorithm different variants are used. For the second virial coefficient for aspect ratios $\nu \leq 5$, the virial coefficients of hard hyperspheres are used, which are scaled to the same hypervolume of the hyperspherocylinder of interest. When investigating hyperspherocylinders with $\nu > 5$, the reference integral $B_2(\nu = 5)$ is used to guarantee a more efficient sampling for highly anisotropic geometries. For higher-order virial coefficients $i \geq 3$ the highly branched trees, as in Sec. 3.2.2, are used.

Virial coefficients B_2 up to B_6 of hard hyperspherocylinders are calculated for a range of aspect ratios and compiled in Table I in [69]. They result from at least 16 independent runs with 5×10^{10} steps, uncertainties are given by standard deviations. As the virial coefficient $B_2(\nu = 5)$ is sometimes used as a reference, this specific coefficient was sampled exhaustively to minimise the

uncertainty of the numerical reference.

The algorithm with exception of the rotation implementation and geometry-specific overlap can be validated via the virial coefficients of hard hyperspheres. For the virial coefficients B_3 up to B_6 the literature values of hard hyperspheres (Ref. [76]) could be reproduced within the respective uncertainties. The homogeneous sampling of the rotation algorithm was previously verified. A direct evaluation of the overlap and coupled rotation is not directly possible. However, if a relation based on the geometric measures can describe the calculated second virial coefficients with high accuracy, it can be considered as a good indication.

With the second virial coefficients calculated, a comparison with a proposed relation for an analogue of the Isihara-Hadwiger theorem in four dimensions in Ref. [124] is possible. Although the correct limit is obtained for $\nu \to 1^+$, with increasing aspect ratio, significant discrepancies can be observed (Fig. 1, Ref. [69]). The data can instead be excellently described with the relation

$$B_2^* = 2\,\frac{S_\mathrm{P}\tilde{R}_\mathrm{P}}{V_\mathrm{P}} \tag{3.10}$$

as proposed in Ref. [69]. Interestingly, the particle hypervolume is in contrast to $\mathbb{R}^2$ and $\mathbb{R}^3$ [Eq. (2.8)] not an additive contribution. However, the universality of this proposed conjecture as an analogue of the Isihara-Hadwiger theorem in $\mathbb{R}^4$ has to be investigated in future work by examining further convex geometries.

When comparing the higher-order virial coefficients $\nu \geq 3$, with increasing anisotropy the even-order virial coefficients B_4 and B_6 become negative while the odd-order coefficients B_3 and B_5 remain positive. An identical behaviour has been observed for hyperspheres in $D \geq 8$ for third- and higher-order virial coefficients [76].

In accordance with the definitions in Ref. [125] a scaled excess part of the excluded volume as in Eq. (3.3) for $\mathbb{R}^3$ can be defined in $\mathbb{R}^4$ as

$$\alpha = \frac{B_2 - V_\mathrm{P}}{7\,V_\mathrm{P}} \tag{3.11}$$

with the scaling factor $1/7$ again guaranteeing $\alpha(\nu \to 1^+) = 1$. The corresponding graph of $\tilde{B}_i = B_i/B_2^{i-1}$ in dependence on α^{-1} (Fig. 2 in [69]) in contrast to Fig. 3.3 for $\mathbb{R}^3$ does not show the same characteristic. Instead of a nearly linear (B_3 to B_5) or parabolic (B_6 to B_8) behaviour of the oblate shapes investigated in $\mathbb{R}^3$, the trend can be adequately described by a third-order polynomial in $\mathbb{R}^4$. The reason for this behaviour is not directly explainable without additional investigation of higher coefficients and further geometries. The fits obtained can, however, be used for interpolation to gain access to intermediate aspect ratios.

3.3 Simulation results

3.3.1 Overview of the simulation algorithm using cluster scaling

The standard approaches for the simulation of anisotropic shapes in an (N, p, T) ensemble can be found in the monographs of Frenkel and Smit as well as Allen and Tildesley [103, 104]. In the following, a brief overview of the volume-scaling routine allowing cluster formation following the principles outlined by Almarza [65] is presented.

In the first step, bonds are generated between particles according to the probability given by Eq. (2.23). For each cluster, a list is generated containing all linked particles. If a generated bond links two particles of formerly separate clusters, these two lists have to be united. In a subsequent step, the simulation box and clusters are rescaled keeping the distances within clusters constant. In a standard scaling attempt using reduced coordinates only the box is changed, while the relative particle coordinates remain unchanged. In a cluster scaling attempt this also applies to remaining single particles and the cluster's center of mass, the relative coordinates of particles belonging to a cluster, however, have to be rescaled accordingly to preserve the particle distances in a cluster. The obtained trial configuration has to be checked for cluster percolation and overlaps between particles. If either are identified, the trial configuration is rejected. Finally, the complete acceptance probability according to Eq. (2.25) is evaluated.

Considering that interparticle distances and orientations are preserved between particles within a cluster move and therefore $\sigma'_{ij} = \sigma_{ij}$ and consequently $[1 - b(\sigma'_{ij})]/[1 - b(\sigma_{ij})] = 1$, the product of the cluster probability ratio can be calculated over all particle permutations $[ij]$ and not only those where i and j belong to different clusters as originally proposed by Almarza [65]. When additionally rewriting the cluster probability ratio in Eq. (2.26) as

$$\frac{\omega_c(\chi_c|\underline{\mathbf{s}}'^N, V')}{\omega_c(\chi_c|\underline{\mathbf{s}}^N, V)} = \frac{\prod\limits_{[ij]} \left[1 - b(\sigma'_{ij})\right]}{\prod\limits_{[ij]} \left[1 - b(\sigma_{ij})\right]} \ , \tag{3.12}$$

it is possible to calculate the cluster probabilities $\omega_c(\chi_c|\underline{\mathbf{s}}'^N, V')$ and $\omega_c(\chi_c|\underline{\mathbf{s}}^N, V)$ separately without *a priori* knowledge of the specific cluster realisation. This allows to simultaneously calculate the probability $\omega_c(\chi_c|\underline{\mathbf{s}}^N, V)$ while generating the bonds and $\omega_c(\chi_c|\underline{\mathbf{s}}'^N, V')$ during the overlap check. The numerical effort is further reduced by using combined overlap and surface-distance routines.

The algorithm implemented is based on periodic boundary conditions and makes use of a Verlet neighbour list to increase efficiency. This has to be taken into account when generating bonds, calculating the cluster's center of mass, rescaling positions, or calculating the cluster probabilities.

3.3.2 Simulation details

Based on the algorithms described for selected aspect ratios and particle numbers, independent calculations are performed for each pressure of interest. A single Monte Carlo step is here defined as N random particle translation or rotation attempts as well as one volume change attempt. The maximum distance for translation, the maximum angle of rotation, and the maximum relative volume change and deformation are tuned during equilibration to obtain an acceptance ratio $p \approx 1/2$. The characteristic length for bond generation δ is tuned so that $N_\mathrm{b}/N \approx 1/4$, whereby N_b denotes the number of bonds created between particles. This guarantees that the number of rejections due to cluster percolation is less than 1%.

Calculations to analyse the equation of state or the isotropic-nematic phase transition are performed as compression simulations with 1000 particles. These are initialised from a cubic lattice with randomly aligned orientations. After a first equilibration phase, at a volume fraction of $\varphi = 0.05$, the ensembles are compressed to the pressure of interest. After a further equilibration phase wherein all variables are adjusted to the required acceptance rate and subsequently locked, a production run consisting of 5×10^7 steps is started, during which the observables of interest are calculated.

When an isotropic-solid phase transition is however of interest, expansion simulations are performed, initialised from a dense SM2 crystal. The particles number lies between $N = 972$ and $N = 1040$ in dependence on the aspect ratio, chosen to minimize the anisotropy of the simulation box. Additional shape fluctuations at constant volume are introduced and several subsequent runs with in total at least 2×10^8 steps are calculated.

3.3.3 Validation of the algorithm

As hard spheres are an extensively studied model and are the limit of both geometries for $\nu = 1$, they are again used to validate the data obtained. In the first step, the data of the isotropic phase is compared to the highly accurate equation of state of Kolafa *et al.* [112]. The data calculated in reference to the Kolafa equation of state is displayed in Fig. 3.4 (left) for five system sizes ranging from $N = 500$ up to $N = 2916$. As a comparison, data for the system $N = 864$ from a significantly longer simulation (2.5×10^8 steps) calculated with a standard volume fluctuation procedure is displayed.

The significantly smaller uncertainties of the volume fraction φ resulting from the algorithm allowing cluster formation in contrast to the standard (N, p, T) algorithm for the system size $N = 864$ show the benefit of the cluster technique. When comparing different system sizes, a significant dependence on the number of particles is evident with increasing reduced pressure $\beta p r^3$. This is pronounced for smaller systems in the region of the phase transition indicated by the dashed black line (data from Noya *et al.* [126]). For larger systems, the deviations are within the determined uncertainties. The high accuracy of the data obtained is a first validation of the implemented algorithm.

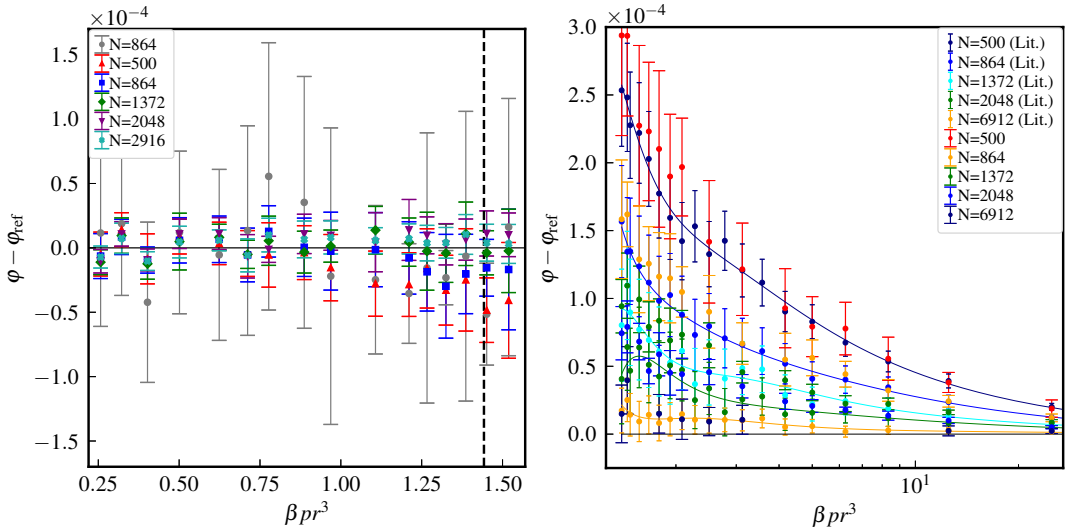

Fig. 3.4: The left figure from [67] shows deviations in volume fraction φ in dependence on the reduced pressure βpr^3 using [112] as a reference for the isotropic phase of hard spheres. Data is displayed for different system sizes obtained using a cluster routine with 5×10^7 steps. The grey data is calculated with a standard (N, p, T)-approach during 2.5×10^8 steps. The dashed line indicates the isotropic-solid phase transition (Ref. [126]).
The right figure shows data for the solid FCC phase of hard spheres in an equivalent manner in reference to the extrapolated thermodynamic limit of [65]. Here, additional data and system-size-dependent equations of state (solid lines) according to Ref. [65] are shown.

Additionally, an understanding of the impact of the system size for spherical system has been acquired.

A comparison of data for the solid phase of hard spheres in reference to the data calculated by Almarza [65] for a range of system sizes is shown in Fig. 3.4 (right) for five system sizes ranging from $N = 500$ up to $N = 6912$. The deviations are calculated in reference to the extrapolated thermodynamic limit of Almarza, solid lines indicate the equations of state for specific system sizes. The data of Almarza was thereby reproduced within the respective uncertainties.

The equation-of-state data for ellipsoids of Frenkel, Mulder, and McTague [22] as well as McBride and Lomba [59] can be compared to additionally validate the algorithm. The latter is visualised together with the data calculated in the supplementary material of [68]. However, the comparatively small ensembles ($N = 343$) and large uncertainties of the reference data do not allow a quantitative analysis. Additionally, the data was compared to separate calculations employing a standard technique also using the (N, p, T) ensemble, which excellently agree.

As no equation-of-state data is known for lenses, only a comparison with data calculated with a classical technique is possible. These agreed within the corresponding uncertainties. In the low-density limit, the accordance with the virial series is an additional indication of reliability.

3.3.4 Evaluation of simulation results

In principle, for the simulation of hard ellipsoids, the lower limit $\sigma_{\mathrm{ll}}(\mathbf{A},\mathbf{B})$ or upper limit $\sigma_{\mathrm{ul}}(\mathbf{A},\mathbf{B})$ for the closest surface distance of Paramonov and Yaliraki [117] can be used to generate bonds according to Eq. (2.23). As the length scale of δ should be better described by the lower limit, it can be assumed that using this limit may lead to smaller uncertainties. However, in trials for arbitrary aspect ratios and system sizes no systematic difference considering the respective uncertainties could be observed between data calculated with the two limits. The ratio of Eq. (2.26) presumably compensates for the over- and underestimations of the surface distance. As a consequence, an approximation of the closest surface distance is probably sufficient for cluster Monte Carlo simulations of hard shapes. For the subsequent systematic calculations, the lower limit $\sigma_{\mathrm{ll}}(\mathbf{A},\mathbf{B})$ is used.

The investigation of the influence of the system size was extended to anisotropic shapes by examining the influence on ellipsoids in the isotropic phase with an arbitrary aspect ratio of $\nu = 1/3$. The results are presented in Fig. 2 of Ref. [67]. As a reference, data from a system with $N = 4096$ particles is used. As also shown for the case of spheres, the influence of the system size is pronounced in the region of the phase transition. Beginning with a system size $N = 1000$, the deviations are in the range of the uncertainties. For the subsequent investigation therefore systems with $N = 1000$ are used for the compression simulations, where the computational expense is still acceptable.

Before equation-of-state data can be analysed, the limits of the isotropic phase have to be determined. For aspect ratios with an isotropic-nematic phase transition, the critical volume fraction is determined by linearly extrapolating the nematic order parameter

$$S_4 = \left\langle \frac{1}{8}\left(35x_i^4 - 30x_i^2 + 3\right)\right\rangle \tag{3.13}$$

to its root for pressures definitely beyond the phase transition. The scalar product $x_i = \underline{\hat{\mathbf{u}}}_j.\underline{\hat{\mathbf{u}}}_k$ is thereby calculated from the orientations of all pairs of particles j and k. This is a simple alternative to identify the existence of a nematic phase without *a priori* knowledge of the nematic director and avoids the use of the Saupe tensor [67, 127]. The extrapolation and limit obtained is visualised in Fig. 3 of Ref. [67] for ellipsoids and Fig. 4 of Ref. [68] for lenses.

The isotopic-solid phase transitions are determined from expansion simulations under consideration of the order parameters S_2 and Q_6 (Eqs. (2.27)-(2.28)) and can often be identified by obvious changes of the volume fraction

(compare Fig. 4 in [67] or Fig. 5 in [68]).

Both geometries exhibit a qualitatively identical phase behaviour for the investigated aspect ratios under consideration of the employed density resolution. While for aspect ratios $\nu \leq 1/3$ an isotropic-nematic phase transition is observed, the aspect ratio $\nu = 1/2$ transitions directly into the SM2 phase. The three aspect ratios $\nu = 2/3$, $\nu = 4/5$ and $\nu = 10/11$ transition from the isotropic into a plastic crystalline phase. The determined phase boundaries of the isotropic phase are compiled in Table I of [67] for ellipsoids and Table I of [68] for lenses. Odriozola *et al.* [46], however, identified a nematic phase for ellipsoids with $\nu = 1/2$ over a volume fraction range of $\Delta\varphi = 0.004$. This results from a different approach using significantly smaller ensembles and therefore making a higher density resolution possible. With this exception, the results are consistent with the work of Odriozola *et al.* on ellipsoids and Cinacchi and Torquato [60] on lenses.

With the procedure described, highly accurate equation-of-state data for hard particles is accessible with corresponding limits of the isotropic phase. The calculated data is compiled in Tables S-1 to S-4 in [67] for ellipsoids and in Tables S-1 to S-4 in [68] for lenses. A comparative analysis with the virial series is now possible and the subject of the next section.

3.4 Combining simulation results and the virial series

3.4.1 Truncated virial series

Using the virial coefficients previously calculated, the equation-of-state data obtained can be described using the virial approach

$$Z = \frac{p}{\varrho k_\mathrm{B} T} = 1 + \sum_{i=2}^{8} B_i^* \, \varphi^{i-1} \tag{3.14}$$

considering coefficients up to order $i = 8$. This is shown in Fig. 3.5a for selected aspect ratios of both geometries. While the low-density limit is described with high accuracy, severe discrepancies can be observed for volume fractions approaching the limit of the isotropic phase. These truncation effects of the virial series even lead to unphysical negative real gas factors for highly anisotropic particles, caused by negative virial coefficients which emerge for orders $i \geq 5$ for moderately and highly anisotropic particles. It is expected that these unphysical truncation effects would be compensated by even higher-order coefficients.

The obvious discrepancies are thereby evidence for the relevance of higher-order virial coefficients and thus many-particle interactions and their effect in denser hard-particle systems which intrinsically are included in many-particle Monte Carlo simulations. As the number of known virial coefficients is limited, relations to correct these contributions are essential. In the following, approaches to correct these effects are presented.

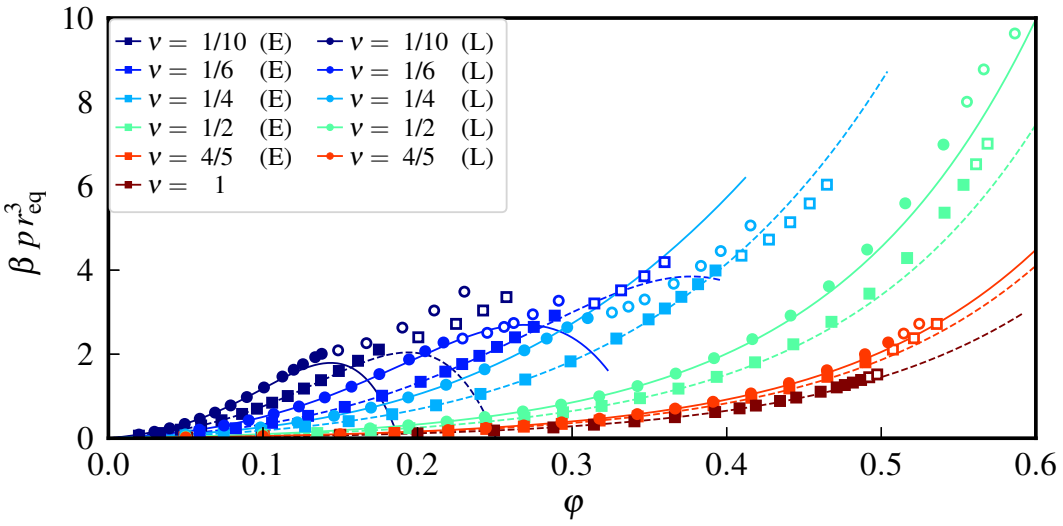

(a) Lines show the truncated virial series considering coefficients up to order $i = 8$ according to Eq. (3.14).

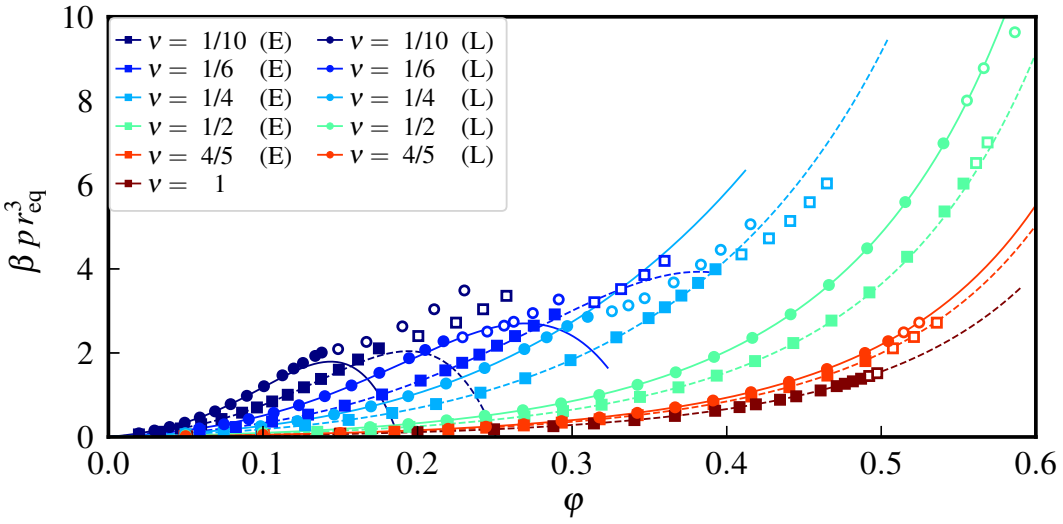

(b) Lines correspond with a virial approach using a rescaled Carnahan-Starling correction for the unknown coefficients according to Eq. (3.16).

Fig. 3.5: Equation-of-state data for selected aspect ratios of oblate ellipsoids (E) and lenses (L) described with two different approaches. Ellipsoids are represented by squares and lenses are shown as circles. Closed symbols represent data of the isotropic phase whereas open symbols are beyond the determined phase boundary of the isotropic phase.

3.4.2 Truncation correction of the virial series

The hard-sphere virial coefficients can be approximated by the Carnahan-Starling relation in Eq. (2.29) for the unknown orders $9 \leq i \leq \infty$ to obtain the closed expression

$$\sum_{i=9}^{\infty} \left(i^2 + i - 2\right) \varphi^{i-1} = \frac{2\varphi^8 \left(35\varphi^2 - 78\varphi + 44\right)}{\left(1-\varphi\right)^3} \tag{3.15}$$

under the condition $0 \leq \varphi < 1$. This result can be scaled in the Parson manner (compare Eq. (2.34)) to obtain an equation of state as suggested by Vega [Eq. (2.35)], which reads as

$$Z = 1 + \sum_{i=2}^{8} B_i^* \varphi^{i-1} + \frac{B_2^*}{4} \frac{2\varphi^8 \left(35\varphi^2 - 78\varphi + 44\right)}{\left(1-\varphi\right)^3} \tag{3.16}$$

considering virial coefficients of the anisotropic shape up to order $i = 8$ and a closed correction factor for the unknown higher-order coefficients. The results for this equation of state are shown in Fig. 3.5b for selected aspect ratios. A complete compilation can be found in the respective publications in Fig. 6, Ref. [67] for ellipsoids and in Fig. 7, Ref. [68] for lenses.

It is clearly visible that this correction accurately describes the data of moderately anisotropic particles over a wide density range. For intermediate aspect ratios, slight over- and underestimations can be observed. There is no systematic difference between the two geometries, while for $\nu = 1/2$ the correction works better for lenses for $\nu = 1/4$ a better description of ellipsoids is obtained. However, for highly anisotropic particles $\nu \leq 1/6$ the correction has no significant effect and also fails to correct the unphysical negative real gas factors Z.

In principle, this correction can only attempt to compensate effects of translational correlations as well as two-particle orientational correlations of the anisotropic shape considered by the second virial coefficient as a scaling factor. Seemingly, the role of orientational correlations have an increasing impact on the real gas factor with increasing anisotropy. As virial coefficients up to order $i = 8$ are considered, orientational correlations with lengthscales exceeding the dimension of an eight-particle cluster are present in the isotropic phase of hard ellipsoids and lenses. This provides evidence for the importance of so-far-unknown higher-order virial coefficients.

3.4.3 Generalised Carnahan-Starling relation

For hard spheres, a variety of heuristic correlations exist [111] to describe their equation of state. The accurate correlation of Kolafa *et al.* [112] uses up to

nine parameters. A simple generalised Carnahan-Starling equation

$$Z = \frac{1 + \gamma_0\,\varphi + \gamma_1\,\varphi^2 - \gamma_2\,\varphi^3}{(1-\varphi)^3} \tag{3.17}$$

can be used as a heuristic correlation to accurately describe the data calculated. Here the coefficient γ_0 is chosen as $\gamma_0 = B_2^* - 3$ to obtain the virial series as a low-density limit. The two further parameters γ_1 and γ_2 are determined via least-squares fits to calculated data in the isotropic phase. Results are compiled in Table II of [67] for ellipsoids and Table II in [68] for lenses.

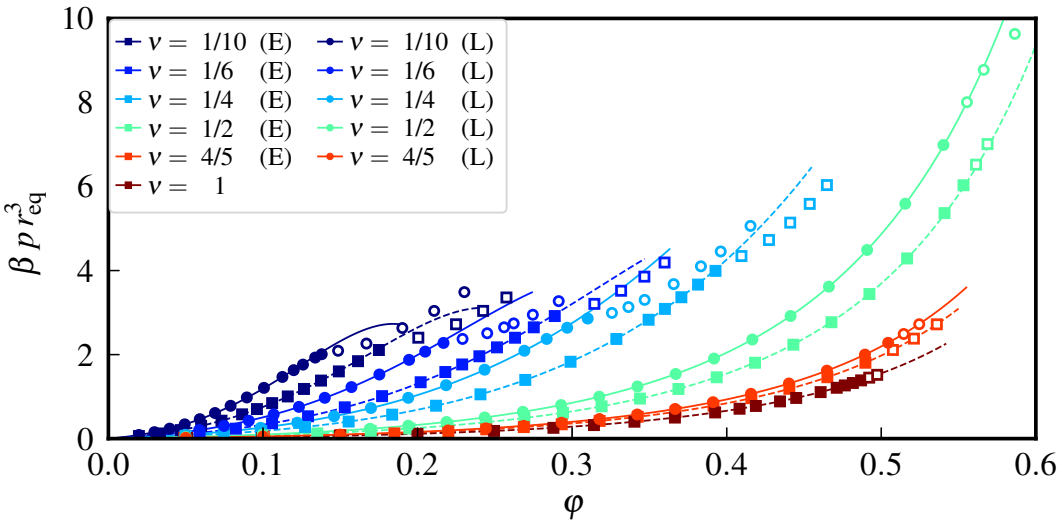

Fig. 3.6: Equation-of-state data for oblate Ellipsoids (E) and Lenses (L) described by a generalised Carnahan Starling relation according to Eq. (3.17) for selected aspect ratios. Squares are data from ellipsoids and circles from lenses while filled symbols are equation-of-state points in the isotropic phase and open symbols beyond the phase boundary.

This approach is shown in Fig. 3.6 for five selected anisotropic aspect ratios of both geometries as well as spheres for comparison. Thereby, the presented data is described astoundingly well by Eq. (3.17) for both geometries considering the simplicity of the approach. However, when examining the results in more detail, systematic deviations can be observed. This is exemplarily shown for ellipsoids with an aspect ratio $\nu = 1/3$ in Fig. 8 of [66].

3.4.4 Comparison of the investigated geometries

To investigate the influence of the detailed particle geometry it is useful to analyse the dimensionless real gas factor Z in dependence on the volume fraction φ as therewith quantities independent of the topological parameters are obtained. This is visualised in Fig. 3.7 for four selected aspect ratios. Although

the two geometries are in principle quite similar, significant differences can be observed. Interestingly, while the real gas factors of moderately anisotropic particles $\nu \geq 4/5$ are in first approximation identical, for higher anisotropies the real gas factor of hard lenses exceeds that of hard ellipsoids of revolution for the same volume fraction and aspect ratio. These differences are thereby more distinct for aspect ratios which exhibit an isotropic-nematic phase transition ($\nu \leq 1/3$).

This effect has also been observed for the reduced second virial coefficient, where with increasing anisotropy the reduced second virial coefficient $B_2^* = B_2/V_\mathrm{P}$ for lenses increasingly exceeds that of oblate ellipsoids of revolution [63]. This is caused by the contribution of the equatorial singularity to the mean radius of curvature which also is directly related to the excess part of the excluded volume.

The dependence of the two heuristic parameters γ_1 and γ_2 of Eq. (3.17) on the excess part α [Eq. (3.3)] is displayed in Fig. 10 in [68]. Here again, an in first approximation universal behaviour for both geometries investigated is observed. This is an additional indication that not only the higher-order virial coefficients but also the equation of state of hard oblate geometries are predominantly determined by the excess part of the excluded volume α.

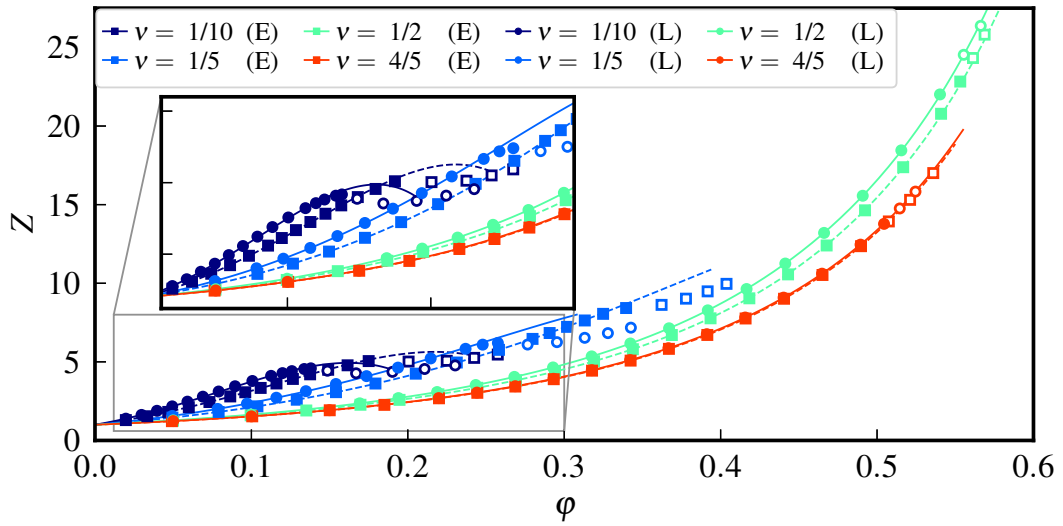

Fig. 3.7: Real gas factor Z in dependence on the volume fraction φ for selected aspect ratios of ellipsoids (circles) and lenses (squares). Data of the isotropic phase is shown by closed symbols while data beyond the phase transition is represented by open symbols. Lines correspond with the generalised Carnahan-Starling relation [Eq. (3.17)].

4 Summary and outlook

In this work, the equations of state of hard, anisotropic particles have been studied with a complementary virial series and cluster Monte Carlo simulation approach. For the calculation of virial coefficients, the Mayer-Sampling algorithm has been utilised and specifically optimised for hard-body interactions. Therefore, the required Ree-Hoover graphs were formulated as ordinal numbers allowing an efficient determination of the single contributing graph using a bisection search. The efficiency of this variant increases drastically with the increasing order of the virial coefficient. Additionally, a significant optimisation could be achieved by using highly branched trees as an intrinsic reference integral. As in this case, the identical geometry is used for the reference integrand, statistical fluctuations could be reduced significantly allowing a higher accuracy.

The algorithm presented was validated and applied to oblate hard ellipsoids of revolution and hard lenses allowing the calculation of virial coefficients of order three to eight. The analysis of the results obtained interestingly showed in first approximation a universal dependence of the reduced virial coefficients $\tilde{B}_i = B_i/B_2^{i-1}$ on the inverse scaled excess part α^{-1} of the excluded volume.

An extension of the algorithm developed to four-dimensional space allowed the calculation of virial coefficients of an anisotropic four-dimensional object for the first time. Here, the virial coefficients of order two to six of hard hyperspherocylinders were calculated. The analysis of the influence of the aspect ratio on the second virial coefficient and thus mutual excluded volume allowed the formulation of a conjecture for an analogue of the Isihara-Hadwiger theorem in $\mathbb{R}^4$. Interestingly, the hypervolume is in contrast to lower dimensions not an additive contribution to the excluded volume.

Additionally, a Monte Carlo simulation algorithm was developed to calculate equation-of-state data in the (N, p, T) ensemble employing a cluster scaling technique. It could be shown that this method allows the calculation of precise data for the isotropic phase of hard-particle systems. For anisotropic particles, the benefit increases as the efficiency gain is more relevant for complex overlap problems. However, an additional algorithm for the closest surface distance is required. On the work on ellipsoids, it could be shown that an approximation therefore is sufficient. The algorithm was also validated using the hard sphere and hard ellipsoid systems.

With this method, equation-of-state data for the isotropic phase was calculated for hard lenses and oblate hard ellipsoids of revolution from comparatively large ensembles with typically 1000 particles. Additionally, the phase boundaries of the isotropic phase were determined with the same method and similar system sizes.

Subsequently, the data calculated for both geometries was compared to the virial series considering the coefficients calculated up to order $i = 8$ allowing an analysis of truncation effects giving evidence for the importance of higher-order virial coefficients. It can be shown that the data of the isotropic phase

can be described reasonably well with a Parson-type truncation correction for moderate and intermediate anisotropies $\nu \geq 1/5$. This approach fails for higher anisotropies. Alternatively, the data is described with a generalised Carnahan-Starling type equation using in addition to the second virial coefficient two heuristic parameters. This approach describes all aspect ratios over a wide density range with astounding accuracy considering the simplicity of the approach. An analysis of the two heuristic parameters in dependence on the scaled excess part of the excluded volume α again showed in first approximation a geometry-independent, universal behaviour. This is a further indication that not only the virial coefficients but also the equation of state for oblate hard lenses and ellipsoids of revolution are in first approximation determined by the excess part of the excluded volume.

To fully understand the impact of the excess excluded volume further investigations of hard body systems are required. Specifically, prolate shapes such as ellipsoids or spherocylinders as well as biaxial geometries or other candidates without rotational symmetry are thereby of specific interest. To investigate the extent of orientational correlations at different lengthscales an analysis of directional-dependent orientational correlation functions might be a suitable approach.

5 Original Publications

This chapter contains four publications, three as first-author [66–68] and one as co-author [69]. Prior to each chapter, an overview listing the authors and their respective contributions is given. The four publications are:

Publication I, Full Paper

Calculation of third to eighth virial coefficients of hard lenses and hard, oblate ellipsoids of revolution employing an efficient algorithm
Philipp Marienhagen, Robert Hellmann, and Joachim Wagner,
Phys. Rev. E **104**, 015308 (2021).
DOI: 10.1103/PhysRevE.104.015308

Publication II, Full Paper

Reexamining equations of state of oblate hard ellipsoids of revolution: Numerical simulation utilizing a cluster Monte Carlo algorithm and comparison to virial theory
Philipp Marienhagen and Joachim Wagner,
Phys. Rev. E **105**, 014125 (2022).
DOI: 10.1103/PhysRevE.105.014125

Publication III, Full Paper

Virial coefficients of hard hyperspherocylinders in $\mathbb{R}^4$: Influence of the aspect ratio
Markus Kulossa, Philipp Marienhagen, and Joachim Wagner,
Phys. Rev. E **105**, 064121 (2022).
DOI: 10.1103/PhysRevE.105.064121

Publication IV, Full Paper

Equation of state of hard lenses: A combined virial series and simulation approach
Philipp Marienhagen and Joachim Wagner,
Phys. Rev. E **106**, 014101 (2022).
DOI: 10.1103/PhysRevE.106.014101

5.1 Publication I: Calculation of third to eighth virial coefficients of hard lenses and hard, oblate ellipsoids of revolution employing an efficient algorithm

Philipp Marienhagen, Robert Hellmann, and Joachim Wagner,
Phys. Rev. E **104**, 015308 (2021).
DOI: 10.1103/PhysRevE.104.015308.

Contribution:
This work was conceptualised by P.M. and J.W. Algorithms were developed by P.M and J.W. The graphs were generated by J.W. with valuable input from P.M. and R.H. Calculations were performed by P.M and J.W. Data was analysed by P.M. The draft was written by P.M and all authors contributed to the revision process. The work was supervised by J.W.

Calculation of third to eighth virial coefficients of hard lenses and hard, oblate ellipsoids of revolution employing an efficient algorithm

Philipp Marienhagen [1], Robert Hellmann [2] and Joachim Wagner [1,*]

[1] *Institut für Chemie, Universität Rostock, Albert-Einstein-Straße 3a, 18059 Rostock, Germany*

[2] *Institut für Thermodynamik, Helmut-Schmidt-Universität/Universität der Bundeswehr Hamburg, 22043 Hamburg, Germany*

(Received 21 May 2021; accepted 25 June 2021; published 19 July 2021)

We provide third to eighth virial coefficients of oblate, hard ellipsoids of revolution and hard lenses in dependence on their aspect ratio ν. Employing an algorithm optimized for hard anisotropic shapes, highly accurate data are accessible with comparatively small numerical effort. For both geometries, reduced virial coefficients $\tilde{B}_i(\nu) = B_i(\nu)/B_2^{i-1}(\nu)$ are in first approximation proportional to the inverse excess contribution α^{-1} of their excluded volume. The latter quantity is directly accessible from second virial coefficients and analytically known for convex bodies.

DOI: 10.1103/PhysRevE.104.015308

I. INTRODUCTION

Starting with the seminal work of Onsager [1], hard anisotropic solids attracted increasing interest as a model system for condensed matter, where a competition of entropy resulting from rotational and translational degrees of freedom determines the equation of state and therewith the phase behavior of such systems.

An obvious route to extend the spherically symmetric hard sphere model to anisotropic particles is the affine transformation to ellipsoids. In the special case of axial symmetry, ellipsoids of revolution are obtained with tunable aspect ratio ν as a single parameter of anisometry. Such systems are thoroughly investigated as model systems for liquid crystalline matter [2–5]. The influence of the detailed particle shape becomes evident comparing the phase behavior of ellipsoids and hard spherocylinders [6–8]. While ellipsoids and spherocylinders are continuous with respect to their surface curvature, lenses possess a two-dimensional discontinuity at their equators. The impact of such discontinuities to second virial coefficients is known [9]. Recently, the phase behavior of hard lenses has been investigated [10–12].

Much earlier, van der Waals [13], Jäger [14], and Boltzmann [15,16] used the excluded volume to calculate the virial coefficients of hard spheres up to order 4. Kamerlingh Onnes [17] proposed the virial series as an equation of state for gases and liquids, where orientational degrees of freedom average out. The fifth- and higher-order virial coefficients became accessible with emerging computer simulation techniques [18–20].

Using Monte Carlo methods and numerical approaches for the contact function of anisotropic hard solids, also third- and higher-order virial coefficients of such systems became available. In addition to spherocylinders [21,22], the virial coefficients of ellipsoids [2,3,23–27] up to order 7 were systematically determined for selected aspect ratios. For two aspect ratios, in addition virial coefficients of order 8 are available [28].

In this paper, virial coefficients up to order 8 for the oblate geometries hard lenses and hard ellipsoids of revolution are systematically determined in dependence on their aspect ratio.

II. VIRIAL COEFFICIENTS OF HARD SOLIDS

The virial coefficient of order i depends on the interactions in a cluster of i particles, which can for hard solids be exactly expressed in a pairwise additive representation,

$$V^{(i)} = \sum_i \sum_{j>i} V_{ij}, \tag{1}$$

where due to the absence of long-range interactions and the particles' impenetrability the pair interaction

$$V_{ij}(\mathbf{r}_{ij}, \hat{\mathbf{u}}_i, \hat{\mathbf{u}}_j) = \begin{cases} 0 & : \quad r_{ij} \geqslant r_c(\hat{\mathbf{r}}_{ij}, \hat{\mathbf{u}}_i, \hat{\mathbf{u}}_j) \\ \infty & : \quad r_{ij} < r_c(\hat{\mathbf{r}}_{ij}, \hat{\mathbf{u}}_i, \hat{\mathbf{u}}_j) \end{cases} \tag{2}$$

is either zero when both particles do not overlap or infinity when both particles intersect. At the contact distance $r_c(\hat{\mathbf{r}}_{ij}, \hat{\mathbf{u}}_i, \hat{\mathbf{u}}_j)$, two particles i and j touch when their orientation is given by the unit vectors $\hat{\mathbf{u}}_i$ and $\hat{\mathbf{u}}_j$ and the direction $\hat{\mathbf{r}}_{ij} = \mathbf{r}_{ij}/r_{ij}$ of their center of mass distance vector $\mathbf{r}_{ij}$.

The Mayer f function $f_{ij}(V_{ij}) = \exp(-V_{ij}/k_\mathrm{B}T) - 1$ vanishes for a nonoverlap configuration and is $f_{ij} = -1$ when particles i and j intersect, i.e.,

$$f_{ij}(\mathbf{r}_{ij}, \hat{\mathbf{u}}_i, \hat{\mathbf{u}}_j) = \begin{cases} 0 & : \quad r_{ij} \geqslant r_c(\hat{\mathbf{r}}_{ij}, \hat{\mathbf{u}}_i, \hat{\mathbf{u}}_j) \\ -1 & : \quad r_{ij} < r_c(\hat{\mathbf{r}}_{ij}, \hat{\mathbf{u}}_i, \hat{\mathbf{u}}_j) \end{cases}. \tag{3}$$

Since the energy is either zero or infinity, the Mayer f function and as a consequence the virial coefficients of hard body systems are independent of thermal energy $k_\mathrm{B}T$.

The virial coefficient of order i

$$B_i = -\frac{i-1}{i!} \sum_{G \in \mathbb{M}_i^\mathrm{L}} S_G \tag{4}$$

*joachim.wagner@uni-rostock.de

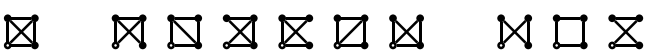

FIG. 1. Biconnected Mayer graphs with four nodes contributing to the fourth virial coefficient. The ten existing labeled graphs can be subdivided into three topological classes. The first node is represented by an open circle, at lower left, followed by three nodes labeled in counterclockwise direction.

is the sum of integrals S_G over products of Mayer f functions represented by the edges of graphs G in the set of biconnected or nonseparable labeled graphs $\mathbb{M}_i^{\mathrm{L}}$ with i nodes, called Mayer graphs. We have

$$B_2 = -\frac{1}{2V}\iint \langle f_{12}\rangle_{\hat{\mathbf{u}}_2} d^3\mathbf{r}_1 d^3\mathbf{r}_2 = -\frac{1}{2}$$  (5a)

$$B_3 = -\frac{1}{3V}\iiint \langle f_{12}f_{13}f_{23}\rangle_{\hat{\mathbf{u}}_2,\hat{\mathbf{u}}_3} d^3\mathbf{r}_1 d^3\mathbf{r}_2 d^3\mathbf{r}_3 = -\frac{1}{3}$$ 

$$\vdots \qquad (5b)$$

where $\langle\ldots\rangle_{\hat{\mathbf{u}}_2,\ldots,\hat{\mathbf{u}}_i}$ indicates the average over the orientations of the second to ith particle, while the position $\mathbf{r}_1$ and orientation $\hat{\mathbf{u}}_1$ of the first particle determine the coordinate system.

While for the second and third virial coefficient, i.e., clusters of two or three particles, only one biconnected graph exists, already ten labeled graphs (Fig. 1) contribute to the fourth virial coefficient and 238 contribute to the fifth. The number of labeled biconnected graphs with i nodes can be found in Ref. [29].

The reformulation of Ree and Hoover [19,20,30] reduces the number of labeled graphs roughly to one third of the labeled Mayer graphs by introduction of a new type of bond $e_{ij} = f_{ij} + 1$. The resulting Ree-Hoover graphs are fully connected either by f bonds or e bonds as exemplarily shown for the fourth virial coefficient in Fig. 2. Since for hard solids we have

$$e_{ij}(\mathbf{r}_{ij}, \hat{\mathbf{u}}_i, \hat{\mathbf{u}}_j) = \begin{cases} 1 & : \quad r_{ij} \geqslant r_c(\hat{\mathbf{r}}_{ij}, \hat{\mathbf{u}}_i, \hat{\mathbf{u}}_j) \\ 0 & : \quad r_{ij} < r_c(\hat{\mathbf{r}}_{ij}, \hat{\mathbf{u}}_i, \hat{\mathbf{u}}_j) \end{cases}, \qquad (6)$$

e_{ij} vanishes in the case of an intersection ($f_{ij} = -1$) and f_{ij} vanishes for nonintersecting particles ($e_{ij} = 1$). Hence, for a given configuration of overlaps and nonoverlaps only a single Ree-Hoover graph contributes to the integrand [31].

FIG. 2. Two topological classes of labeled Ree-Hoover graphs with four nodes and nonzero Ree-Hoover star contents contributing to the fourth virial coefficient exist. Ree-Hoover graphs are fully connected either via Mayer f bonds (black lines) or e bonds (red lines). The star contents as weighting factors result by replacing missing connections in Mayer graphs by a factor $(e_{ij} - f_{ij}) = 1$. Six remaining but noncontributing Ree-Hoover graphs with a single e bond are not displayed.

Using the Ree-Hoover reformulation, the virial coefficient of order i reads as

$$B_i = -\frac{i-1}{i!}\sum_{G\in\mathbb{R}_i^{\mathrm{L}}} c_G S_G, \qquad (7)$$

where $\mathbb{R}_i^{\mathrm{L}}$ is the set of labeled Ree-Hoover graphs with i vertices. The weighting factors c_G, called Ree-Hoover star contents, depend on the topology of the graphs in $\mathbb{R}_i^{\mathrm{L}}$.

Since in a Ree-Hoover graph any combination of two nodes is either connected via a Mayer f bond or an e bond, its topology can be memory-efficiently represented as a binary number related to the upper triangle of its adjacency matrix, where $i(i-1)/2$ bits are needed for a graph with i nodes. Herewith, Ree-Hoover graphs can be represented as ordinal numbers and thus be sorted. Based on the number of overlaps n_o and nonoverlaps $i(i-1)/2 - n_o$, a preclassification of possible graphs with a given number of f bonds is possible. In an ordered array of ordinal numbers, by means of a bisection search the single contributing graph and its star content can be identified very efficiently. The complexity of a bisection search scales as $\log_2 N(i, n_o)$, where $N(i, n_o)$ is the cardinality of the set of Ree-Hoover graphs with i nodes and n_o f bonds. Hence, a bisection search for virial coefficients of order 5 and higher is much faster than classical computation using integer arithmetic. The integrand resulting from such an identified configuration reads as $(-1)^{n_o} c_G$, since each f bond contributes as a factor of $f_{ij} = -1$ for an overlap between particles i and j and each e bond as a factor of $e_{ij} = 1$ in the case of a nonoverlap.

However, due to the highly increasing number of labeled Ree-Hoover diagrams, this method is restricted to virial coefficients up to order 9 using state-of-the-art hardware: for the binary representation of 21 286 987 064 labeled Ree-Hoover diagrams with nine nodes, where for each graph 5 bytes are necessary, roughly 100 GB of memory are required plus another 40 GB for the corresponding star contents. For even higher-order virial coefficients, the method of Wheatley is the fastest approach [32].

A. Importance sampling

Calculating a virial coefficient of order i for an anisotropic solid of revolution requires numerical integration in $5(i-1)$-dimensional space, with three translational and two rotational degrees of freedom for each, except the first particle. Importance sampling can significantly improve the sampling of the configurational space where integrands are large. Singh and Kofke [33] proposed the Mayer-sampling method, where the acceptance of a trial is determined by the ratio of the system's integrand in subsequent configurations. Since in this approach the configuration space is no longer explored at constant sampling density, the comparison with a known integral of a reference system sampled at identical points of the configuration space is required in addition.

For a hard body system, i.e., a system with discontinuous f and e functions, which is sampled with a hard-body reference system of different shape, the situation can occur that the system's integrand is zero when the reference's integrand is nonzero. If the acceptance solely would be governed by the system's integrand, contributions to the reference integrand in

such configurations would not be sampled. Then, the accessible configuration space of the reference system would not be a subset of the system of interest's accessible configuration space and importance sampling would fail. To facilitate that the union of accessible configuration spaces of both system of interest and reference is sampled exhaustively, the acceptance of a Monte Carlo trial in this paper is determined by the sum of moduli of sample and reference integrands. A weighting factor is adjusted during equilibration guaranteeing the same average moduli of system and reference integrands. Thus, both integrands contribute on average with equal weights to the acceptance of a trial.

B. Trees as an intrinsic reference

Since virial coefficients of hard spheres are the most accurate reference and the determination of overlaps of spheres is fast and simple, hard spheres scaled to the same volume as the particles of interest are an obvious reference system. Here, the virial coefficient of hard spheres or a diagram with known value can be used.

The efficiency of the Mayer-sampling method increases if the geometric shapes of the system of interest and reference system are as similar as possible. However, using anisotropic particles as a reference increases the numerical effort tremendously as a consequence of the orientation-dependent overlap problem. In addition, the accuracy of available virial coefficients is significantly smaller than that of hard sphere systems.

Both obstacles can be circumvented using trees with i nodes and $i-1$ Mayer f bonds as an intrinsic reference for the virial coefficient of order i. The number of labeled trees with i nodes is i^{i-2}. Since these graphs do not contain any leaves and all f bonds are connected via articulation points, they factorize to powers of the second virial coefficient. Each tree with i nodes and $i-1$ Mayer f bonds can be written as $(-2B_2)^{i-1}$. For convex hard bodies, B_2 is analytically known employing the Isihara-Hadwiger theorem [9]. Even if the second virial coefficient is not analytically known in the case of concave bodies, it can numerically be determined with high accuracy.

If a set of trees with i nodes and $i-1$ f bonds of cardinality N_T is used as an intrinsic reference, the value of the reference integral reads as

$$I_\mathrm{ref} = N_\mathrm{T}(-2\,B_2)^{i-1}. \tag{8}$$

With known overlaps and nonoverlaps in a given configuration, the reference integrand is the number of trees whose f bonds are a subset of the configuration's nonzero f bonds. Although the number of trees does not increase as dramatically with the order of the virial coefficient as the number of Ree-Hoover diagrams, numerous trees with i nodes exist for high-order virial coefficients.

However, it is sufficient to use only those trees whose Mayer f bonds are most frequently a subset of the Ree-Hoover diagram's f bonds. This is the case for the most branched trees, i.e., trees with nodes of highest order. In this paper, we used for the virial coefficient of order i trees with one node of order $i-1$ and $i-1$ nodes of order 1. This topological class consists of i labeled trees. For example,

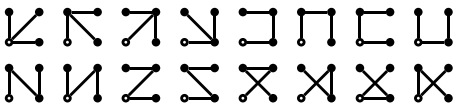

FIG. 3. Labeled trees with four nodes and three Mayer f bonds. Two topological classes with orders (3,1,1,1) and (2,2,1,1) can be distinguished. Since all Mayer f bonds of these trees are connected via articulation points, the value of each diagram is $-8B_2^3$.

to calculate the fourth virial coefficient, the first four trees displayed in Fig. 3 are used.

III. OVERLAP CRITERIA FOR HARD ELLIPSOIDS AND HARD LENSES

A. Ellipsoid

Overlaps between ellipsoids can be identified using the algorithm proposed by Perram and Wertheim [34]. Since a numerical maximization is involved, the algorithm can be optimized employing a Newton-Raphson maximization instead of the Brent maximization originally proposed by the authors.

B. Lens

A lens is the section of two spheres with radii R_0 whose centers are less than their diameter $2R_0$ apart from each other. The radius R_0 of spheres generating a lens with equatorial radius r_eq and aspect ratio ν is

$$R_0 = \frac{\nu^2+1}{2\nu} r_\mathrm{eq}, \tag{9}$$

as illustrated in Fig. 4.

The equator at $z=0$ is a two-dimensional singularity of surface curvature for $\nu < 1$. In contrast, the surface curvature of ellipsoids is completely continuous. In the limits $z \to 0^+$ and $z \to 0^-$, the tangents enclose the critical angle $\vartheta_\mathrm{crit} = \arccos[(1-\nu^2)/(1+\nu^2)]$ with the lens's equatorial plane.

Choosing $r_\mathrm{eq} = 1$, two lenses i and j possibly intersect with a center to center distance $r_{ij} < 2$. With $r_{ij} < 2\nu$, they definitely intersect. For $2\nu < r_{ij} < 2$, an intersection is possible

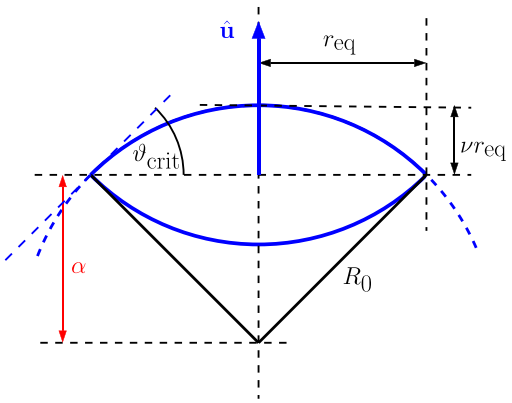

FIG. 4. A lens is the section of two spheres with center to center distance less than their diameter $2R_0$, where r_eq is the lens's equatorial radius and ν is its aspect ratio. Its orientation is denoted by the unit vector $\hat{\mathbf{u}}$ perpendicular to its equatorial plane.

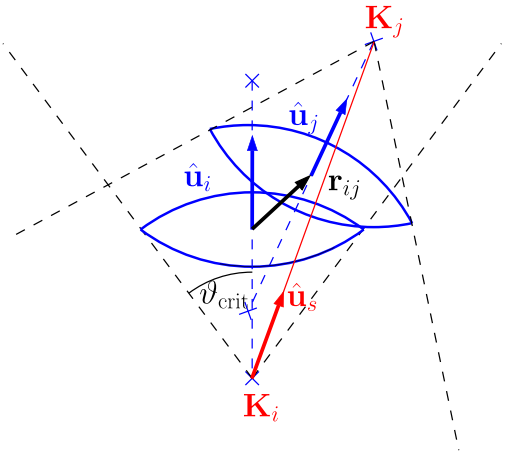

FIG. 5. Undercritically inclined lenses with $|\hat{\mathbf{u}}_i \cdot \hat{\mathbf{u}}_s| > \zeta$ and $|\hat{\mathbf{u}}_j \cdot \hat{\mathbf{u}}_s| > \zeta$, where $\zeta = (1-\nu^2)/(1+\nu^2)$ denotes the cosine of the critical angle ϑ_{crit}. Undercritically inclined lenses do not touch at a singularity of surface curvature at their equators.

if a generating sphere of lens i intersects with a generating sphere of lens j.

Let $\hat{\mathbf{u}}_i$ and $\hat{\mathbf{u}}_j$ be the orientations of lenses i and j with each vector being perpendicular to its equatorial plane. Without loss of generality, we can choose $\mathbf{r}_i = \mathbf{0}$ and $\hat{\mathbf{u}}_i$ defining the z direction of the coordinate system. Thus, the generating spheres of a lens with center of mass $\mathbf{r}_i$ are located at

$$\mathbf{c}_{i\pm} = \mathbf{r}_i \pm \alpha \hat{\mathbf{u}}_i, \tag{10}$$

where $\alpha = R_0 - \nu r_{\text{eq}}$ is the distance of the sphere center to the lens's equatorial plane.

An intersection of two lenses i and j is possible if at least one of four possible distances $\|\mathbf{c}_{j\pm} - \mathbf{c}_{i\pm}\| < 2R_0$ is smaller than the diameter $2R_0$ of generating spheres. An intersection, however, occurs if and only if at least one point of the generating spheres' intersection simultaneously is inside both lenses i and j.

An intersection can be proven or excluded by the following tests. The closest surface to surface distance between two nonintersecting lenses occurs between the most distant generating spheres of both lenses. In a first step, let us look for the maximum of

$$d_{\max} = \max \|\mathbf{r}_{ij} \pm \alpha \hat{\mathbf{u}}_j \mp \alpha \hat{\mathbf{u}}_i\|. \tag{11}$$

Let $\mathbf{K}_i$ and $\mathbf{K}_j$ be the centers of generating spheres of lens i and lens j with the distance $d_{\max} = \|\mathbf{K}_j - \mathbf{K}_i\|$. Let further $\hat{\mathbf{u}}_s = (\mathbf{K}_j - \mathbf{K}_i)/\|\mathbf{K}_j - \mathbf{K}_i\|$ be the direction of the distance vector and $\zeta = (1-\nu^2)/(1+\nu^2)$ the cosine of the critical angle ϑ_{crit}. If simultaneously $|\hat{\mathbf{u}}_i \cdot \hat{\mathbf{u}}_s| > \zeta$ and $|\hat{\mathbf{u}}_j \cdot \hat{\mathbf{u}}_s| > \zeta$, $\mathbf{K}_j$ is in the critical cone of lens i and $\mathbf{K}_i$ is in the critical cone of lens j. Then, both lenses are undercritically inclined to each other (Fig. 5). In this case, the equatorial circles of both lenses are not in their section.

Undercritically inclined lenses intersect if $\mathbf{K}_i + R_0 \hat{\mathbf{u}}_s$ is inside lens j or $\mathbf{K}_j - R_0 \hat{\mathbf{u}}_s$ is inside lens i and otherwise not. Hence, an intersection is excluded for undercritically inclined lenses if $d_{\max} > 2R_0$.

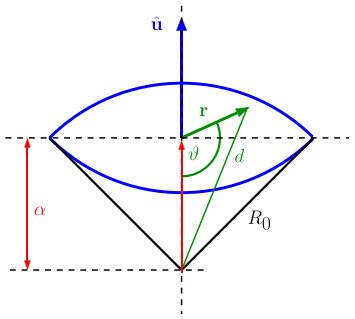

FIG. 6. A point $\mathbf{r}$ is inside a lens if its distance to the generating sphere's center is smaller than the radius R_0 of the generating sphere.

For overcritically inclined lenses, we need to check if the nearest point of lens i's equator to $\mathbf{K}_j$ is inside lens j or the nearest point of lens j's equator to $\mathbf{K}_i$ is inside lens i. The two points of interest are

$$\mathbf{P}_i = \mathbf{r}_i + r_{\text{eq}} \frac{\hat{\mathbf{u}}_i \times [(\mathbf{K}_j - \mathbf{r}_i) \times \hat{\mathbf{u}}_i]}{\|\hat{\mathbf{u}}_i \times [(\mathbf{K}_j - \mathbf{r}_i) \times \hat{\mathbf{u}}_i]\|} \tag{12a}$$

and

$$\mathbf{P}_j = \mathbf{r}_j + r_{\text{eq}} \frac{\hat{\mathbf{u}}_j \times [(\mathbf{K}_i - \mathbf{r}_j) \times \hat{\mathbf{u}}_j]}{\|\hat{\mathbf{u}}_j \times [(\mathbf{K}_i - \mathbf{r}_j) \times \hat{\mathbf{u}}_j]\|}. \tag{12b}$$

Finally, we have to check if the equator circles of both lenses intersect. This is only possible if the intersection line of the planes containing the equators of the respective lenses intersects both equator circles. The sufficient condition for an overlap of lenses is fulfilled when both obtained line segments overlap. This is the case when the intervals $[x_1^{(i)}, x_2^{(i)}]$ and $[x_1^{(j)}, x_2^{(j)}]$ overlap, where $x_1^{(i)}$ and $x_2^{(i)}$ are solutions of $\mathbf{r}^{\mathrm{T}} \cdot \mathbf{r} = 1$ and $x_1^{(j)}$ and $x_2^{(j)}$ are solutions of $(\mathbf{r} - \mathbf{r}_j)^{\mathrm{T}} \cdot (\mathbf{r} - \mathbf{r}_j) = 1$ under the constraint $\mathbf{r}^{\mathrm{T}} \cdot \hat{\mathbf{u}}_j = 0$ with $\mathbf{r} = (x, y, 0)$ in the coordinate system defined by lens i.

The required tests of whether a point of interest $\mathbf{r}$ is inside or outside a lens centered at $\mathbf{c}$ with orientation $\hat{\mathbf{u}}$ can be done as follows: Let us again without loss of generality choose $\mathbf{c} = \mathbf{0}$. A point is inside a lens if its distance to the generating sphere's center is smaller than R_0 (Fig. 6). With $\vartheta = \pi - \arccos(\hat{\mathbf{r}} \cdot \hat{\mathbf{u}})$, where $\hat{\mathbf{r}}$ and $\hat{\mathbf{u}}$ are unit vectors indicating the direction of $\mathbf{r}$ and lens orientation $\hat{\mathbf{u}}$, we obtain

$$\begin{aligned} d^2 &= \alpha^2 + r^2 - 2\alpha r \cos[\pi - \arccos(\mathbf{r} \cdot \hat{\mathbf{u}})] \\ &= \alpha^2 + r^2 + 2\alpha \mathbf{r} \cdot \hat{\mathbf{u}}. \end{aligned} \tag{13}$$

Should $\mathbf{r}$ be located at the lower hemilens when $\mathbf{r} \cdot \hat{\mathbf{u}} < 0$, the edge d of a triangle containing the sphere center above the lens's equatorial plane as a corner decides if $\mathbf{r}$ is inside or outside the lens. Hence, $\mathbf{r}$ is inside the lens whenever

$$\alpha^2 + r^2 + 2\alpha |\mathbf{r} \cdot \hat{\mathbf{u}}| < R_0^2. \tag{14}$$

As the above described overlap algorithm does not contain any iterative numerical step, checking overlaps of lenses is significantly faster than checking overlaps of ellipsoids.

The comparison of second virial coefficients obtained from numerical integration employing the above described overlap algorithm with the analytical result proves its reliability:

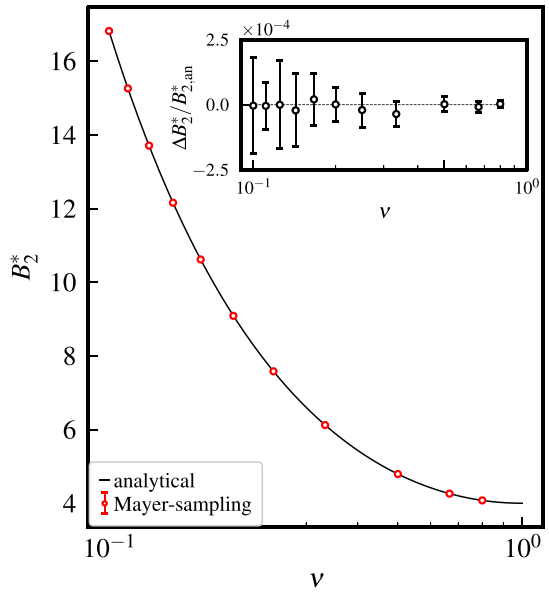

FIG. 7. Comparison of reduced second virial coefficients $B_2^* = B_2/V_\mathrm{P}$ of hard lenses obtained numerically with the respective analytical values. The numerical integration is performed via Mayer sampling using hard spheres as a reference, where the spheres are scaled to obtain a sphere volume identical to the lens volume. In the inset, relative deviations $\Delta B_2^* = (B_2^* - B_{2,\mathrm{an}}^*)/B_{2,\mathrm{an}}^*$ from the analytical values are displayed.

within experimental uncertainties, results from Mayer sampling agree with the analytical values (Fig. 7). Here, the second virial coefficient of hard spheres with volume identical to the lens volume is used as a reference.

IV. RESULTS

Despite the geometric similarity between oblate ellipsoids of revolution and lenses, the latter shape differs from ellipsoids by a two-dimensional equatorial discontinuity in its surface curvature. In addition, at the same equatorial radius r_eq and aspect ratio ν, both volume and surface of lenses are smaller than those of ellipsoids. As a consequence of the discontinuity of curvature, however, for $\nu < 1$ the strongly increasing mean curvature radius of lenses overcompensates the drop of volume and surface: with decreasing aspect ratio ν, the second virial coefficient of lenses increasingly exceeds that of oblate uniaxial ellipsoids [9].

As in the limit $\nu \to 1$ both geometries approach a sphere, the comparison of virial coefficients of lenses and ellipsoids with aspect ratio $\nu = 1$ with literature data of hard spheres is a test for the reliability of our algorithm optimized for hard anisotropic shapes. The excellent accordance of our data with reference values from [35] can be seen from the compilation in Table I. Since the scope of this paper is a systematic, aspect ratio dependent comparison of both geometries' virial coefficients, the data for the limiting case of spheres obtained by comparatively short simulations do not reflect a principal limitation of our algorithm in terms of accuracy.

Reduced virial coefficients $\tilde{B}_i = B_i/B_2^{i-1}$ calculated by means of the above described algorithm are compiled for oblate ellipsoids of revolution in Table II and for lenses in Table III. For both investigated geometries, the dependence of virial coefficients on the aspect ratio decreases with increasing order of the virial coefficient.

Our data for hard ellipsoids are in excellent agreement with data previously published from order 3 to 7 in Ref. [27]. The accuracy, however, could be improved by our algorithm. For moderately anisotropic particles, eighth-order virial coefficients could be accessed with acceptable accuracy. Since for highly anisotropic shapes small rotations influence the number of overlaps in a cluster drastically, exhaustive sampling of the configuration space is hampered in the case of large anisotropy. Hereby, the fluctuations of virial coefficients during Mayer sampling significantly increase, leading to uncertainties in the magnitude of the observable itself. As a consequence, for $\nu \leqslant 1/7$ only a limit for the eighth virial coefficients' moduli could be obtained. In Ref. [28] two virial coefficients of order 8 for ellipsoids of moderate aspect ratio are reported which could not be reproduced in terms of either value or uncertainty. As reported in Ref. [36], only a subset of possible diagrams was utilized for the calculation of these two virial coefficients.

For three-dimensional hard, convex bodies, Boublík [37] proposed the quantity α^{-1}, which is proportional to the mutual excluded volume, as a geometric measure, leading to comparatively simple correlations to the reduced virial coefficients $\tilde{B}_i = B_i/B_2^{i-1}$. In three dimensions, for convex shapes the excess part of the mutual excluded volume can, employing the Isihara-Hadwiger theorem [38] with the volume V_P, the

TABLE I. Second to eighth virial coefficients of hard spheres [35] and hard ellipsoids of revolution and lenses with aspect ratio $\nu = 1$ (this paper). In the limit $\nu \to 1^-$, both anisotropic shapes approach a sphere. $\Delta^{(\mathrm{ell})} = (B_i^{*,(\mathrm{ell})} - B_i^{*,(\mathrm{sph})})/B_i^{*,(\mathrm{sph})}$ and $\Delta^{(\mathrm{lens})} = (B_i^{*,(\mathrm{lens})} - B_i^{*,(\mathrm{sph})})/B_i^{*,(\mathrm{sph})}$ are relative deviations from literature data of hard spheres. The values in parentheses indicate the standard deviations of at least eight independent runs, each with 2×10^{10} Monte Carlo steps.

	Spheres	Ellipsoids ($\nu = 1$)	$\Delta^{(\mathrm{ell})}$	Lenses ($\nu = 1$)	$\Delta^{(\mathrm{lens})}$
B_2^*	4				
B_3^*	10	10.0002(3)	2.0×10^{-5}	9.9999(7)	-1.0×10^{-5}
B_4^*	18.3647684...	18.365(2)	1.3×10^{-5}	18.364(1)	-4.2×10^{-5}
B_5^*	28.224437(15)	28.224(7)	-2.9×10^{-5}	28.23(1)	2.0×10^{-4}
B_6^*	39.81523(10)	39.80(3)	-3.8×10^{-4}	39.81(2)	-1.3×10^{-4}
B_7^*	53.34208(49)	53.3(1)	-1.1×10^{-3}	53.3(2)	-7.9×10^{-4}
B_8^*	68.5285(28)	68.6(6)	1.0×10^{-3}	68.5(4)	-4.2×10^{-4}

TABLE II. Reduced third to eighth virial coefficients $\tilde{B}_i = B_i/B_2^{i-1}$ of oblate, hard ellipsoids of revolution. The values in parentheses indicate the standard deviations of at least eight independent runs, each with 2×10^{10} Monte Carlo steps.

ν	$\tilde{B}_3$	$\tilde{B}_4$	$\tilde{B}_5$	$\tilde{B}_6$	$\tilde{B}_7$	$\tilde{B}_8$
1	0.624998(46)	0.286935(17)	0.110260(38)	0.038874(21)	0.013079(41)	0.004183(25)
4/5	0.621429(22)	0.281755(18)	0.106449(41)	0.036954(19)	0.012247(26)	0.004693(210)
2/3	0.613817(30)	0.270539(32)	0.098223(25)	0.032895(41)	0.010623(30)	0.003342(76)
1/2	0.595464(35)	0.243124(25)	0.078313(43)	0.023378(35)	0.007081(13)	0.002078(68)
1/3	0.562854(29)	0.194102(25)	0.043556(36)	0.008142(77)	0.002143(38)	0.000657(90)
1/4	0.539669(37)	0.159003(35)	0.019600(32)	−0.001217(79)	−0.000142(54)	0.000248(70)
1/5	0.523263(35)	0.134251(29)	0.003238(25)	−0.006938(111)	−0.001224(43)	0.000118(95)
1/6	0.511319(17)	0.116317(31)	−0.008217(46)	−0.010571(94)	−0.001819(26)	0.000111(87)
1/7	0.502348(27)	0.102906(26)	−0.016542(35)	−0.012959(179)	−0.001915(55)	0.000077(250)
1/8	0.495413(32)	0.092570(28)	−0.022834(50)	−0.014566(54)	−0.001993(76)	−0.000016(187)
1/9	0.489884(32)	0.084401(24)	−0.027656(49)	−0.015730(100)	−0.001882(109)	0.000043(270)
1/10	0.485403(26)	0.077811(24)	−0.031481(34)	−0.016480(72)	−0.001853(22)	0.000064(268)

surface S_P, and the mean radius of curvature $\tilde{R}$, be written as

$$\alpha = \frac{B_2 - V_\mathrm{P}}{3V_\mathrm{P}} = \frac{B_2^* - 1}{3} = \frac{S_\mathrm{P}\tilde{R}_\mathrm{P}}{3V_\mathrm{P}}, \tag{15}$$

where the factor $1/3$ guarantees $0 < \alpha^{-1} \leqslant 1$ with $\alpha^{-1} = 1$ being the upper limit for hard spheres. The geometric measures V_P, S_P, and $\tilde{R}_\mathrm{P}$ for hard lenses and oblate ellipsoids of revolution are provided in the Appendix.

At first approximation, for both investigated shapes an identical dependence of reduced virial coefficients $\tilde{B}_i$ on the geometric measure α^{-1} emerges as visible in Figs. 8 and 9.

For reduced virial coefficients $\tilde{B}_3$, $\tilde{B}_4$, and $\tilde{B}_5$, a nearly linear dependence is obtained. For the higher orders $\tilde{B}_6$, $\tilde{B}_7$, and $\tilde{B}_8$, a generalized, nonlinear dependence is visible, which can be reasonably approximated by parabolas (Fig. 9). The limitation of this parabolic approximation can be identified by deviations of this approximation to the data exceeding their uncertainties. This is also reflected by the optimum parameters of least-squares fits to a polynomial,

$$\tilde{B}_i(\alpha^{-1}) = a_{0,i} + a_{1,i}\alpha^{-1} + a_{2,i}\alpha^{-2}, \tag{16}$$

where the intercepts $a_{0,i}$ are quite similar for lenses and ellipsoids. The curvatures $a_{2,i}$ of ellipsoids, however, exceed those of lenses, while the linear coefficients $a_{1,i}$ of lenses are larger than those of ellipsoids (Fig. 10 and Table IV).

V. EQUATION OF STATE

With the virial series the real gas factor reads as

$$\begin{aligned} Z = \frac{p}{k_\mathrm{B}T\varrho} &= 1 + B_2\varrho + B_3\varrho^2 + \cdots \\ &= 1 + \sum_{i=2}^{\infty} B_i\varrho^{i-1}, \end{aligned} \tag{17}$$

where $k_\mathrm{B}T$ denotes the thermal energy and ϱ denotes the particle number density. With the volume V_P of a hard body, the volume fraction can be written as $\varphi = \varrho V_\mathrm{P}$. Employing reduced virial coefficients $B_i^* = B_i/V_\mathrm{P}^{i-1}$, the real gas factor can be reformulated as

$$Z = \frac{pV_\mathrm{P}}{k_\mathrm{B}T\varphi} = 1 + \sum_{i=2}^{\infty} B_i^*\varphi^{i-1}. \tag{18}$$

The reduced virial coefficients B_i^* of hard spheres can for $i \geqslant 2$ be approximated by the Carnahan-Starling series as $B_i^* \approx i^2 + i - 2$ [39]. The reason why this approximation

TABLE III. Reduced third to eighth virial coefficients $\tilde{B}_i = B_i/B_2^{i-1}$ of hard lenses. The values in parentheses indicate the standard deviations of at least eight independent runs, each with 2×10^{10} Monte Carlo steps.

ν	$\tilde{B}_3$	$\tilde{B}_4$	$\tilde{B}_5$	$\tilde{B}_6$	$\tilde{B}_7$	$\tilde{B}_8$
1	0.625012(21)	0.286957(28)	0.110249(29)	0.038867(27)	0.013009(27)	0.004187(36)
4/5	0.620911(35)	0.280841(33)	0.105628(46)	0.036445(43)	0.011946(17)	0.003786(77)
2/3	0.611414(43)	0.266666(21)	0.095071(30)	0.031080(41)	0.009732(20)	0.002932(98)
1/2	0.588039(11)	0.231810(35)	0.069868(22)	0.019239(39)	0.005436(39)	0.001468(86)
1/3	0.549095(31)	0.173328(22)	0.029403(43)	0.002691(24)	0.000916(73)	0.000571(80)
1/4	0.524367(29)	0.135765(19)	0.004218(31)	−0.006408(50)	−0.000861(145)	0.000340(158)
1/5	0.508397(29)	0.111646(18)	−0.011454(37)	−0.011596(25)	−0.001656(42)	0.000360(170)
1/6	0.497563(31)	0.095327(39)	−0.021663(34)	−0.014575(49)	−0.001943(147)	0.000287(82)
1/7	0.489793(40)	0.083754(40)	−0.028697(47)	−0.016477(92)	−0.002043(122)	0.000198(214)
1/8	0.483953(38)	0.075178(33)	−0.033683(55)	−0.017556(69)	−0.002093(83)	0.000221(197)
1/9	0.479431(44)	0.068622(38)	−0.037424(42)	−0.018290(75)	−0.002058(101)	0.000230(226)
1/10	0.475858(18)	0.063396(28)	−0.040296(65)	−0.018748(47)	−0.001815(104)	0.000257(120)

TABLE IV. Optimum parameters $a_{0,i}$, $a_{1,i}$, and $a_{2,i}$ of Eq. (16) describing the dependence of the reduced virial coefficients $\tilde{B}_i$ on the inverse excess part of the excluded volume α^{-1} for orders $i = 3$ to 8. The values in parentheses indicate the standard deviations of the parameters determined via weighted least squares fits.

	Ellipsoid			Lens		
i	a_0	a_1	a_2	a_0	a_1	a_2
3	0.44274(17)	0.17047(63)	0.01157(50)	0.43979(96)	0.1877(43)	−0.0011(39)
4	0.01352(32)	0.2561(12)	0.01730(95)	0.0088(19)	0.2804(72)	−0.0014(56)
5	−0.06831(55)	0.13820(20)	0.0405(15)	−0.0739(17)	0.1629(67)	0.0224(55)
6	−0.02316(31)	0.0141(11)	0.04794(85)	−0.02576(75)	0.0246(27)	0.0401(21)
7	0.00112(8)	−0.01986(31)	0.03174(26)	0.00027(25)	−0.01616(94)	0.02882(72)
8	0.00252(49)	−0.0115(15)	0.0132(11)	0.00184(35)	−0.0090(13)	0.01130(99)

works surprisingly well is still not understood [40]. Using the obvious condition $0 \leqslant \varphi < 1$, for the geometric series

$$\sum_{i=2}^{\infty}(i^2+i-2)\varphi^{i-1} = \frac{2\varphi(2-\varphi)}{(1-\varphi)^3}, \tag{19}$$

a closed expression is obtained. Herewith, the Carnahan-Starling real gas factor

$$Z = 1 + \frac{2\varphi(2-\varphi)}{(1-\varphi)^3} \tag{20}$$

of hard spheres results.

Introducing reduced virial coefficients normalized to powers of the second virial coefficients $\tilde{B}_i = B_i^*/(B_2^*)^{i-1}$, the expression

$$Z = 1 + \sum_{i=2}^{\infty}\tilde{B}_i(B_2^*\varphi)^{i-1} \tag{21}$$

is obtained for the real gas factor Z. Note that for a convergent sum in Eq. (21) $B_2^*\varphi < 1$ is not necessarily required in addition to $\varphi < 1$.

For the equation of state of hard anisotropic solids, the known virial coefficients of the respective geometry can be used in combination with an approximation of higher virial coefficients by the Carnahan-Starling series. With analytically known second-order and numerically determined third- to eighth-order virial coefficients using

$$\sum_{i=9}^{\infty}(i^2+i-2)\varphi^{i-1} = \frac{2\varphi^8(35\varphi^2-78\varphi+44)}{(1-\varphi)^3}, \tag{22}$$

we can express the real gas factor Z as

$$Z = 1 + \sum_{i=2}^{8}\tilde{B}_i(B_2^*\varphi)^{i-1} + \frac{2\varphi^8(35\varphi^2-78\varphi+44)}{(1-\varphi)^3}. \tag{23}$$

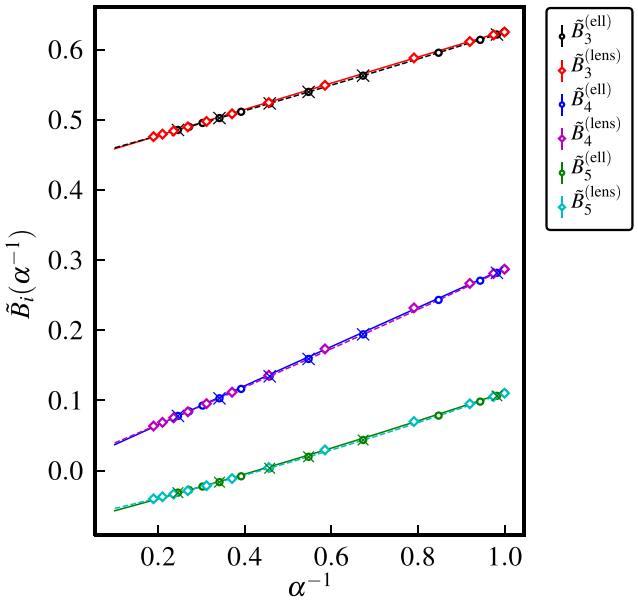

FIG. 8. Reduced virial coefficients $\tilde{B}_3$, $\tilde{B}_4$, and $\tilde{B}_5$ of hard lenses and hard ellipsoids of revolution as a function of the excluded volume's inverse excess part α^{-1}. The crosses represent data from [27]. The lines are least-squares fits of lens and ellipsoid data to parabolas [Eq. (16)].

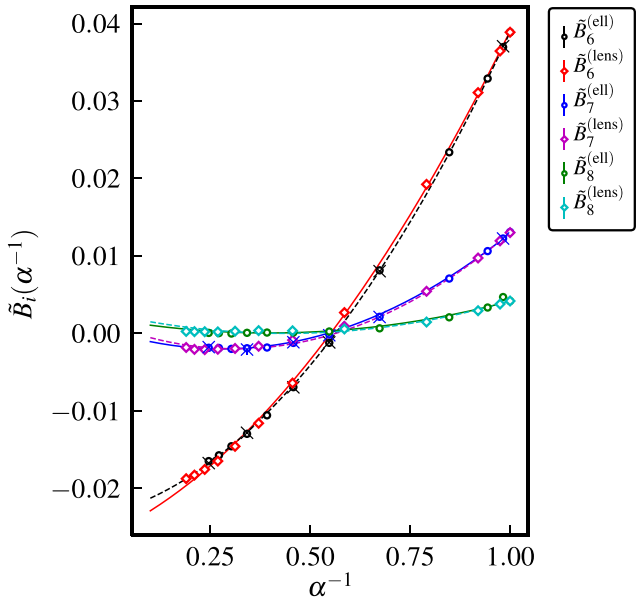

FIG. 9. Reduced virial coefficients $\tilde{B}_6$, $\tilde{B}_7$, and $\tilde{B}_8$ of hard lenses and hard ellipsoids of revolution as a function of the excluded volume's inverse excess part α^{-1}. The lines are least-squares fits of lens and ellipsoid data to parabolas [Eq. (16)]. The crosses represent data from [27].

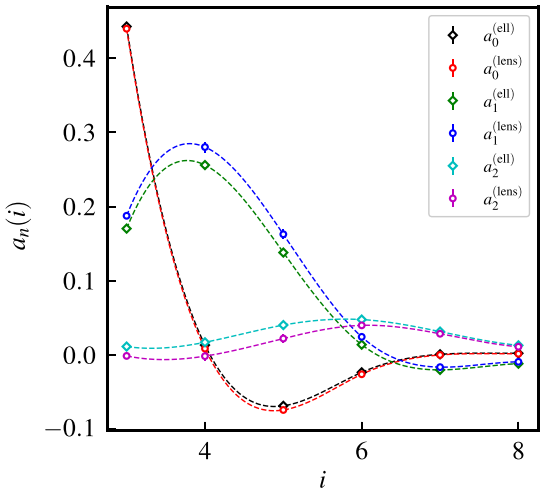

FIG. 10. Optimum parameters $a_{0,i}$, $a_{1,i}$, and $a_{2,i}$ of Eq. (16) describing the dependence of the reduced virial coefficients $\tilde{B}_i$ on the inverse excess part of the excluded volume α^{-1} for orders $i = 3$ to 8. The dotted lines are cubic splines as a guide to the eye.

Employing Eq. (16), we obtain

$$Z = 1 + \frac{2\varphi^8(35\varphi^2 - 78\varphi + 44)}{(1-\varphi)^3} + B_2^*\varphi + \sum_{i=3}^{8}(a_{0,i} + a_{1,i}\alpha^{-1} + a_{2,i}\alpha^{-2})(B_2^*\varphi)^{i-1} \qquad (24)$$

as an approximative interpolation for the real gas factor of hard, oblate ellipsoids of revolution and lenses. Since the slope of $\tilde{B}_i$ versus α^{-1} decreases systematically with increasing order of the virial coefficients and presumably approaches zero (Fig. 9), approximating orders $i \geqslant 9$ of so far unknown virial coefficients of anisotropic particles by those of hard spheres [Eq. (22)] is a suitable approach.

The Parsons approach [26,41] approximates high-order virial coefficients of anisotropic hard bodies by rescaling Carnahan-Starling virial coefficients by a factor of $B_2^*(\nu)/B_2^{*(\mathrm{HS})}$, where $B_2^{*(\mathrm{HS})} = 4$ denotes the reduced second virial coefficient of hard spheres. While negative virial coefficients of highly anisotropic particles cannot be approximated in an adequate way by this approach, our numerical data for eighth-order virial coefficients are reasonably described by this approach. Probably, rescaling the contribution of even higher virial coefficients given by Eq. (22) in this way could improve the real gas factor in Eq. (24).

The effect of increasing the order of the virial expansion on the real gas factor is exemplarily shown in Fig. 11 for ellipsoids and Fig. 12 for lenses, each with an aspect ratio of $\nu = 1/4$. By comparison, the influence of more negative sixth- and seventh-order virial coefficients of lenses becomes evident.

In the following, we investigate for selected aspect ratios the dependence of the real gas factor Z on the volume fraction. Here, we focus on the interval of confidence of the real gas factor given by Eq. (23) derived from uncertainties of virial coefficients from order 3 to 8 and the reliability of the interpolation approach [Eq. (24)].

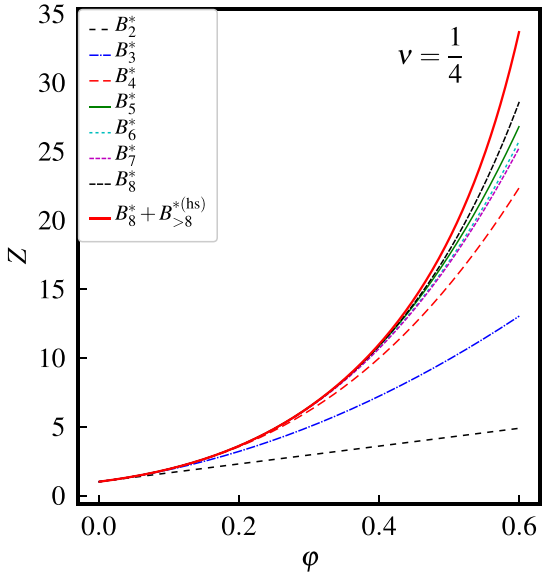

FIG. 11. Real gas factor Z of ellipsoids with aspect ratio $\nu = 1/4$ for different orders of the virial series. Indicated is the highest-order term contributing to Z. The thick solid line includes the contribution of higher-order virial coefficients approximated by the Carnahan-Starling series, Eq. (22).

For less anisotropic particles, Eq. (24) excellently describes real gas factors up to the maximum random packing fraction (Fig. 13), which can exceed that of hard spheres [42]. With increasing anisotropy, at least for small and moderate volume fractions, a reasonable approximation within the accuracy of available virial coefficients is possible (Figs. 14

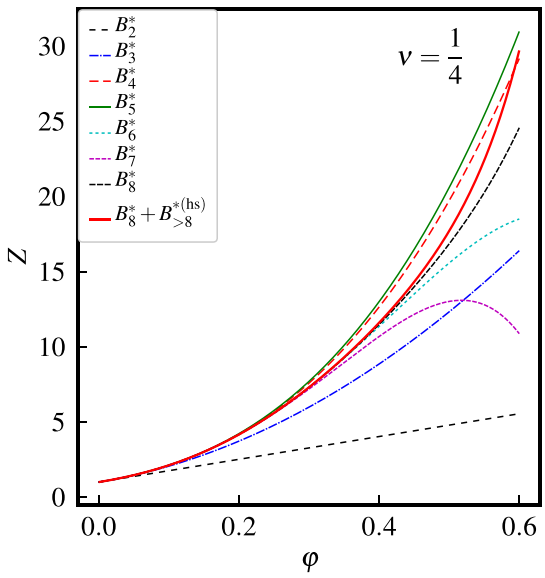

FIG. 12. Real gas factor Z of lenses with aspect ratio $\nu = 1/4$ for different orders of virial series. Again, the highest-order term contributing to Z is indicated, and for the thick solid line the contribution of higher-order virial coefficients approximated by the Carnahan-Starling series, Eq. (22), is included.

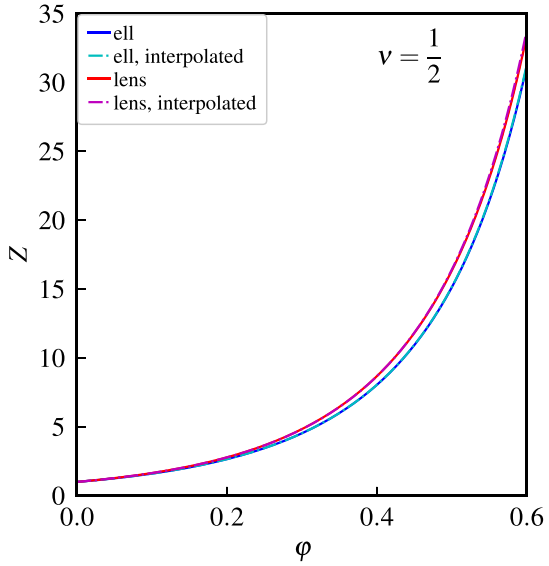

FIG. 13. Real gas factor Z for ellipsoids of revolution and lenses with aspect ratio $\nu = 1/2$ as a function of volume fraction φ. Displayed are real gas factors resulting from Eq. (23), where analytically known second virial coefficients B_2^* and numerically determined virial coefficients of order 3 to 8 are used. The contributions of higher-order virial coefficients are approximated by virial coefficients obtained from the Carnahan-Starling series, leading to Eq. (22). The real gas factors calculated by the interpolation [Eq. (24)], displayed as dashed lines, agree excellently with those obtained from virial coefficients calculated for aspect ratio $\nu = 1/2$. The uncertainties of the real gas factors are less than the width of the solid lines.

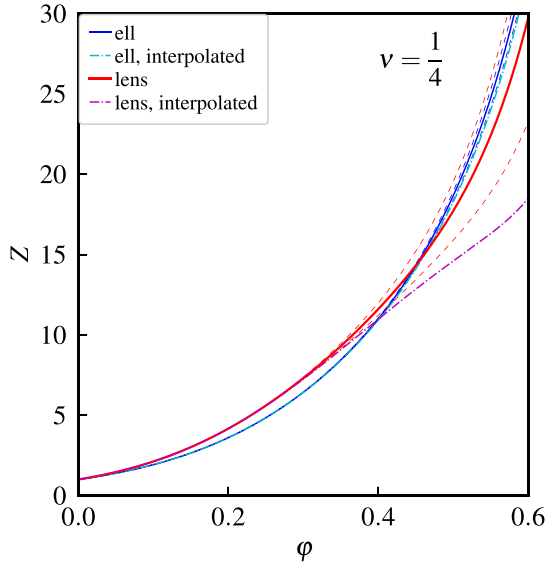

FIG. 14. Real gas factor Z for ellipsoids of revolution and lenses with aspect ratio $\nu = 1/4$ as a function of volume fraction φ. The real gas factors obtained from virial coefficients for aspect ratio $\nu = 1/4$ are represented as solid lines; those from interpolation [Eq. (24)] are represented as dashed-dotted lines. The uncertainties are indicated by thin dashed lines. While for ellipsoids the interpolation is nearly up to $\varphi = 0.6$ within the uncertainty of the real gas factor, the interpolation deviates in the case of lenses for $\varphi \gtrapprox 0.4$.

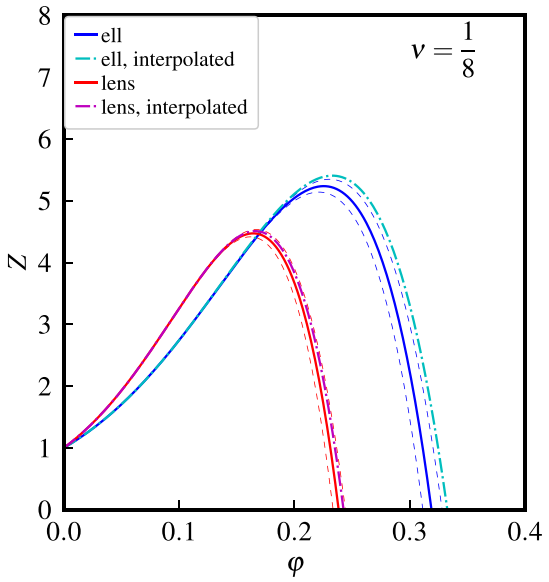

FIG. 15. Real gas factor Z for ellipsoids of revolution and lenses with aspect ratio $\nu = 1/8$ as a function of volume fraction φ. Possible reasons for the decrease of real gas factor Z with increasing volume fraction φ are the truncation of the virial series or an isotropic-nematic phase transition, which occurs for hard lenses at volume fractions significantly smaller than for hard ellipsoids of revolution. Again, the real gas factors resulting from virial coefficients for aspect ratio $\nu = 1/8$ are displayed as solid lines and the interpolation according to Eq. (24) is displayed as dashed-dotted lines.

and 15). For higher volume fractions, the uncertainty of the real gas factor Z, however, increases significantly.

For highly anisotropic shapes, a decreasing real gas factor with increasing volume fraction φ could either be related to an isotropic-nematic phase transition or insufficient approximation of higher-order virial coefficients by those of spheres. The critical volume fraction for this transition is in the case of lenses significantly smaller than in the case of hard ellipsoids: while the maximum real gas factor at an aspect ratio $\nu = 1/8$ is found at a volume fraction $\varphi \approx 0.23$ for hard ellipsoids, in the case of hard lenses the maximum real gas factor occurs at $\varphi \approx 0.17$.

VI. DISCUSSION

The numerical effort for the calculation of virial coefficients increases dramatically with the order i of the respective virial coefficient. One reason is the number $i(i-1)/2$ of pair interactions in an i cluster roughly quadratically increasing with order i. Much more severe is the superexponential increase of labeled graphs that need to be considered.

With an optimized algorithm based on bisection search of an ordered representation of Ree-Hoover graphs, where for hard bodies only a single graph contributes at a given configuration to the virial coefficients, the value of this single contributing graph can rapidly be determined. The CPU time needed to determine virial coefficients up to order 8 increases in first approximation logarithmically with the order of the virial coefficients.

Since rotational degrees of freedom dramatically increase the dimensionality of configuration space compared to spherically symmetric systems, a highly efficient numerical integration algorithm is required. Importance sampling algorithms such as Mayer sampling efficiently explore the configuration space in regions where integrands contribute significantly. Since with this method the configuration space is no longer explored with uniform sampling density, a known reference integral has to be sampled simultaneously.

The efficiency and accuracy of importance sampling increase when the reference system and system of interest are as similar as possible. The approach of Singh and Kofke [33] to use a known virial coefficient or at least one or more graphs contributing to a known virial coefficient requires the determination of pair interactions both in the system of interest and reference system. For anisotropic hard solids, the determination of orientation-dependent contact distances is numerically demanding. Hence, identifying overlaps and nonoverlaps both in the system of interest and reference system requires considerable computing resources.

The numerical effort can drastically be reduced using a known integral of the same system instead which depends on already determined overlaps and nonoverlaps. Here, trees as graphs are a suitable reference, whose integrals can be written as powers of the second virial coefficient, which is for convex bodies analytically known. However, this approach is not limited to convex bodies, since the second virial coefficients of concave objects are numerically accessible with high accuracy, too. The increase of virial coefficients' uncertainties related to not exactly known reference integrals is still acceptable. Statistical fluctuations of virial coefficients during Mayer-sampling Monte Carlo runs using the same system as a reference are considerably smaller than those using a geometry of similar shape.

Since in the the limit $\nu \to 1^-$ ellipsoids and lenses approach spheres, a comparison with highly accurate literature data of spheres can be used to validate our algorithm. The relative deviations $\Delta^{(\mathrm{ell})}$ and $\Delta^{(\mathrm{lens})}$ smaller than 10^{-3} even for the eighth virial coefficients indicate the reliability of this algorithm optimized for hard, anisotropic particles. Deviations of virial coefficients independently determined employing the contact algorithms for ellipsoids and lenses in the limit $\nu \to 1^-$ from literature data of hard spheres are significantly smaller than our error estimates. This indicates realistic confidence intervals.

Using this improved algorithm, virial coefficients of order 3 to 8 of differently shaped, oblate solids of revolution were obtained systematically with high accuracy for a large range of aspect ratios.

The accuracy of available virial coefficients of ellipsoids could be improved. Simultaneously, the thus obtained data validate the reliability of our optimized algorithm. In addition, hitherto unknown virial coefficients of hard lenses from order 3 to 8 are calculated.

Interestingly, normalizing higher virial coefficients $\tilde{B}_i(\nu) = B_i(\nu)/B_2(\nu)^{i-1}$ to powers of the second virial coefficients $B_2(\nu)$ leads in first approximation to a universal dependence on the inverse reduced excess part α^{-1} of their mutual excluded volume. As the ratio of mutual excluded volume to the particle volume V_P is the reduced second virial coefficient $B_2^*(\nu) = B_2(\nu)/V_\mathrm{P}$, the excess part of the excluded volume, $B_2^*(\nu) - 1$, is solely related to the second virial coefficient.

Reduced virial coefficients $\tilde{B}_i$ from order 3 to 5 show a nearly linear dependence on the inverse excess part of the excluded volume α^{-1}, while from order 6 to 8 a slight nonlinearity occurs, which, however, can be described reasonably by a second-order polynomial. This in first approximation universal behavior of reduced virial coefficients $\tilde{B}_i$ of lenses and ellipsoids of revolution suggests that the entire dependence of the virial series of hard solids on the particle geometry is essentially reflected by the second virial coefficient. With this approximation, the equation of state for such particles can be formulated in a closed expression.

However, the comparison of further geometric shapes including prolate solids of revolution such as ellipsoids, spherocylinders, or spindles is a pending task deciding if this behavior is universal for hard solids.

ACKNOWLEDGMENT

P.M. gratefully acknowledges financial support by the Universität Rostock within the Ph.D. scholarship program.

APPENDIX: ANALYTICAL SECOND VIRIAL COEFFICIENTS OF OBLATE, HARD ELLIPSOIDS OF REVOLUTION AND LENSES

The second virial coefficient of convex hard solids is analytically accessible from the geometric measures volume, surface, and mean radius of curvature by means of the Isihara-Hadwiger theorem [9,38,43,44]. The reduced second virial coefficients of convex hard bodies are

$$B_i^* = 1 + \frac{S_\mathrm{P}\tilde{R}_\mathrm{P}}{V_\mathrm{P}}, \tag{A1}$$

where S_P is the surface, $\tilde{R}_\mathrm{P}$ is the mean radius of curvature, and V_P is the volume of the particle. These geometric measures read for oblate ellipsoids of revolution as

$$S_\mathrm{P}^{(\mathrm{ell})} = \frac{2\pi r_\mathrm{eq}^2}{\sqrt{1-\nu^2}}\left[\nu^2 \ln\left(\frac{1+\sqrt{1-\nu^2}}{\nu}\right) + \sqrt{1-\nu^2}\right], \tag{A2a}$$

$$\tilde{R}_\mathrm{P}^{(\mathrm{ell})} = \frac{\nu r_\mathrm{eq}}{2} + \frac{r_\mathrm{eq}}{2\sqrt{1-\nu^2}} \arctan\left(\frac{\sqrt{1-\nu^2}}{\nu}\right), \tag{A2b}$$

$$V_\mathrm{P}^{(\mathrm{ell})} = \frac{4\pi}{3}\nu r_\mathrm{eq}^3, \tag{A2c}$$

and for lenses as

$$S_\mathrm{P}^{(\mathrm{lens})} = 2\pi r_\mathrm{eq}^2(1+\nu^2), \tag{A3a}$$

$$\tilde{R}_\mathrm{P}^{(\mathrm{lens})} = \nu r_\mathrm{eq} + \frac{r_\mathrm{eq}}{2} \arctan\left(\frac{1-\nu^2}{2\nu}\right), \tag{A3b}$$

$$V_\mathrm{P}^{(\mathrm{lens})} = \pi r_\mathrm{eq}^3\left(\nu + \frac{\nu^3}{3}\right), \tag{A3c}$$

where r_eq and ν denote the particles' equatorial radius and aspect ratio.

[1] L. Onsager, Ann. NY Acad. Sci. **51**, 627 (1949).
[2] D. Frenkel, B. M. Mulder, and J. P. McTague, Phys. Rev. Lett. **52**, 287 (1984).
[3] B. Mulder and D. Frenkel, Mol. Phys. **55**, 1193 (1985).
[4] G. Odriozola, J. Chem. Phys. **136**, 134505 (2012).
[5] G. Bautista-Carbajal, A. Moncho-Jordá, and G. Odriozola, J. Chem. Phys. **138**, 064501 (2013).
[6] J. Vieillard-Baron, Mol. Phys. **28**, 809 (1974).
[7] P. Bolhuis and D. Frenkel, J. Chem. Phys. **106**, 666 (1997).
[8] J. A. C. Veerman and D. Frenkel, Phys. Rev. A **41**, 3237 (1990).
[9] E. Herold, R. Hellmann, and J. Wagner, J. Chem. Phys. **147**, 204102 (2017).
[10] G. Cinacchi and S. Torquato, J. Chem. Phys. **143**, 224506 (2015).
[11] G. Cinacchi and S. Torquato, Soft Matter **14**, 8205 (2018).
[12] G. Cinacchi and S. Torquato, Phys. Rev. E **100**, 062902 (2019).
[13] J. D. van der Waals, Proc. K. Ned. Akad. Wet. **1**, 138 (1899).
[14] B. Jäger, Sitzungsber. Akad. Wiss. Wien, Math.-Naturwiss. Kl., Abt. 2A **105**, 15 (1896).
[15] L. Boltzmann, Sitzungsber. Akad. Wiss. Wien, Math.-Naturwiss. Kl., Abt. 2A **105**, 695 (1896).
[16] L. Boltzmann, Proc. K. Ned. Akad. Wet. **1**, 398 (1899).
[17] H. Kamerlingh Onnes, Proc. K. Ned. Akad. Wet. **4**, 125 (1902).
[18] M. N. Rosenbluth and A. W. Rosenbluth, J. Chem. Phys. **22**, 881 (1954).
[19] F. H. Ree and W. G. Hoover, J. Chem. Phys. **40**, 939 (1964).
[20] F. H. Ree and W. G. Hoover, J. Chem. Phys. **46**, 4181 (1967).
[21] P. A. Monson and M. Rigby, Mol. Phys. **35**, 1337 (1978).
[22] D. Frenkel, J. Phys. Chem. **91**, 4912 (1987).
[23] W. Cooney, S. Thompson, and K. Gubbins, Mol. Phys. **66**, 1269 (1989).
[24] M. Rigby, Mol. Phys. **66**, 1261 (1989).
[25] J. A. C. Veerman and D. Frenkel, Phys. Rev. A **45**, 5632 (1992).
[26] C. Vega, Mol. Phys. **92**, 651 (1997).
[27] X.-M. You, A. Y. Vlasov, and A. J. Masters, J. Chem. Phys. **123**, 034510 (2005).
[28] A. Y. Vlasov, X.-M. You, and A. J. Masters, Mol. Phys. **100**, 3313 (2002).
[29] The On-Line Encyclopedia of Integer Sequences, https://oeis.org, Sequence A013922, accessed in 2021.
[30] F. H. Ree and W. G. Hoover, J. Chem. Phys. **41**, 1635 (1964).
[31] C. Zhang and B. M. Pettitt, Mol. Phys. **112**, 1427 (2014).
[32] R. J. Wheatley, Phys. Rev. Lett. **110**, 200601 (2013).
[33] J. K. Singh and D. A. Kofke, Phys. Rev. Lett. **92**, 220601 (2004).
[34] J. W. Perram and M. Wertheim, J. Comp. Phys. **58**, 409 (1985).
[35] A. J. Schultz and D. A. Kofke, Phys. Rev. E **90**, 023301 (2014).
[36] S. Labík, J. Kolafa, and A. Malijevský, Phys. Rev. E **71**, 021105 (2005).
[37] T. Boublík, Mol. Phys. **27**, 1415 (1974).
[38] H. Hadwiger, Experientia **7**, 395 (1951).
[39] N. F. Carnahan and K. E. Starling, J. Chem. Phys. **51**, 635 (1969).
[40] Y. Song, E. A. Mason, and R. M. Stratt, J. Phys. Chem. **93**, 6916 (1989).
[41] J. D. Parsons, Phys. Rev. A **19**, 1225 (1979).
[42] A. Baule, R. Mari, L. Bo, L. Portal, and H. A. Makse, Nat. Commun. **4**, 2194 (2013).
[43] A. Isihara, J. Chem. Phys. **18**, 1446 (1950).
[44] A. Isihara and T. Hayashida, J. Phys. Soc. Jpn. **6**, 40 (1951).

5.2 Publication II: Reexamining equations of state of oblate hard ellipsoids of revolution: Numerical simulation utilizing a cluster Monte Carlo algorithm and comparison to virial theory

Philipp Marienhagen and Joachim Wagner,
Phys. Rev. E **105**, 014125 (2022).
DOI: 10.1103/PhysRevE.105.014125.

Contribution:
This work was conceptualised by P.M. and J.W., P.M. implemented all algorithms, performed calculations, and analysed the results. The draft was written by P.M. and revised by P.M. and J.W. The work was supervised by J.W.

Reexamining equations of state of oblate hard ellipsoids of revolution: Numerical simulation utilizing a cluster Monte Carlo algorithm and comparison to virial theory

Philipp Marienhagen and Joachim Wagner*
Institut für Chemie, Universität Rostock, 18059 Rostock, Germany

(Received 29 November 2021; accepted 5 January 2022; published 25 January 2022)

We provide highly accurate equation-of-state data determined by means of cluster Monte Carlo simulations for the isotropic phase of oblate hard ellipsoids of revolution. Both equation-of-state data and phase boundaries of the isotropic phase are obtained from relatively large ensembles with typically 1000 particles. The comparison of simulation data with a virial approach gives evidence for the importance of high-order so-far-unknown virial coefficients and therewith many-particle interactions in dense, isotropic systems of anisotropic particles. While a virial approach with a rescaled Carnahan-Starling correction for the unknown, higher-order virial coefficients reproduces the simulation data of moderately anisotropic particles with high accuracy, we suggest for highly anisotropic shapes a simple, heuristic equation of state as a suitable approach.

DOI: 10.1103/PhysRevE.105.014125

I. INTRODUCTION

Due to their relevance as model systems for dense condensed matter, hard-particle systems have attracted large scientific interest for several decades. In addition to hard-sphere systems, where numerous properties can be calculated analytically, with increasing computer performance a growing interest in anisometric hard-particle systems emerged. Using computer simulations considering realistic many-particle interactions, Onsagers theory on isotropic-nematic phase transitions [1] could be confirmed and extended. To obtain an analytical access to this phase transition, Onsager used infinitely thin needles as a model. With computer simulations, which are capable to handle different particle shapes, the investigation of the influence of the detailed particle geometry and its aspect ratio ν is possible. Herewith, tunable models for the self-organization and properties of liquid crystalline matter could be investigated.

First computer simulations of hard ellipsoids [2,3] identified an isotropic-nematic phase transition depending on the aspect ratio and provided first equation-of-state data for these systems. The identification of unusual dense packings of ellipsoids exceeding even close packings of spheres [4] initiated a reexamination of the hard ellipsoid system concerning both equation of state [5] and phase behavior for the identified structures. In addition to an isotropic and nematic phase, a plastic crystalline phase and the unusually dense monoclinic SM2 phase could be identified as two types of crystalline phases [6–9].

The theoretical investigation of hard-sphere systems simultaneously stimulated the development and refinement of simulation techniques. Starting from the seminal Metropolis-Hastings scheme [10,11] as a theoretical background of classical Monte Carlo (MC) simulations, improved methods such as biased MC simulations [12], event-chain Monte Carlo [13–15], and replica exchange Monte Carlo methods [16] have been developed.

Especially for the simulation of hard-body multiparticle systems in the isobaric and isothermal (N, p, T) ensemble, cluster MC as a variant of biased MC simulations is the method of choice to calculate accurate equation-of-state data as shown by Almarza [17] for the crystalline phase of hard-sphere systems. This method has been extended to anisotropic particles to investigate the phase behavior of hard rhombic platelets [18]. The availability of theoretical predictions for the phase behavior and equation of state has regularly lead to experimental verifications employing colloidal model systems with predominant hard-body interactions by means of scattering methods [19] or confocal microscopy [20].

The virial series is a complementary theoretical approach to equation-of-state data of the isotropic phase of hard multiparticle systems. While the second virial coefficients of convex hard bodies are analytically known [21–24], higher virial coefficients have to be calculated employing numerical methods [25,26]. With an optimized algorithm based on Mayer sampling [27], these quantities are accessible with improved accuracy [28]. In contrast to MC simulations of large ensembles, for the calculation of the virial coefficient of order i, a cluster integral over interactions between i particles is calculated. Since the maximum order of accessible virial coefficients is limited, the truncation of the virial series at order $i_{\max}$ ignores contributions of clusters with $N > i_{\max}$ particles to the equation of state.

The Carnahan-Starling relation $B_i^* = i^2 + i - 2$ as an approximation for the reduced virial coefficients of order i leads to a closed expression for hard spheres' equation of state in terms of their volume fraction $\varphi = \varrho V_{\mathrm{P}}$, where ϱ denotes the number density of particles and V_{P} the particle volume. Parsons suggested rescaling the hard-sphere virial coefficients by the ratio of the reduced, second virial coefficient of an anisotropic shape and a sphere as an approximation for the

*joachim.wagner@uni-rostock.de

equation of state of an ensemble of anisotropic particles [29]. Later, Vega [25] modified this approach considering all known virial coefficients and approximating only the unknown ones in the same manner. Alternatively, several heuristic correlations for the equation of state have been suggested [30–33].

Since cluster-MC simulations give access to precise equation-of-state data and implicitly take many-particle interactions of large systems into account, with these data, a systematic evaluation of proposed equations of state and corrections for the truncated virial series is possible.

II. THEORETICAL BACKGROUND

A. (N, p, T) Monte Carlo algorithm

Monte Carlo simulations in the isobaric-isothermal (N, p, T) ensemble are a useful approach to determine equation-of-state data of hard particles as already proposed by McDonald [34]. In this ensemble with fixed pressure p, Monte Carlo simulations compute the configuration integral of the studied system which is independent of the thermal energy $\beta^{-1} = k_B T$ since the potential energy $U(\mathbf{r}^N, V)$ can in the case of hard particles only be infinite in an overlapping configuration or zero otherwise. In the following, for better readability, only the potential energy's dependence on the center-of-mass coordinates $\mathbf{r}^N$ is explicitly written down, which can easily be extended to anisotropic systems by additionally introducing angular coordinates.

To simulate an (N, p, T) ensemble, fluctuations of the system's volume V and therewith the simulation box are necessary. Employing a transformation matrix $\mathbf{H}$ defined by $\mathbf{r}_i = \mathbf{H}.\mathbf{s}_i$, volume-independent, reduced center-of-mass coordinates $\mathbf{s}_i$ are elegantly obtained allowing particle moves decoupled from volume changes of the simulation box. The volume of the simulation box equals the parallelepipedal product $V = \|\mathbf{H}\|$ of the transformation matrix.

In the case of fluid phases, where a cubic simulation box can be used, the transformation matrix is simply related to matrix identity $\mathbf{I}$ via $\mathbf{H} = V^{\frac{1}{3}}\mathbf{I}$. For the simulation of solid phases, additionally shape fluctuations of the simulation box are required for which an upper triangular transformation matrix $\mathbf{H}$ is an obvious choice enabling decoupled shape and volume fluctuations.

B. Acceptance criteria for volume fluctuations

Starting from the configuration integral

$$Z_{N,p,T} = \int_V V^{N-1} \int_{\mathbf{s}_1} \cdots \int_{\mathbf{s}_N} \times \exp[-\beta pV - \beta U(\mathbf{s}^N, V)] d^N\mathbf{s}\, dV, \quad (1)$$

the normalized probability of a configuration $(\mathbf{s}^N, V)$ reads as

$$p_{N,p,T}(\mathbf{s}^N, V) = \frac{V^{N-1}}{Z_{N,p,T}} \exp[-\beta pV - \beta U(\mathbf{s}^N, V)] \quad (2)$$

with the reduced enthalpy as argument of the exponential. Herewith, the acceptance criterion $P_A(V'|V)$ for a volume change from V to V' in an (N, p, T) ensemble can be written as

$$P_A(V'|V) = \min\left[1, \left(\frac{V'}{V}\right)^{N-1} \frac{\exp[-\beta pV' - \beta U(\mathbf{s}^N, V')]}{\exp[-\beta pV - \beta U(\mathbf{s}^N, V)]}\right] \quad (3)$$

within the Metropolis-Hastings scheme [35].

C. Cluster MC algorithm

To improve the sampling efficiency, Almarza adopted a cluster algorithm for the (N, p, T) simulation of hard spheres [17]. In this approach, the biased formation of rigid pseudomolecules of especially close particles during volume fluctuations increases the accepted mean volume change $\langle|V' - V|\rangle$ and thus allows a better exploration of phase space. Before the actual volume change random bonds are generated between particles forming clusters containing all pairs of all linked particles. Instead of scaling the particles coordinates during a volume trial move, only the cluster's center of mass is rescaled, preserving the interparticle distances and orientations within the rigid cluster.

The arbitrary bond probability function $b(r_{ij})$ suggested by Almarza was generalized by Tasios [18] to anisotropic particles

$$b(\sigma_{ij}) = \begin{cases} 1 - \left(\frac{\sigma_{ij}}{\delta}\right)^2 & : \quad \sigma_{ij} < \delta \\ 0 & : \quad \sigma_{ij} \geqslant \delta \end{cases} \quad (4)$$

by considering the shortest surface distance σ_{ij} instead of the center-of-mass distance r_{ij}. Using the closest surface distance σ_{ij} weighted by the cutoff distance δ increases the probability of forming clusters at small surface distances while for distances $\sigma_{ij} \geqslant \delta$ bonds are not generated.

Since the probability of forming a specific cluster configuration depends via the surface distances σ_{ij} on the volume, an additional factor in the acceptance probability is required to fulfill the condition of detailed balance. Let $\omega_c(\chi_c|\mathbf{s}'^N, V')$ be the probability to form the cluster configuration χ_c at reduced center-of-mass configuration $\mathbf{s}'^N$ and volume V', and $\omega_c(\chi_c|\mathbf{s}^N, V)$ that with reduced center-of-mass configuration $\mathbf{s}^N$ at volume V, the acceptance probability for a volume change allowing cluster formation reads as

$$P_A(V'|V, \chi_c) = \min\left[1, \left(\frac{V'}{V}\right)^{\tilde{N}-1} \frac{\exp[-\beta pV' - \beta U(\chi_c, V')]}{\exp[-\beta pV - \beta U(\chi_c, V)]} \times \frac{\omega_c(\chi_c|\mathbf{s}'^N, V')}{\omega_c(\chi_c|\mathbf{s}^N, V)}\right] \quad (5)$$

under the constraint of detailed balance. Additionally, the apparent number of particles $\tilde{N} \leqslant N$ is reduced by cluster formation, where $\tilde{N}$ is the sum of remaining single particles and the number of present clusters.

The additional factor in the volume change proposal ratio allowing cluster formation can, according to Almarza [17], be written as

$$\frac{\omega_c(\chi_c|\mathbf{s}'^N, V')}{\omega_c(\chi_c|\mathbf{s}^N, V)} = \prod_{[ij]} \frac{1 - b(\sigma'_{ij})}{1 - b(\sigma_{ij})}, \quad (6)$$

where the product contains factors resulting from all particle combinations $[ij]$ where i and j belong to different clusters.

However, there is no need to check that i and j belong to different clusters: Since, within a cluster, interparticle distances and relative orientations are preserved during a volume change, the surface distances $\sigma'_{ij} = \sigma_{ij}$ remain unchanged, resulting in $[1 - b(\sigma'_{ij})]/[1 - b(\sigma_{ij})] = 1$. For large systems, the numerical stability can be improved by calculating the product by the summation of individual ratios' logarithms.

Using periodic boundary conditions, particles within a cluster may be linked via a chain of bonds to its periodic images. When this cluster percolation occurs, the simulation box cannot be rescaled, keeping the particle distances within the cluster constant. Hence cluster percolation has to be checked and volume change attempts leading to cluster percolation have to be rejected. If the amount of scale rejections becomes substantial, the sampling efficiency of cluster-MC simulations decreases.

D. Surface distance of ellipsoids

The check for overlaps of two ellipsoids can be done by the Perram-Wertheim algorithm [36]. This algorithm essentially scales two ellipsoids until they reach tangent contact. From the scaling factor at tangent contact, overlap and nonoverlap can be distinguished. We improved the performance of the original algorithm by replacing the bisection minimization by a Newton-Raphson minimization using analytic derivatives of the elliptic contact function.

There is no known algorithm to directly determine the closest surface distance $\sigma(\mathbf{A}, \mathbf{B})$ of two ellipsoids $\mathbf{A}$ and $\mathbf{B}$ with given shape, orientation, and center of mass which is needed to calculate the bond probability. Paramonov and Yaliraki [37] suggested a lower limit $\sigma_{\mathrm{ll}}(\mathbf{A}, \mathbf{B})$ and an upper limit $\sigma_{\mathrm{ul}}(\mathbf{A}, \mathbf{B})$ for the closest surface distance $\sigma(\mathbf{A}, \mathbf{B})$ fulfilling the inequality

$$0 < \sigma_{\mathrm{ll}}(\mathbf{A}, \mathbf{B}) \leqslant \sigma(\mathbf{A}, \mathbf{B}) \leqslant \sigma_{\mathrm{ul}}(\mathbf{A}, \mathbf{B}) \tag{7}$$

for nonoverlapping particles. The upper limit $\sigma_{\mathrm{ul}}(\mathbf{A}, \mathbf{B})$ can be directly determined in the Perram-Wertheim algorithm and is a reasonable approximation for large distances. In the limit $\sigma_{\mathrm{ul}}(\mathbf{A}, \mathbf{B}) \to \infty$, the approximation is independent of the mutual orientation of both ellipsoids. The lower limit $\sigma_{\mathrm{ll}}(\mathbf{A}, \mathbf{B})$ can be determined by calculating the projection of the upper limit to the normal vector of both rescaled ellipsoids at the common contact point. The latter approximation generally provides better results for small separations.

Therefore, the lower limit $\sigma_{\mathrm{ll}}(\mathbf{A}, \mathbf{B})$ is expected to be a better approximation in the case of small surface distances, when clusters are presumably formed. However, obvious differences between the results of cluster-MC simulations using both approximations for σ_{ij} are not observed within their uncertainties. We presume that the proposal ratio in Eq. (6) sufficiently compensates over- and underestimations of the surface distance. The data provided in this contribution are obtained using the lower limit $\sigma_{\mathrm{ll}}(\mathbf{A}, \mathbf{B})$ as an approximation for the closest surface distance.

E. Simulation details

An isotropic start configuration is prepared for each investigated pressure via an equilibration phase of 10^6 MC steps at a volume fraction of $\varphi = 0.05$ starting from a configuration with centers of mass placed at a cubic lattice and particle directors randomly aligned, where an MC step consists of N particle translation or rotation attempts and a volume change attempt.

The resulting isotropic configuration is compressed to the pressure of interest and after a second equilibration phase a production run with 5×10^7 steps is performed.

Since cluster percolation is an increasing obstacle for the simulation of highly anisotropic particles, the characteristic length δ which determines cluster formation is tuned to obtain approximately $N_{\mathrm{b}}/N \approx 1/4$, where N_{b} is the number of bonds created between N individual particles. Hereby the number of rejections due to cluster percolation is reduced to less than 1%.

Since isotropic-crystalline phase transitions can only be determined by the expansion of a crystalline phase, these phase boundaries are determined by expansion of a dense monoclinic SM2 crystal [38] containing between 972 and 1040 particles depending on their aspect ratio. For these expansion simulations, additionally shape fluctuations of the simulation box at constant volume are allowed, where at least 2×10^8 steps are performed.

III. RESULTS AND DISCUSSION

A. Validation of the cluster-MC algorithm with a system of hard spheres

As hard spheres are a thoroughly investigated model system, the cluster (N, p, T) algorithm is validated with hard spheres, i.e., ellipsoids with an aspect ratio $\nu = 1$. The deviations of our data from the highly accurate equation-of-state data of Kolafa *et al.* [39] are illustrated in Fig. 1 for five different system sizes from $N = 500$ to $N = 2916$.

A comparison of the different system sizes shows that the system-size dependence becomes more pronounced with increasing reduced pressure $\beta\, pr^3$. This is especially the case in the region of the phase transition, which is indicated by the dashed black line (as determined by Noya *et al.* [40]). The data beyond the phase transition result from a metastable phase and depend significantly on the system size. While this dependence is especially notable for $N = 500$ particles, it decreases for $N = 864$ particles and the deviations are within the determined uncertainties of the volume fraction φ compared to the equation of state of Kolafa *et al.* for larger systems. It is also visible that the determined uncertainties for a system of $N = 864$ hard spheres obtained in 5×10^7 steps employing the cluster algorithm displayed with blue error bars are considerably smaller than those obtained in 2.5×10^8 steps displayed with gray error bars employing a standard (N, p, T) approach. Although equation-of-state data for hard spheres can be determined via simpler methods, the comparison with the data shown in Fig. 1 is a proof of the cluster algorithm's reliability.

For anisotropic particles only few data are available resulting from relatively small ensembles. A comparison of available data from McBride and Lomba [5] with our cluster-MC data is displayed in the Supplemental Material (Sec. S-I) [41].

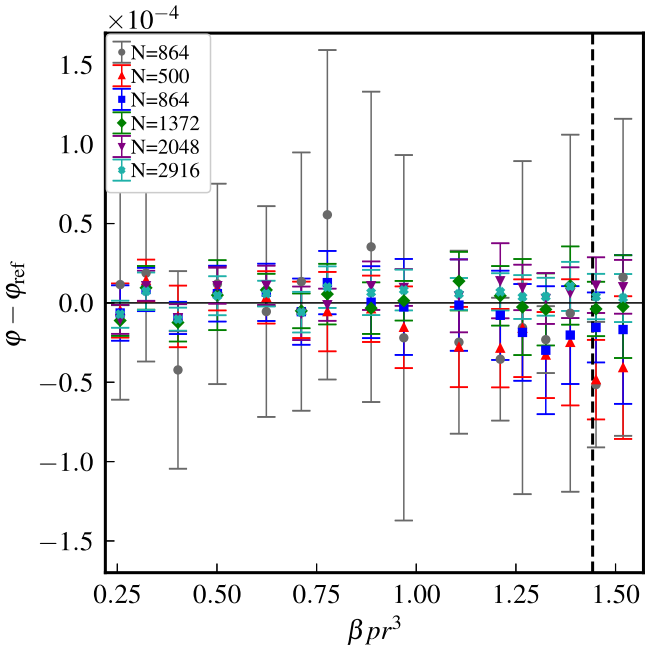

FIG. 1. Deviations of hard-sphere volume fraction φ from the reference data φ_{ref} from Kolafa *et al.* [39] in dependence on the reduced pressure βpr^3. The volume fractions are determined for five system sizes N obtained during 5×10^7 steps with the cluster (N, p, T) algorithm. For comparison, data obtained during 2.5×10^8 steps in a classical (N, p, T) MC simulation are displayed with dark gray circles. The liquid-solid phase transition of hard spheres determined by Noya *et al.* [40] is indicated by the dashed black line.

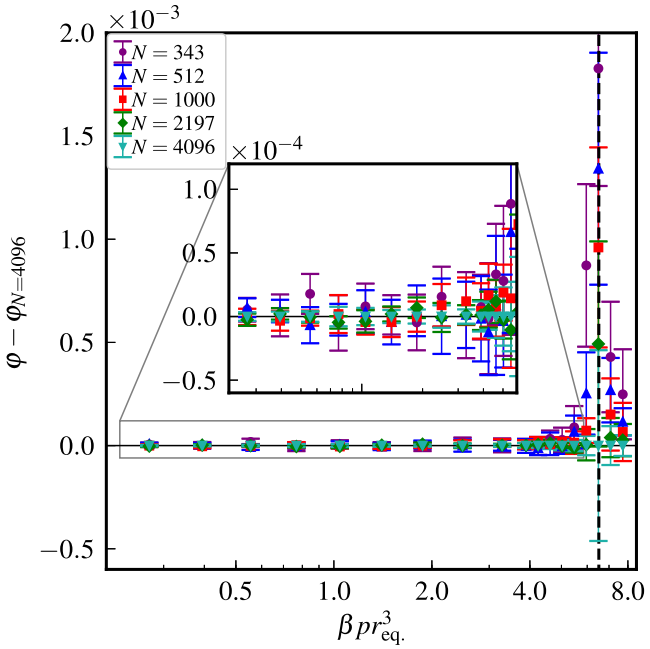

FIG. 2. Deviations of the volume fraction φ in dependence on the reduced pressure βpr^3_{eq} for aspect ratio $\nu = 1/3$ using different system sizes N. Here, the largest investigated system with $N = 4096$ particles is used as a reference. The estimated critical pressure for the isotropic-nematic phase transition is indicated by the dashed black line.

B. Influence of the system size for aspect ratio $\nu = 1/3$

The influence of the system size is exemplarily investigated for the intermediate aspect ratio $\nu = 1/3$. Data from five different system sizes from $N = 343$ to $N = 4096$ are analyzed in Fig. 2, where deviations of volume fractions are displayed in dependence on the reduced pressure. As a reference, data of the largest investigated system with $N = 4096$ particles are used.

For reduced pressures βpr^3_{eq} below the isotropic-nematic phase transition, a systematic dependence of the volume fraction φ on the system size cannot be observed. In the phase transition's vicinity, however, a significant system-size dependence emerges. Additionally, the uncertainties increase drastically in this region.

For the subsequent systematic investigation of equations of states in dependence on the aspect ratio ν, systems with $N = 1000$ particles are used. The deviations to a system of $N = 4096$ particles are in the range of the uncertainties at acceptable numerical effort. Equation-of-state data obtained for these systems with aspect ratios $1/10 \leqslant \nu \leqslant 1$ are compiled in Tables S-1, S-2, S-3, and S-4 in the Supplemental Material (Sec. S-II) [41].

C. Tracing the phase transitions

Since phase transitions are discontinuities in equations of state, the regions of stability need to be determined as a first step. For the equation of state in the isotropic phase of oblate ellipsoids of revolution, phase boundaries to nematic, plastic solid, and monoclinic phase limit their region of stability depending on the aspect ratio. The formation of these phases can be identified by means of characteristic observables.

1. Isotropic-nematic phase transition

The formation of nematic phases is identified by the nematic order parameters S_2 and S_4 defined as averages

$$S_2 = \left\langle \frac{1}{2}\left(3x_i^2 - 1\right) \right\rangle_{x_i}, \tag{8}$$

$$S_4 = \left\langle \frac{1}{8}\left(35x_i^4 - 30x_i^2 + 3\right) \right\rangle_{x_i}, \tag{9}$$

of the second- and fourth-order Legendre polynomials with $x_i = \hat{\mathbf{u}}_i.\hat{\mathbf{n}}$, where the unit vector $\hat{\mathbf{u}}_i$ denotes the orientation of particle i and the unit vector $\hat{\mathbf{n}}$ the nematic director. If the nematic director $\hat{\mathbf{n}}$ is *a priori* unknown, order parameters can be extracted from the largest positive eigenvalue of averaged dyadic vector products, known as the Saupe tensor in the case of S_2 [42,43]. However, if just the existence of a preferential direction is of interest, an orientational correlation can also be identified by using inner products of particle orientations $x_i = \hat{\mathbf{u}}_j.\hat{\mathbf{u}}_k$ instead. With the latter approach, averaging over scalar products of particle orientations $\hat{\mathbf{u}}_j$ and $\hat{\mathbf{u}}_k$ has to be limited according to periodic boundary conditions fulfilling the minimum image convention. In this work, we identify the isotropic-nematic phase transition by comparison of order parameters calculated via the latter approach.

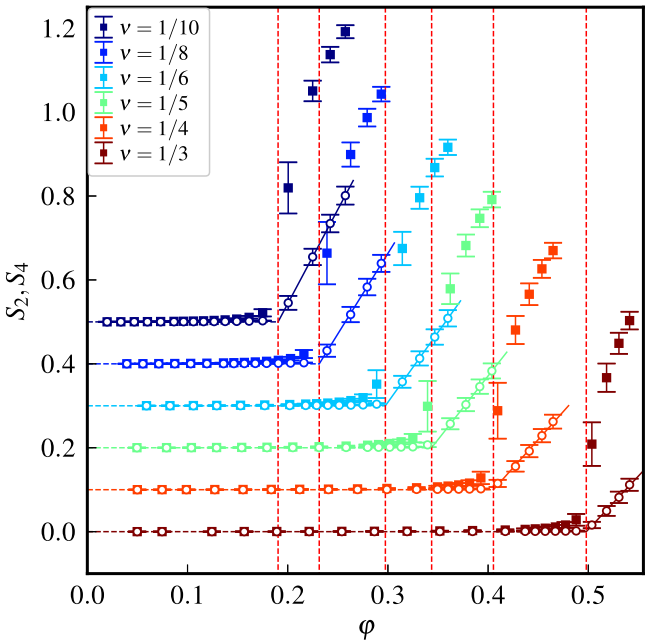

FIG. 3. Nematic order parameters S_2 (closed squares) and S_4 (open circles) in dependence on the volume fraction φ for six different aspect ratios ν separated by arbitrary offsets. The dashed red lines indicate the critical volume fractions φ_c which are roots of extrapolated, linear increasing S_4 beyond the transition to the nematic phase.

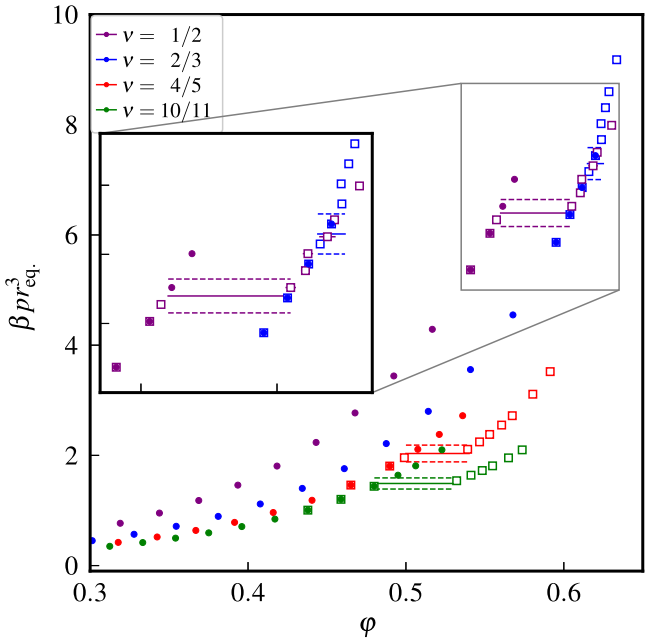

FIG. 4. Equation-of-state data for four different aspect ratios ν from compression (closed circles) and expansion (open squares) simulations. The coexistence pressures and their uncertainties are displayed as horizontal solid and dashed lines. While at aspect ratio $\nu = 1/2$ a transition from a SM2 phase to the isotropic phase is observed, for the less anisometric particles a transition from a plastic solid (PS) to the isotropic phase occurs.

Since the increase of S_4 with the volume fraction by transition to the nematic structure is much more pronounced than that of S_2, the critical volume fractions are determined by linear extrapolation of S_4 to its root. This approach is visualized in Fig. 3, where for a better display the data are separated by arbitrary offsets. The critical volume fractions φ_c as indicated by red dashed lines are compiled in Table I.

2. Isotropic-solid phase transitions

For aspect ratios $\nu \geqslant 1/2$, phase transitions from isotropic to either monoclinic SM2 phases or plastic solids (PS) occur. In contrast to the isotropic-nematic phase transition, which can be determined by compression of a disordered configuration, isotropic-solid phase transitions can only be determined by expansion of crystalline structures. Simulations of crystalline phases require deformation trials allowing nonorthogonal simulation boxes as enabled by appropriate transformation matrices **H** (Sec. II A). Due to the high sensitivity of the phase stability to the simulation box and the larger system-size dependence, data of crystalline phases exhibit larger uncertainties than those of isotropic and nematic phases. The uncertainties of coexistence pressures are estimated by pressure differences between consecutive, independent runs. The coexistence pressures at isotropic-crystalline phase transitions are displayed in Fig. 4. The respective data are compiled in Table I.

TABLE I. Phase boundaries of the isotropic phase.

ν	Phase transition	φ_c	$\beta p_c r_{\mathrm{eq}}^3$
1/10	I → N	0.190(2)	2.45(4)
1/8	I → N	0.231(2)	2.66(5)
1/6	I → N	0.297(2)	3.14(5)
1/5	I → N	0.344(2)	3.64(6)
1/4	I → N	0.405(2)	4.43(7)
1/3	I → N	0.498(2)	6.51(12)
1/2	I → SM2	0.560(5)	6.40(25)
2/3	I → PS	0.615(5)	7.30(29)
4/5	I → PS	0.500(10)	2.03(15)
10/11	I → PS	0.480(20)	1.49(10)

In contrast to Odrizola *et al.* [9], who identified the existence of a nematic phase in the limits $0.561 \leqslant \varphi \leqslant 0.565$ at aspect ratio $\nu = 1/2$ by means of replica exchange MC, we observed a direct transition from the monoclinic SM2 phase to the isotropic phase for these particles. To facilitate sufficient exchange probabilities between different replicas, the maximum size of a replica is rather limited. In contrast to Odriozala *et al.* our approach is to minimize the ensemble-size dependence using significantly larger systems instead of a higher density resolution. With exception of $\nu = 1/2$, our phase diagram reproduces that of Odriozola *et al.*

D. Equation-of-state data

Due to the absence of attractive interactions, fluidlike, hard-particle systems do not exhibit a critical point and thus are supercritical. Employing the virial series originally proposed by Kamerlingh Onnes [44] and later theoretically

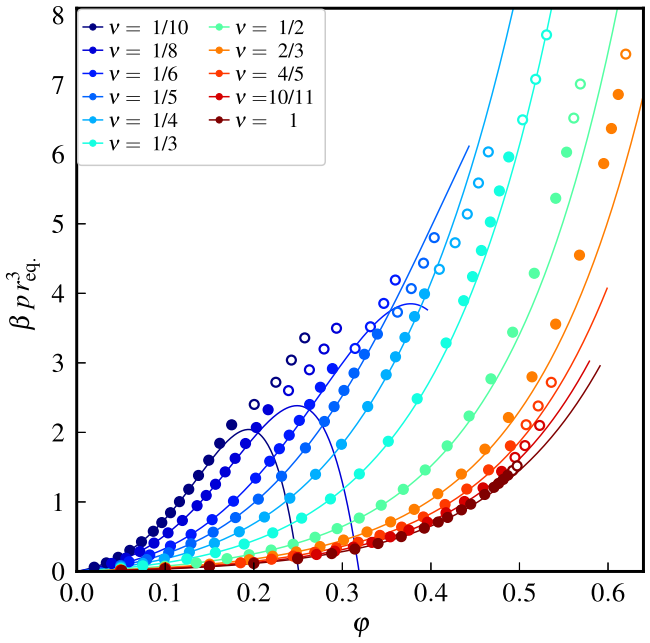

FIG. 5. Equation-of-state data for selected aspect ratios of oblate hard ellipsoids. The solid lines represent the equation of state using a virial series up to order eight. Cluster-MC data in the isotropic phase are represented by solid circles, while cluster-MC results beyond the phase boundary of the isotropic phase are displayed by open circles.

derived by Mayer [45], the real gas factor Z can be written exactly as

$$Z = \frac{p}{\varrho k_B T} = 1 + \sum_{i=2}^{\infty} B_i^* \, \varphi^{i-1} \tag{10}$$

if the reduced virial coefficients B_i^* are known up to infinite order i. In the virial series, the virial coefficient B_i^* of order i accounts for the contribution of i-particle interactions, i.e., clusters consisting of i particles to the real gas factor.

Depending on the particle shape, only a limited number of hard particles' virial coefficients are known. The truncation of the virial series after the highest available virial coefficient possibly leads to an inadequate description for the equation of state depending on the the volume fraction φ.

In Fig. 5, the reduced pressure $\beta p r_{\mathrm{eq.}}^3$ in dependence on the volume fraction φ resulting from cluster-MC simulations is compared to a virial approach using recently published, accurate virial coefficients up to order eight [28]. This comparison shows a severe discrepancy between simulation data and truncated virial series at high volume fractions φ. For highly anisotropic particles, the truncated virial approach even leads to unphysical, negative real gas factors.

Previously, different approaches to compensate the contributions of unknown, higher virial coefficients have been discussed. These corrections can be reevaluated quantitatively with the now available, accurate cluster-MC data.

1. Corrections for truncated virial series

Parsons [29] suggested a correction based only on the second virial coefficient of the respective geometry and the Carnahan-Starling equation of state for hard spheres [46]. As this approach leads to a simple analytical expression for the free energy, it is widely used in classical density functional theory [47]. When only few low-order virial coefficients of hard anisotropic particles were known, Nezbeda [30], Boublík [31], as well as Song and Mason [32] proposed corrections for the truncation of the virial series.

With access to the virial coefficients up to order five, Vega extended the Parsons approach by using the known virial coefficients and approximating the unknown ones by an identically rescaled Carnahan-Starling approach. Hence, a generalized Parsons approach reads as

$$Z = 1 + \sum_{i=2}^{i_{\max}} B_i^* \varphi^{i-1} + \frac{B_2^*}{B_2^{*,\,\mathrm{HS}}} \sum_{i=i_{\max}+1}^{\infty} B_i^{*,\,\mathrm{HS}} \varphi^{i-1}, \tag{11}$$

if virial coefficients up to order $i_{\max}$ are known. Hereby, essentially the Carnahan-Starling approximation for the missing virial coefficients of order $i > i_{\max}$ is rescaled by the ratio of second virial coefficients of the respective shape B_2^* and hard spheres $B_2^{*,\,\mathrm{HS}}$.

With $\varphi < 1$, for the infinite Carnahan-Starling series, the closed expression

$$\sum_{i=2}^{\infty} (i^2 + i - 2)\varphi^{i-1} = \frac{4\varphi - 2\varphi^2}{(1-\varphi)^3} \tag{12}$$

results. Herewith for any number $i_{\max}$ of known virial coefficients, a closed expression for Eq. (11) can be formulated. For $i_{\max} = 8$ this leads to

$$Z = 1 + \sum_{i=2}^{8} B_i^* \varphi^{i-1} + \frac{B_2^*}{4} \frac{2\varphi^8 (35\varphi^2 - 78\varphi + 44)}{(1-\varphi)^3}. \tag{13}$$

The comparison of Figs. 5 and 6 clearly shows that for moderately anisotropic particles with $\nu \geqslant 1/5$ the virial series with the correction according to Eq. (13) accurately describes the cluster-MC results within the phase boundaries of the isotropic phase. For intermediate aspect ratios, slight over- and underestimations at high pressures can be identified. For highly anisotropic particles with $\nu \leqslant 1/6$, however, significant deviations still occur leading as previously discussed even to unphysical, negative real gas factors. The drop of real gas factors is caused by negative virial coefficients of order $i \geqslant 5$ emerging already for moderately anisotropic particles.

Since the maximum volume fraction of the isotropic phase is comparatively small for highly anisotropic particles, higher-order virial coefficients can only contribute significantly if their moduli are extraordinarily large. As visible in Fig. 6, even rescaled higher-order virial coefficients of hard spheres cannot compensate the negative contribution of known virial coefficients: The rescaled Parsons correction based on hard spheres, adequately describing moderately anisotropic particles' equation of state, fails in the case of highly anisotropic particles.

Orientational correlations of limited range can occur in isotropic phases even if, in the thermodynamic limit, a long-range orientational correlation is absent. Whenever the orientational correlation lengths exceed the size of an i-cluster, they are not reflected in the corresponding virial

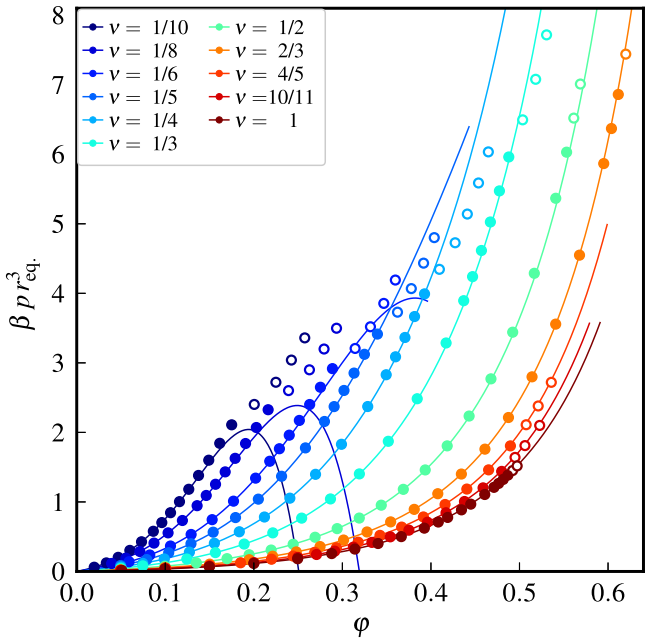

FIG. 6. Equation-of-state data for selected aspect ratios of oblate hard ellipsoids. The solid lines correspond to the virial series employing a rescaled Carnahan-Starling correction [Eq. (13)]. The equation-of-state points resulting from cluster-MC are displayed by circles, whereby closed circles are in the isotropic phase and open circles beyond the phase boundary of the isotropic phase.

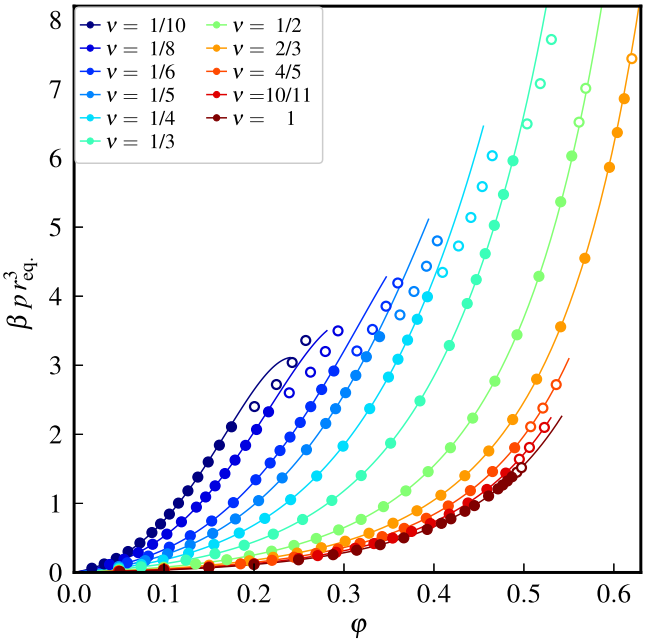

FIG. 7. Equation-of-state data for selected aspect ratios of oblate hard ellipsoids and fits using the generalized Carnahan-Starling relation [Eq. (14)]. The closed circles are equation-of-state points in the isotropic phase while open circles represent equation-of-state data beyond the phase boundary of the isotropic phase.

coefficient of order i. To adequately take the effect of orientational correlations into account, high-order up-to-now inaccessible virial coefficients are required.

Since orientational correlations do not exist for spheres and the Parsons correction only includes the second virial coefficient which is based on pair interactions, approaches based on the Parsons correction are not capable to describe the effect of increasing orientational correlation lengths emerging with progressively anisometric particles.

2. *Generalized Carnahan-Starling equation*

For hard spheres, numerous correlations for the compressibility factor using virial coefficients as well as equation-of-state data have been investigated [48]. Many of them are Padé expansions based on the Carnahan-Starling equation, where an increasing number of additional parameters improve their accordance with available data. For the exhaustively investigated hard-sphere system, Kolafa *et al.* [39] proposed a polynomial with as much as nine heuristic parameters as an accurate description of the real gas factor.

We investigate a modified Carnahan-Starling equation

$$Z = \frac{1 + \gamma_0\varphi + \gamma_1\varphi^2 - \gamma_2\varphi^3}{(1-\varphi)^3}, \tag{14}$$

where in addition to the analytically known second virial coefficient only two further parameters are needed. To approach the virial expansion in the low-density limit, the parameter γ_0 is chosen to be

$$\gamma_0 = B_2^* - 3, \tag{15}$$

which is for hard particles the excess part of the mutual excluded volume. The correlations proposed by Nezbeda [30] and Song and Mason [32] approach this low-density limit as well.

The remaining parameters γ_1 and γ_2 are obtained via least-squares fits from cluster-MC data within the boundaries of the isotropic phase (Sec. III C). The cluster-MC real gas factors and least-squares fits according to Eq. (14) are displayed in Fig. 7, and the optimum parameters γ_1 and γ_2 are compiled in Table II in dependence on the aspect ratio ν.

Despite the simplicity of this heuristical correction with only two unknown parameters, the real gas factor according

TABLE II. Parameters γ_1 and γ_2 and their uncertainties for a generalized Carnahan-Starling-type equation [Eq. (14)] for 11 different aspect ratios ν as well as density limits of the data considered.

ν	Limits	Coefficients	
		γ_1	γ_2
1/10	$0.020 < \varphi < 0.190$	61.66143(13)	333.7431(10)
1/8	$0.039 < \varphi < 0.231$	37.40249(11)	169.0247(8)
1/6	$0.059 < \varphi < 0.297$	19.00785(5)	68.07192(23)
1/5	$0.050 < \varphi < 0.344$	12.26132(8)	37.2321(3)
1/4	$0.050 < \varphi < 0.405$	7.12067(9)	17.5093(4)
1/3	$0.050 < \varphi < 0.498$	3.57926(7)	6.50072(18)
1/2	$0.050 < \varphi < 0.560$	1.593380(26)	1.88163(6)
2/3	$0.050 < \varphi < 0.615$	1.25381(12)	1.43668(24)
4/5	$0.049 < \varphi < 0.500$	1.11610(13)	1.1958(4)
10/11	$0.050 < \varphi < 0.480$	1.07955(15)	1.1336(4)
1	$0.051 < \varphi < 0.492$	1.07284(22)	1.1246(6)

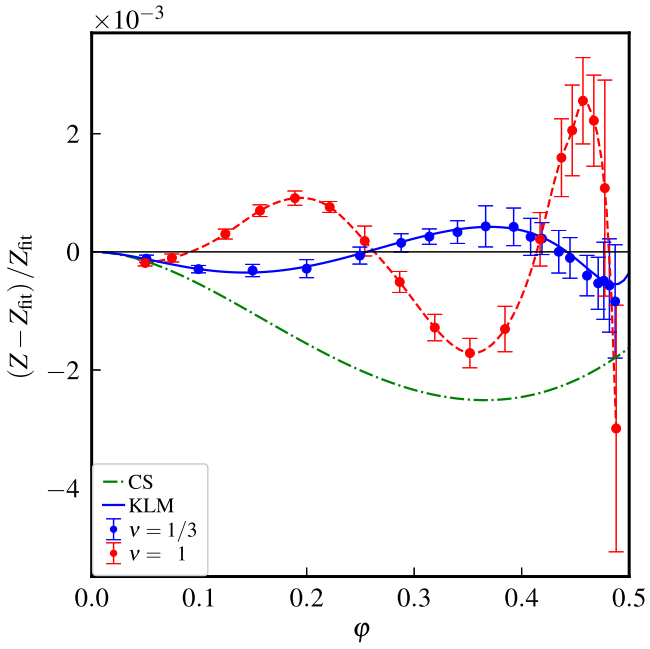

FIG. 8. Relative deviations of the modified Carnahan-Starling real gas factor Eq. (14) from simulation data exemplarily shown for aspect ratios $\nu = 1$ (hard spheres) and $\nu = 1/3$. The green line is the relative deviation from the Carnahan-Starling equation ($\gamma_1 = \gamma_2 = 1$) and the blue line the relative deviation from the Kolafa-Labík-Malijevský equation of state for hard spheres [39]. The dashed red line is a cubic spline as a guide to the eye.

to Eq. (14) is in good agreement to cluster-MC data. As expected, systematic relative deviations of less than 0.5% still exist exceeding the uncertainty of cluster-MC data as exemplarily shown in Fig. 8.

IV. SUMMARY AND OUTLOOK

In principle, equilibrium properties of hard-particle systems can be accessed via an alternative route using molecular dynamics instead [4]. Considering collisions of anisotropic particles, the equations of motion are numerically demanding. Therefore, Monte Carlo simulations requiring only the discrimination of overlap and nonoverlap configurations are a widely used approach in the case of anisotropic systems.

Despite the larger numerical effort of cluster-MC in comparison to classical MC, the significantly increased statistical accuracy as illustrated in Fig. 1 in total reduces the CPU time required to access precise data. The benefit of this technique increases with the complexity of overlap algorithms which are often the time-critical step for anisotropic shapes.

The probability of cluster formation depends in the case of hard particles on the closest surface-to-surface distance between two particles. For many geometries, a closed analytical expression for the minimum surface distance does not exist. In the case of ellipsoids, an upper and a lower limit for the minimum surface distance can be determined. Cluster formation probabilities based on both approximations lead to identical results for equation-of-state data: An approximation for this quantity is sufficient for cluster-MC simulations of ellipsoids and probably other shapes.

Using this method, the phase boundaries of the isotropic phase of oblate, hard ellipsoids of revolution are determined employing significantly larger ensembles than used before [5,9]. In addition, precise (N, p, T) equation-of-state data for the isotropic phase are obtained. This cluster-MC data are compared to the virial series considering recently published virial coefficients of oblate ellipsoids up to order eight.

For moderately anisotropic ellipsoids, the cluster-MC data excellently agree with the virial series up to moderate volume fractions (Fig. 5). The discrepancies in vicinity to the phase transition can be reduced significantly by a rescaled Carnahan-Starling correction [Eq. (13)] for the unknown virial coefficients of order $i > 8$ (Fig. 6).

For highly anisotropic particles with aspect ratio $\nu \leqslant 1/6$ even employing this correction, significant deviations from cluster-MC data are observed in the vicinity to the isotropic-nematic phase transition. At volume fractions beyond the isotropic-nematic phase transition, the virial series even predicts unphysical, negative pressures. A possible explanation are long-range orientational correlations in dense systems of highly anisotropic particles whose range is sufficiently covered only in large clusters reflected by inaccessible high orders of virial coefficients. Since orientational correlations do not exist in hard-sphere systems, any correction based on the Carnahan-Starling equation is not capable to correct these effects: Rescaling with the second virial coefficient of a highly anisotropic shape can only account for short-range orientational correlations in two-particle clusters.

Equation-of-state data of hard-particle systems are commonly described by heuristical correlations such as the Kolafa-Labík-Malijevský equation of state. For ellipsoids of revolution, different approaches have previously been published [25,30–32]. We propose a generalized Carnahan-Starling approach using the second virial coefficient and two additional parameters for each aspect ratio. Despite the simplicity of this approach, equation-of-state data are described surprisingly well within the phase boundaries of the isotropic phase.

Precise equation-of-state data resulting from cluster-MC simulations enable a quantitative analysis of truncation effects in virial approaches and commonly used corrections for the unknown, higher-order virial coefficients. Using oblate, hard ellipsoids of revolution, the capability of cluster-MC to access precise equation-of-state data of anisotropic hard particles is exemplarily demonstrated.

Systematic cluster-MC simulations of differently shaped hard particles can give insights into the importance of higher-order virial coefficients and many-particle interactions of hard particles in dependence on shape and aspect ratio for less dilute systems.

ACKNOWLEDGMENTS

P.M. gratefully acknowledges financial support by the Universität Rostock within the Ph.D. scholarship program.

[1] L. Onsager, Ann. N.Y. Acad. Sci. **51**, 627 (1949).
[2] D. Frenkel, B. M. Mulder, and J. P. McTague, Phys. Rev. Lett. **52**, 287 (1984).
[3] B. M. Mulder and D. Frenkel, Mol. Phys. **55**, 1193 (1985).
[4] A. Donev, I. Cisse, D. Sachs, E. A. Variano, F. H. Stillinger, R. Connelly, S. Torquato, and P. M. Chaikin, Science **303**, 990 (2004).
[5] C. McBride and E. Lomba, Fl. Phase Equilib. **255**, 37 (2007).
[6] P. Pfleiderer and T. Schilling, Phys. Rev. E **75**, 020402(R) (2007).
[7] M. Radu, P. Pfleiderer, and T. Schilling, J. Chem. Phys. **131**, 164513 (2009).
[8] G. Odriozola, J. Chem. Phys. **136**, 134505 (2012).
[9] G. Bautista-Carbajal, A. Moncho-Jordá, and G. Ordiozola, J. Chem. Phys. **138**, 064501 (2013).
[10] N. Metropolis, A. W. Rosenbluth, M. N. Rosenbluth, A. H. Teller, and E. Teller, J. Chem. Phys. **21**, 1087 (1953).
[11] M. N. Rosenbluth and A. W. Rosenbluth, J. Chem. Phys. **22**, 881 (1954).
[12] N. G. Almarza and E. Lomba, J. Chem. Phys. **127**, 084116 (2007).
[13] E. P. Bernard, W. Krauth, and D. B. Wilson, Phys. Rev. E **80**, 056704 (2009).
[14] M. Engel, J. A. Anderson, S. C. Glotzer, M. Isobe, E. P. Bernard, and W. Krauth, Phys. Rev. E **87**, 042134 (2013).
[15] M. Isobe and W. Krauth, J. Chem. Phys. **143**, 084509 (2015).
[16] G. Odriozola, J. Chem. Phys. **131**, 144107 (2009).
[17] N. G. Almarza, J. Chem. Phys. **130**, 184106 (2009).
[18] N. Tasios and M. Dijkstra, J. Chem. Phys. **146**, 144901 (2017).
[19] I. W. Hamley, J. Chem. Phys. **95**, 9376 (1991).
[20] J. Roller, A. Laganapan, J.-M. Meijer, M. Fuchs, and A. Zumbusch, Proc. Natl. Acad. Sci. USA **118**, e2018072118 (2021).
[21] A. Isihara, J. Chem. Phys. **18**, 1446 (1950).
[22] A. Isihara and T. Hayashida, J. Phys. Soc. Jpn. **6**, 40 (1951).
[23] H. Hadwiger, Experientia **7**, 395 (1951).
[24] E. Herold, R. Hellmann, and J. Wagner, J. Chem. Phys. **147**, 204102 (2017).
[25] C. Vega, Mol. Phys. **92**, 651 (1997).
[26] X.-M. You, A. Y. Vlasov, and A. J. Masters, J. Chem. Phys. **123**, 034510 (2005).
[27] J. K. Singh and D. A. Kofke, Phys. Rev. Lett. **92**, 220601 (2004).
[28] P. Marienhagen, R. Hellmann, and J. Wagner, Phys. Rev. E **104**, 015308 (2021).
[29] J. D. Parsons, Phys. Rev. A **19**, 1225 (1979).
[30] I. Nezbeda, Chem. Phys. Lett. **41**, 55 (1976).
[31] T. Boublík, Mol. Phys. **42**, 209 (1981).
[32] Y. Song and E. A. Mason, Phys. Rev. A **41**, 3121 (1990).
[33] M. J. Maeso and J. R. Solana, Mol. Phys. **79**, 1365 (1993).
[34] I. R. McDonald, Mol. Phys. **23**, 41 (1972).
[35] K.-K. Han and H. S. Son, J. Chem. Phys. **115**, 7793 (2001).
[36] J. W. Perram and M. S. Wertheim, J. Comput. Phys. **58**, 409 (1985).
[37] L. Paramonov and S. N. Yaliraki, J. Chem. Phys. **123**, 194111 (2005).
[38] A. Donev, F. H. Stillinger, P. M. Chaikin, and S. Torquato, Phys. Rev. Lett. **92**, 255506 (2004).
[39] J. Kolafa, S. Labík, and A. Malijevský, Phys. Chem. Chem. Phys. **6**, 2335 (2004).
[40] E. G. Noya, C. Vega, and E. de Miguel, J. Chem. Phys. **128**, 154507 (2008).
[41] See Supplemental Material at http://link.aps.org/supplemental/10.1103/PhysRevE.105.014125 for the comparison of available equation-of-state data for oblate hard ellipsoids of revolution with our cluster-MC data (Sec. S-I) and data for the reduced pressures and related real gas factors (Sec. S-II).
[42] R. Eppenga and D. Frenkel, Mol. Phys. **52**, 1303 (1984).
[43] E. Lomba, C. Martín, N. G. Almarza, and F. Lado, Phys. Rev. E **71**, 046132 (2005).
[44] H. Kamerlingh Onnes, Proc. K. Ned. Akad. Wet. **4**, 125 (1902).
[45] J. E. Mayer, J. Chem. Phys. **5**, 67 (1937).
[46] N. F. Carnahan and K. E. Starling, J. Chem. Phys. **51**, 635 (1969).
[47] J. Wu and Z. Li, Annu. Rev. Phys. Chem. **58**, 85 (2007).
[48] A. Mulero, C. Galán, and F. Cuadros, Phys. Chem. Chem. Phys. **3**, 4991 (2001).

Supplemental Material

Revisiting equations of state of oblate hard ellipsoids of revolution: Numerical simulation utilizing a cluster Monte Carlo algorithm and comparison to virial theory

Philipp Marienhagen and Joachim Wagner*
Institut für Chemie, Universität Rostock, Albert-Einstein-Straße 3a, 18059 Rostock, Germany

S-I. COMPARISON OF CLUSTER-MC DATA TO AVAILABLE LITERATURE DATA

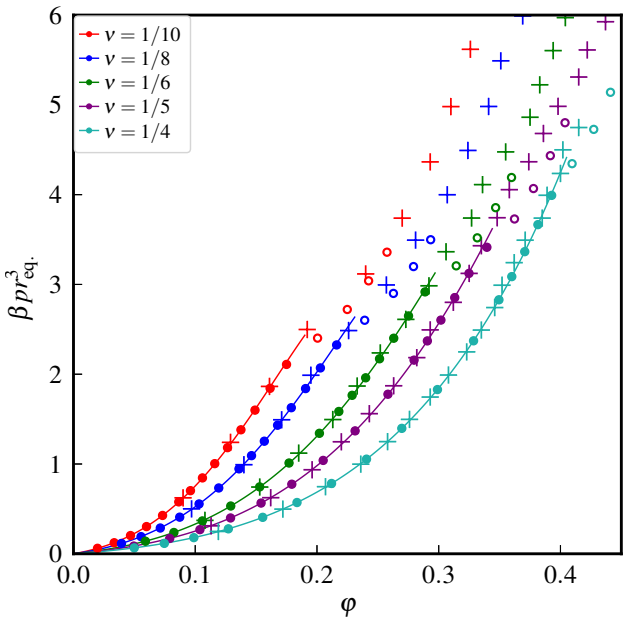

FIG. S-1. Cluster-MC data from this contribution (circles) in comparison to available literature data (crosses)[S1]. Closed circles represent the reduced pressure $\beta p r^3_{\mathrm{eq.}}$ in depence on the volume fraction φ for the isotropic phase. Open circles are reduced pressures of the nematic phase beyond the isotropic-nematic phase transition. The solid lines are results of the generalized Carnahan-Starling relation [Eq. (13)].

S-II. CLUSTER-MC DATA

Data for reduced pressure $\beta p r^3_{\mathrm{eq.}}$, volume fraction φ and related real gas factors Z are compiled in the subsequent tables for all investigated aspect ratios.

* joachim.wagner@uni-rostock.de

[S1] C. McBride and E. Lomba, Fl. Phase Equilib. **255**, 37 (2007).

TABLE S-1. Equation-of-state data for hard ellipsoids of revolution with aspect ratios $\nu = 1/10$, $\nu = 1/8$, and $\nu = 1/6$ determined by cluster-MC simulations.

$\nu = 1/10$			$\nu = 1/8$			$\nu = 1/6$		
$\beta p r^3_{\mathrm{eq.}}$	φ	Z	$\beta p r^3_{\mathrm{eq.}}$	φ	Z	$\beta p r^3_{\mathrm{eq.}}$	φ	Z
0.061	0.0197391(10)	1.29447(7)	0.115	0.0394144(20)	1.52772(8)	0.14	0.0590646(16)	1.65809(5)
0.123	0.0334406(13)	1.54070(6)	0.191	0.0554815(22)	1.80253(7)	0.237	0.082471(4)	2.01025(10)
0.203	0.0468417(16)	1.81532(7)	0.287	0.071299(5)	2.10764(13)	0.366	0.105863(5)	2.41849(11)
0.303	0.059986(4)	2.11585(14)	0.408	0.087256(5)	2.44830(13)	0.532	0.129166(4)	2.88117(9)
0.427	0.073164(5)	2.44467(14)	0.555	0.103150(4)	2.81724(11)	0.745	0.152923(6)	3.40791(13)
0.578	0.086484(8)	2.79949(25)	0.733	0.119320(6)	3.21654(16)	1.011	0.177046(10)	3.99458(22)
0.703	0.096084(6)	3.06473(18)	0.946	0.135931(6)	3.64394(17)	1.342	0.202000(14)	4.6474(4)
0.845	0.105933(5)	3.34128(13)	1.093	0.146235(7)	3.91351(19)	1.585	0.217964(16)	5.0869(4)
1.004	0.116035(8)	3.62438(25)	1.254	0.156745(15)	4.1889(4)	1.765	0.228876(12)	5.39447(27)
1.182	0.126523(5)	3.91325(16)	1.432	0.167643(13)	4.4725(4)	1.96	0.239989(21)	5.7131(5)
1.381	0.137542(9)	4.20579(27)	1.627	0.178908(15)	4.7617(4)	2.172	0.251387(25)	6.0440(6)
1.6	0.149089(14)	4.4953(5)	1.84	0.190630(15)	5.0539(4)	2.401	0.263049(19)	6.3850(5)
1.843	0.161494(15)	4.7803(5)	2.07	0.202818(23)	5.3440(6)	2.649	0.275195(13)	6.7336(3)
2.109	0.17499(4)	5.0485(11)	2.326	0.21615(5)	5.6345(13)	2.917	0.28877(14)	7.066(4)
2.402	0.20049(22)	5.018(6)	2.601	0.2392(5)	5.694(12)	3.207	0.31438(14)	7.136(3)
2.721	0.22490(8)	5.0679(17)	2.9	0.26279(6)	5.7782(12)	3.519	0.33169(11)	7.4216(23)
3.04	0.24242(5)	5.2529(10)	3.199	0.27930(5)	5.9972(11)	3.855	0.34675(5)	7.7771(10)
3.359	0.25751(4)	5.4640(8)	3.498	0.29338(4)	6.2430(8)	4.191	0.35980(6)	8.1481(13)

TABLE S-2. Equation-of-state data for hard ellipsoids of revolution with aspect ratios $\nu = 1/5$, $\nu = 1/4$, and $\nu = 1/3$ determined by cluster-MC simulations.

$\nu = 1/5$			$\nu = 1/4$			$\nu = 1/3$		
$\beta p r^3_{\mathrm{eq.}}$	φ	Z	$\beta p r^3_{\mathrm{eq.}}$	φ	Z	$\beta p r^3_{\mathrm{eq.}}$	φ	Z
0.086	0.0495383(20)	1.45437(6)	0.066	0.0498971(23)	1.38515(7)	0.047	0.0497722(19)	1.31718(6)
0.171	0.0790598(27)	1.81201(7)	0.116	0.0746028(24)	1.62829(5)	0.081	0.074594(4)	1.51465(7)
0.269	0.103858(4)	2.16985(9)	0.18	0.098863(5)	1.90663(10)	0.179	0.124317(6)	2.00843(9)
0.399	0.129009(4)	2.59103(8)	0.278	0.127222(8)	2.28830(14)	0.271	0.156577(7)	2.41420(10)
0.565	0.154078(9)	3.07205(17)	0.406	0.155432(9)	2.73535(15)	0.394	0.189081(8)	2.90658(13)
0.775	0.179322(8)	3.62065(16)	0.571	0.183593(7)	3.25693(12)	0.555	0.221420(6)	3.49630(10)
1.04	0.205090(11)	4.24823(22)	0.783	0.211965(9)	3.86835(16)	0.767	0.253998(15)	4.21209(26)
1.369	0.231321(8)	4.95800(16)	1.054	0.240690(8)	4.58575(15)	1.043	0.286538(10)	5.07732(18)
1.777	0.258288(15)	5.7637(4)	1.397	0.269676(12)	5.42478(24)	1.403	0.319178(12)	6.13137(23)
2.157	0.279740(16)	6.4597(4)	1.829	0.298966(10)	6.40649(20)	1.872	0.351842(12)	7.42149(25)
2.371	0.290671(16)	6.8336(4)	2.372	0.328613(16)	7.5589(4)	2.484	0.384486(17)	9.0116(4)
2.603	0.301800(19)	7.2256(5)	2.829	0.349463(24)	8.4774(6)	3.286	0.417116(19)	10.9886(5)
2.853	0.31316(3)	7.6323(8)	3.087	0.360015(23)	8.9793(6)	3.894	0.436996(22)	12.4294(7)
3.123	0.32487(5)	8.0535(11)	3.365	0.37067(4)	9.5066(8)	4.24	0.447012(25)	13.2306(8)
3.414	0.3396(7)	8.423(16)	3.666	0.38148(5)	10.0636(13)	4.616	0.457009(23)	14.0888(8)
3.729	0.36223(12)	8.6242(27)	3.992	0.39276(9)	10.6436(24)	5.026	0.467119(23)	15.0082(8)
4.068	0.37783(7)	9.0200(15)	4.345	0.4095(5)	11.110(14)	5.473	0.47733(6)	15.9934(19)
4.434	0.39168(5)	9.4838(13)	4.727	0.42733(9)	11.5838(25)	5.961	0.48789(7)	17.0422(21)
4.801	0.40375(8)	9.9617(19)	5.14	0.44109(10)	12.2030(27)	6.495	0.5036(5)	17.992(18)
			5.587	0.45370(6)	12.8954(17)	7.078	0.51824(18)	19.051(7)
			6.034	0.46482(7)	13.5941(21)	7.717	0.53057(15)	20.288(6)
						8.356	0.54121(11)	21.536(5)

TABLE S-3. Equation-of-state data for hard ellipsoids of revolution with aspect ratios $\nu = 1/2$, $\nu = 2/3$, and $\nu = 4/5$ determined by cluster-MC simulations.

$\nu = 1/2$			$\nu = 2/3$			$\nu = 4/5$		
$\beta p r^3_{\mathrm{eq.}}$	φ	Z	$\beta p r^3_{\mathrm{eq.}}$	φ	Z	$\beta p r^3_{\mathrm{eq.}}$	φ	Z
0.03	0.0498739(17)	1.25981(5)	0.022	0.0497010(25)	1.23672(7)	0.018	0.0491810(23)	1.22646(6)
0.076	0.099525(4)	1.59933(6)	0.055	0.099489(5)	1.54454(8)	0.046	0.100540(6)	1.53319(9)
0.123	0.135113(6)	1.90664(8)	0.105	0.150100(5)	1.95444(7)	0.086	0.150086(6)	1.92017(7)
0.184	0.169725(7)	2.27054(9)	0.169	0.194747(9)	2.42455(11)	0.125	0.185039(7)	2.26373(8)
0.24	0.194721(13)	2.58142(17)	0.219	0.221245(6)	2.76557(8)	0.176	0.219940(10)	2.68155(12)
0.308	0.219557(9)	2.93807(12)	0.281	0.247928(10)	3.16661(12)	0.221	0.244442(9)	3.02966(12)
0.391	0.244398(11)	3.35072(15)	0.358	0.274777(18)	3.64013(25)	0.275	0.268759(7)	3.42885(9)
0.492	0.269175(7)	3.82816(10)	0.452	0.301315(12)	4.19114(16)	0.341	0.293288(17)	3.89618(23)
0.616	0.294098(13)	4.38680(19)	0.568	0.327808(18)	4.84108(27)	0.421	0.317789(10)	4.43938(14)
0.768	0.319067(12)	5.04124(19)	0.713	0.354515(13)	5.61913(21)	0.519	0.342442(12)	5.07878(18)
0.953	0.343887(12)	5.80412(20)	0.893	0.381121(15)	6.54641(25)	0.638	0.366934(12)	5.82654(19)
1.181	0.368795(14)	6.70693(26)	1.118	0.407739(15)	7.66080(27)	0.784	0.391480(15)	6.71097(26)
1.46	0.393546(18)	7.7699(4)	1.401	0.434361(13)	9.01159(26)	0.963	0.415950(24)	7.7582(5)
1.806	0.418352(18)	9.0414(4)	1.759	0.460969(21)	10.6612(5)	1.185	0.440533(18)	9.0140(4)
2.235	0.443106(14)	10.5640(4)	2.214	0.487544(26)	12.6876(7)	1.461	0.465123(8)	10.52599(20)
2.77	0.467767(24)	12.4025(7)	2.799	0.514167(17)	15.2094(5)	1.806	0.489748(26)	12.3574(7)
3.441	0.492323(18)	14.6384(6)	3.557	0.54087(4)	18.3740(12)	2.11	0.50753(5)	13.9316(13)
4.288	0.516710(9)	17.38065(28)	4.549	0.56777(4)	22.3850(15)	2.38	0.521124(24)	15.3043(7)
5.367	0.540931(23)	20.7801(10)	5.866	0.59513(7)	27.539(4)	2.72	0.53593(4)	17.0076(12)
6.03	0.553197(27)	22.8295(11)	6.37	0.60385(13)	29.473(6)			
6.52	0.561317(18)	24.3275(8)	6.86	0.61156(19)	31.340(10)			
7.01	0.568762(27)	25.8135(12)	7.44	0.62001(20)	33.526(11)			

TABLE S-4. Equation-of-state data for hard ellipsoids of revolution with aspect ratios $\nu = 10/11$ and $\nu = 1$ determined by cluster-MC simulations.

$\nu = 10/11$			$\nu = 1$		
$\beta p r_{\mathrm{eq.}}^3$	φ	Z	$\beta p r_{\mathrm{eq.}}^3$	φ	Z
0.016	0.0496756(23)	1.22639(6)	0.015	0.0509774(23)	1.23254(7)
0.04	0.100001(5)	1.52304(7)	0.036	0.099374(5)	1.51746(7)
0.075	0.149822(6)	1.90606(8)	0.068	0.149711(9)	1.90258(11)
0.127	0.200183(11)	2.41563(14)	0.115	0.199968(13)	2.40894(16)
0.202	0.249634(11)	3.08106(14)	0.183	0.249500(12)	3.07234(15)
0.244	0.270806(11)	3.43072(15)	0.257	0.287902(12)	3.73919(16)
0.292	0.291349(7)	3.81612(9)	0.322	0.314118(10)	4.29390(13)
0.35	0.312422(14)	4.26559(18)	0.402	0.340297(14)	4.94830(20)
0.418	0.333314(15)	4.77502(21)	0.501	0.366491(23)	5.7262(4)
0.498	0.354095(14)	5.35504(21)	0.623	0.392519(19)	6.6484(4)
0.594	0.375102(13)	6.02961(21)	0.711	0.408306(18)	7.2941(4)
0.708	0.396068(19)	6.8064(4)	0.777	0.418880(15)	7.76998(28)
0.844	0.417021(20)	7.7061(4)	0.886	0.434489(19)	8.5417(4)
1.006	0.437866(16)	8.7480(4)	0.968	0.444962(17)	9.1126(4)
1.202	0.458864(15)	9.9741(4)	1.107	0.460768(16)	10.0636(4)
1.439	0.479875(21)	11.4179(5)	1.21	0.471173(20)	10.7571(5)
1.64	0.494956(26)	12.6163(7)	1.266	0.476428(29)	11.1308(7)
1.81	0.506172(25)	13.6155(7)	1.324	0.48163(4)	11.5150(8)
2.1	0.52279(6)	15.2948(15)	1.386	0.48694(4)	11.9226(10)
			1.451	0.49220(4)	12.3485(9)
			1.518	0.49737(5)	12.7845(12)

5.3 Publication III: Virial coefficients of hard hyperspherocylinders in $\mathbb{R}^4$: Influence of the aspect ratio

Markus Kulossa, Philipp Marienhagen, and Joachim Wagner,
Phys. Rev. E **105**, 064121 (2022).
DOI: 10.1103/PhysRevE.105.064121

Contribution:
This work was conceptualised by M.K., P.M., and J.W. The calculations were performed by M.K. Data was analysed by M.K. and P.M. The draft was written by M.K. and revised by all authors.

Virial coefficients of hard hyperspherocylinders in $\mathbb{R}^4$: Influence of the aspect ratio

Markus Kulossa, Philipp Marienhagen, and Joachim Wagner*
Institut für Chemie, Universität Rostock, 18051 Rostock, Germany

(Received 25 February 2022; accepted 23 May 2022; published 21 June 2022)

We provide second- to sixth-order virial coefficients of hard hyperspherocylinders in dependence on their aspect ratio ν. Virial coefficients of an anisotropic geometry in four dimensions are calculated employing an optimized Mayer-sampling algorithm. As the second virial coefficient of a hard particle is identical to its excluded hypervolume, the numerically obtained second virial coefficients can be compared to analytical relations for the excluded hypervolume based on geometric measures of the respective, convex geometry in dependence on its aspect ratio ν.

DOI: 10.1103/PhysRevE.105.064121

I. INTRODUCTION

Hard particles have been investigated thoroughly as a model for many-particle systems for more than a century. These studies have significantly contributed to the understanding of self-organization in condensed matter [1]. The virial series introduced by Kamerlingh Onnes [2],

$$p = \varrho k_\mathrm{B} T\left(1 + B_2\varrho + B_3\varrho^2 + \dots\right), \tag{1}$$

where p denotes the pressure, $k_\mathrm{B}T$ the thermal energy, and ϱ the particle number density, is the first attempt to describe thermodynamic properties of imperfect gases. The coefficients B_i in the MacLaurin expansion in number density accounting for the nonideal behavior are the virial coefficients. Introducing the volume fraction $\eta = \varrho V_\mathrm{P}$ as the product of number density ϱ and particle volume V_P, with

$$p = \frac{\eta}{V_\mathrm{P}} k_\mathrm{B} T\left(1 + B_2^*\eta + B_3^*\eta^2 + \dots\right), \tag{2}$$

an expansion in terms of the volume fraction η results, where $B_i^* = B_i/V_\mathrm{P}^{i-1}$ are reduced virial coefficients.

The first attempts to calculate virial coefficients use hard spheres as a model system with its geometric constraint of impenetrability [3–6]. The seminal work of Onsager with the analytically treatable model of infinitely thin rods predicted the formation of liquid-crystalline structures beyond a critical volume fraction [7]. Based on the theoretical foundation by means of statistical mechanics [8], with emerging computer performance, virial coefficients of order $5 \leqslant i \leqslant 12$ of hard spheres have been computed [9–15]. These methods have been extended to virial coefficients of anisometric hard bodies with different topology and aspect ratio [16–24].

Virial coefficients of hard discs as two-dimensional analogs of hard spheres have been theoretically [25,26] and numerically [27] calculated. For orders $i > 5$, in most cases, these virial coefficients were calculated together with those of hard spheres [10–12,28]. With these data, first insights into the dimensionality's influence to the nonideal behavior of gases and supercritical fluids with impacts on the maximum packing fraction have been possible [29].

The extension of the hard-sphere model system to Euclidean spaces with dimensionality $D > 3$, already published by Ree and Hoover [30], does not only provide useful physical insights [31], but also has implications to information theory [32]. Virial coefficients of hard spheres in higher dimensions interestingly become negative for even orders i in dimensions $D \geqslant 5$ [33]. For hard hyperspheres, selected virial coefficients up to order $i = 64$ and up to dimension $D = 100$ are known [28]. Virial coefficients of anisometric, hard objects in dimensions $D > 3$, however, are so far unknown.

The aim of this contribution is the calculation of uniaxial, hard hyperspherocylinders' virial coefficients for dimension $D = 4$ in dependence on their aspect ratio ν. Since the second virial coefficient of hard, convex objects equals the mutual excluded volume, its relation to geometric measures is analyzed in dependence on the aspect ratio ν. Herewith, expressions for a four-dimensional analog of the Isihara-Hadwiger relation [34–36] can be tested.

II. THEORETICAL BACKGROUND

Using the Ree-Hoover reformulation, the virial coefficient of order i can be written as

$$B_i = -\frac{i-1}{i!} \sum_{G \in \mathcal{R}_i^\mathrm{L}} c_G S_G, \tag{3}$$

where $\mathcal{R}_i^\mathrm{L}$ is the set of labeled Ree-Hoover graphs G with i vertices and weighting factors c_G, called Ree-Hoover star contents, depending on the graph's topology. S_G is the configuration integral over interactions represented by the labeled graph G. Since in the case of hard-body interaction a single Ree-Hoover diagram contributes to the integrand, the calculation based on the Mayer-sampling method [37] can be done employing an optimized algorithm with a bisection search in an ordered list containing all labeled diagrams with their star contents [23]. Mayer sampling as an importance sampling

*joachim.wagner@uni-rostock.de

technique requires the simultaneous calculation of a known reference integral. For the calculation of the second virial coefficients the analytically known second virial coefficient of hard hyperspheres is used as a reference for small aspect ratios $\nu \leqslant 5$. To increase the accuracy for aspect ratios $\nu \geqslant 6$, as a reference, the virial coefficient of hard hyperspherocylinders with aspect ratio $\nu = 5$ obtained with hard hyperspheres as a reference is used. To minimize the total uncertainties for $\nu \geqslant 6$, this reference value is extensively sampled to reduce the uncertainty of this numerically obtained reference integral. For virial coefficients with order $i \geqslant 3$, however, integrals of highly branched spanning trees containing i vertices, each with the value $(-2B_2)^{i-1}$, are the more efficient choice as an intrinsic reference integral [23].

A. Geometric measures of hyperspherocylinders in $\mathbb{R}^4$

A hyperspherocylinder is the union of hyperspheres with radius r_{eq} the centers of which are located at $\mathbf{r} = \mathbf{c} + \lambda\hat{\mathbf{u}}$, where $\mathbf{c} = (c_{\mathrm{w}}, c_{\mathrm{x}}, c_{\mathrm{y}}, c_{\mathrm{z}})^{\mathrm{T}}$ is the hyperspherocylinder's center of mass and $\hat{\mathbf{u}} = (u_{\mathrm{w}}, u_{\mathrm{x}}, u_{\mathrm{y}}, u_{\mathrm{z}})^{\mathrm{T}}$ its direction indicated by a Cartesian unit vector. The parameter $-(\nu-1)r_{\mathrm{eq}} \leqslant \lambda \leqslant (\nu-1)r_{\mathrm{eq}}$ defines the length of the hypercylinder barrel and is related to the hyperspherocylinder's equatorial radius r_{eq} and its aspect ratio $\nu \geqslant 1$. The hypervolume V of a hyperspherocylinder with equatorial radius r_{eq} and aspect ratio ν reads as

$$V = \frac{16(\nu-1)+3\pi}{6}\pi r_{\mathrm{eq}}^4, \tag{4}$$

and its hypersurface S can be written as

$$S = 2\pi[4(\nu-1)+\pi]r_{\mathrm{eq}}^3. \tag{5}$$

Its mean radius of curvature $\tilde{R}$ is accessible as the hypersurface integral of its mean curvature κ [38,39]. Since the latter quantity is $\kappa = 1/(3r_{\mathrm{eq}}^2)$ in the hypercylindrical part with length $2(\nu-1)r_{\mathrm{eq}}$, $1/r_{\mathrm{eq}}^2$ in both hemihyperspheres, and the curvature is continuous at the entire hypersurface, a hyperspherocylinder's mean radius of curvature $\tilde{R}$ reads as

$$\tilde{R} = \left[\frac{4(\nu-1)}{3\pi}+1\right]r_{\mathrm{eq}}. \tag{6}$$

B. Overlap criteria for hyperspherocylinders

Let $\mathbf{c}_1$ and $\mathbf{c}_2$ be two hyperspherocylinders' centers of mass, $\hat{\mathbf{u}}_1$ and $\hat{\mathbf{u}}_2$ unit vectors describing their orientation, r_{eq} their equatorial radius, and ν their aspect ratio. The overlap problem of hard hyperspherocylinders in $\mathbb{R}^4$ can be solved by determination of the minimum distance between the two lines $\mathbf{r}_1(\lambda) = \mathbf{c}_1 + \lambda\hat{\mathbf{u}}_1$ and $\mathbf{r}_2(\mu) = \mathbf{c}_2 + \mu\hat{\mathbf{u}}_2$ under the constraints $|\lambda| \leqslant (\nu-1)r_{\mathrm{eq}}$ and $|\mu| \leqslant (\nu-1)r_{\mathrm{eq}}$ in analogy to the overlap problem in $\mathbb{R}^3$ [40]. If the minimum distance is $|\mathbf{r}_1(\lambda_{\min}) - \mathbf{r}_2(\mu_{\min})| \leqslant 2r_{\mathrm{eq}}$, both hyperspherocylinders overlap, otherwise not. This overlap criterion can easily be extended to arbitrary dimensions D.

C. Simulation details

The calculation of the ith virial coefficient of an uniaxial solid of revolution in $\mathbb{R}^4$ requires an integration over a $7(i-1)$-dimensional configuration space which can be performed efficiently using a Mayer-sampling algorithm [37] extended to the four-dimensional space. In the case of hard-body systems, the originally proposed acceptance criterion has to be adapted by using a weighted sum of the integrands of both the system of interest and the reference system [23]. The algorithm is based on random translation and rotation attempts of randomly selected particles.

Let $\mathbf{\Omega} = (\vartheta, \chi, \varphi)$ be the angular coordinates of a random unit vector in $\mathbb{R}^4$ with the probability densities $p(\vartheta) = 2\sin^2\vartheta/\pi$, $p(\chi) = \sin\chi/2$, and $p(\varphi) = 1/(2\pi)$ in $0 \leqslant \vartheta \leqslant \pi$, $0 \leqslant \chi \leqslant \pi$, and $0 \leqslant \varphi \leqslant 2\pi$. With the abbreviations $a = \cos\vartheta$, $b = \sin\vartheta\cos\chi$, $c = \sin\vartheta\sin\chi\sin\varphi$, and $d = \sin\vartheta\sin\chi\cos\varphi$, a randomly oriented unit vector $\hat{\mathbf{u}} = (-d, -c, -b, a)^{\mathrm{T}}$ is generated. A random translation of a particle is achieved by choosing its center-of-mass position $\mathbf{c}_{N+1}$ at step $N+1$ relative to its previous position $\mathbf{c}_N$:

$$\mathbf{c}_{N+1} = \mathbf{c}_N + \Delta_{\mathrm{trans}}\,\xi\,\hat{\mathbf{u}}, \tag{7}$$

where $0 \leqslant \xi \leqslant 1$ is a uniformly distributed random number. The maximum length of displacement Δ_{trans} is tuned to obtain an acceptance ratio of $p_{\mathrm{acc}} \approx 1/2$.

Using again random angular coordinates $\mathbf{\Omega}$, a left isoclinic rotation matrix in $\mathbb{R}^4$ can be written as

$$\mathbf{R}(\mathbf{\Omega}) = \begin{pmatrix} a & -b & c & -d \\ b & a & -d & -c \\ -c & d & a & -b \\ d & c & b & a \end{pmatrix} \tag{8}$$

based on the Hamilton quaternion [41]. Additionally employing a rotation matrix

$$\mathbf{\Psi}(\psi) = \mathbf{R}(\psi, 0, 0) = \begin{pmatrix} \cos\psi & -\sin\psi & 0 & 0 \\ \sin\psi & \cos\psi & 0 & 0 \\ 0 & 0 & \cos\psi & -\sin\psi \\ 0 & 0 & \sin\psi & \cos\psi \end{pmatrix}, \tag{9}$$

a randomly rotated unit vector $\hat{\mathbf{u}}_{N+1}$ can be obtained from the orientation of a given particle $\hat{\mathbf{u}}_N$ at step N by

$$\hat{\mathbf{u}}_{N+1} = \mathbf{R}(\mathbf{\Omega}) \cdot \mathbf{\Psi}(\psi) \cdot \mathbf{R}^{\mathrm{T}}(\mathbf{\Omega}) \cdot \hat{\mathbf{u}}_N. \tag{10}$$

Choosing ψ with $-\Delta_{\mathrm{rot}} \leqslant \psi \leqslant \Delta_{\mathrm{rot}}$ as a random number with probability density $p(\psi) = 1/(2\Delta_{\mathrm{rot}})$ allows an exploration of the rotational configuration space with uniform density at the unit hypersphere's hypersurface as shown in the Appendix complemented by a detailed description of the rotation. The maximum rotation Δ_{rot} is again chosen to obtain an acceptance probability of $p_{\mathrm{acc}} \approx 1/2$.

The calculation of virial coefficients with known overlaps and nonoverlaps is independent of the systems' dimensionality and thus identical to the strategy in $\mathbb{R}^2$ and $\mathbb{R}^3$ as described in [23]: After translation and rotation of a selected particle $i(i-1)/2$ Mayer f functions f_{jk} are calculated based on overlaps and nonoverlaps between particles j and k of the obtained configuration, where, in the case of an overlap between particles j and k, $f_{jk} = -1$ is obtained and otherwise $f_{jk} = 0$ results. Defining additionally $e_{jk} = f_{jk} + 1$, the contribution of the generated configuration to the virial coefficient [Eq. (3)] is a product of f and e functions of the single contributing graph G weighted by its star content c_G [10].

TABLE I. Reduced virial coefficient B_i^* of hard, four-dimensional hyperspherocylinders with the aspect ratio ν.

ν	B_2^*	B_3^*	B_4^*	B_5^*	B_6^*
1		32.4061 (19)	77.743 (9)	146.23 (6)	253.2 (8)
	8	32.405759 . . .[a]	77.745183 . . .[a]	146.2451 (5)[a]	253.388 (6)[a]
2	9.6026 (4)	42.7361 (20)	96.325 (14)	174.58 (16)	340 (4)
3	11.9340 (6)	57.9720 (29)	108.70 (4)	270.5 (5)	444 (19)
4	14.3853 (7)	74.454 (9)	104.28 (5)	564.3 (13)	−850 (40)
5	16.87831 (21)	91.606 (11)	81.18 (7)	1213.2 (22)	−7000 (130)
6	19.3904 (11)	109.188 (21)	39.09 (14)	2363 (7)	−23500 (400)
7	21.9132 (13)	127.076 (25)	−21.31 (16)	4161 (12)	−57500 (600)
8	24.4416 (16)	145.19 (4)	−99.59 (24)	6723 (27)	−119000 (1100)
9	26.9744 (11)	163.52 (5)	−194.71 (24)	10180 (40)	−215600 (1900)
10	29.5108 (17)	182.00 (9)	−306.7 (6)	14581 (30)	−360000 (4000)

[a]Value from [28].

For the calculation of virial coefficients of order 2–6 at least 16 independent runs, each with 5×10^{10} Monte Carlo steps, are used. The data provided are averages with confidence intervals given by standard errors.

III. RESULTS AND DISCUSSION

The calculated virial coefficients of hard hyperspherocylinders with aspect ratios $1 \leqslant \nu \leqslant 10$ from order 2–6 are compiled in Table I. The literature values for hard hyperspheres' virial coefficients are in the limit $\nu \to 1^+$ reproduced within their uncertainties for the orders $3 \leqslant i \leqslant 6$. Since the scope of this paper is an aspect-ratio dependent approach covering orientation averages of anisotropic particles, the numerical effort is drastically increased. The larger uncertainties compared to hard hyperspheres' virial coefficients in [28] are therefore not a principal limitation of the used algorithm, but a consequence of the significantly enlarged computational demands.

A. Second virial coefficient and excluded hypervolume

Using the geometric measures of hypersurface S, mean radius of curvature $\tilde{R}$, and particle hypervolume V_P, the relation

$$B_2^* = 1 + \frac{7}{4}\frac{S\tilde{R}}{V_\mathrm{P}} \tag{11}$$

was proposed for convex geometries as the excluded hypervolume per particle in $\mathbb{R}^4$ [38], which is in the case of hard-body interaction identical to the second virial coefficient. While this relation is valid for a hypersphere in the limit $\nu \to 1^+$, for larger aspect ratios severe discrepancies to second virial coefficients calculated by means of Mayer sampling arise (Fig. 1). However, the relation

$$B_2^* = 2\frac{S\tilde{R}}{V_\mathrm{P}} = \frac{8}{\pi}\frac{[4(\nu-1)+3\pi][4(\nu-1)+\pi]}{16(\nu-1)+3\pi} \tag{12}$$

describes the reduced second virial coefficients for $1 \leqslant \nu \leqslant 10$ with high accuracy.

Recently, the same authors corrected their conjecture (11) using mixed volumes and quermassintegrals [42]. For a convex set K, the excluded hypervolume per particle v_ex and thus the second virial coefficient can in the four-dimensional space be written as

$$B_2 = v_\mathrm{ex} = \frac{1}{2\kappa_4}\sum_{i=0}^{4}\binom{4}{i}W_i(\mathrm{K})W_{4-i}(\mathrm{K}), \tag{13}$$

where $\kappa_4 = \pi^2/2$ is the hypervolume of the unit hypersphere in $\mathbb{R}^4$ and $W_i(\mathrm{K})$ are quermassintegrals of K. With the latter quantities, B_2 can be written as

$$B_2 = \frac{2}{\pi^2}\left[W_0(\mathrm{K})W_4(\mathrm{K}) + 4W_1(\mathrm{K})W_3(\mathrm{K}) + 3W_2^2(\mathrm{K})\right]. \tag{14}$$

$W_0(\mathrm{K}) = V_\mathrm{P}^{(\mathrm{D})}(\mathrm{K})$ is the D-dimensional hypervolume of a convex shape, $W_1(\mathrm{K}) = S^{(\mathrm{D}-1)}(\mathrm{K})/D$ its $(D-1)$-dimensional hypersurface, $W_{D-1}(\mathrm{K}) = \kappa_D\tilde{R}$ its mean radius of curvature $\tilde{R}$ multiplied by the hypervolume κ_D of a D-dimensional unit

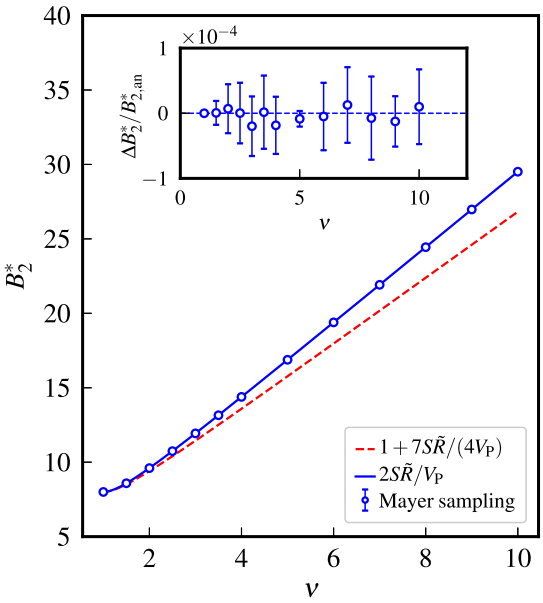

FIG. 1. Reduced second virial coefficients $B_2^* = B_2/V_\mathrm{P}$ for hard, four-dimensional hyperspherocylinders in dependence on the aspect ratio ν. The dashed red line represents relation Eq. (11), while the blue solid line represents Eq. (12). The inset displays the relative deviations $\Delta B_2^* = B_2^* - B_{2,\mathrm{an}}^*$ between numerically calculated, reduced second virial coefficients B_2^* and analytically calculated $B_{2,\mathrm{an}}^*$ employing Eq. (12).

hypersphere, and finally $W_D(\mathrm{K}) = \kappa_D$ the hypervolume of the D-dimensional unit hypersphere. Using these quantities, B_2 of a convex shape in $\mathbb{R}^4$ can be expressed as

$$B_2 = V_\mathrm{P}^{(4)}(\mathrm{K}) + S^{(3)}(\mathrm{K})\tilde{R}(\mathrm{K}) + \frac{6}{\pi^2}W_2^2(\mathrm{K}) \tag{15}$$

with the missing quermassintegral

$$W_2 = \frac{\pi^2}{2}r_\mathrm{eq}^2 + \frac{4\pi}{3}(\nu - 1)r_\mathrm{eq}^2 \tag{16}$$

of a hyperspherocylinder in $\mathbb{R}^4$ [43,44]. As easily can be seen, this leads to $V_\mathrm{P} + 6W_2^2/\pi^2 = S\tilde{R}$ and results in the analytical expression $B_2 = 2S\tilde{R}$ and therewith $B_2^* = 2S\tilde{R}/V_\mathrm{P}$. The relation $V_\mathrm{P} + 6W_2^2/\pi^2 = S\tilde{R}$ is to our knowledge unique for hyperspherocylinders in $\mathbb{R}^4$.

In the limit of infinitely long hyperspherocylinders, Eq. (12) leads to

$$\lim_{\nu\to\infty}\frac{B_2^*(\nu)}{\nu} = \frac{8}{\pi} \tag{17}$$

indicating an excluded hypervolume proportional to the aspect ratio ν.

In the two-dimensional Euclidean space with the figure's area A_F, the circumference S, and the mean radius of curvature $\tilde{R} = S/(2\pi)$, the reduced second virial coefficient can be written as $B_2^* = 1 + S\tilde{R}/(2A_\mathrm{F}) = 1 + S^2/(4\pi A_\mathrm{F})$ [45]. In the three-dimensional Euclidean space, the relation $B_2^* = 1 + S\tilde{R}/V_\mathrm{P}$ is obtained with the surface S, the mean radius of curvature $\tilde{R}$, and the particle volume V_P [34–36].

Despite that the hypervolume in Eq. (12) is not an additive contribution to the excluded hypervolume, the formulation based on quermassintegrals [Eq. (15)] shows that the hypervolume in fact contributes to the mutual excluded hypervolume. In analogy to the excluded volume in the two- and three-dimensional space, also in four- and higher-dimensional Euclidean spaces, the D-dimensional hypervolumes are additive contributions to the mutual excluded hypervolume.

B. Higher-order virial coefficients

The excellent agreement of our numerical results for the second virial coefficients with the analytical result [Eq. (12)] proves the correctness of the Mayer-sampling algorithm and the overlap criterion in $\mathbb{R}^4$. The third- to sixth-order virial coefficients in Table I are calculated using this analytical result as an exact reference integral. Noticeably, the higher-order virial coefficients exhibit alternating signs between even and odd orders at large aspect ratios: The even-order virial coefficients B_4^* and B_6^* are negative and strongly decrease with increasing aspect ratio ν, while the odd-order virial coefficients B_3^* and B_5^* are positive and notably increase with the aspect ratio ν. This behavior is also known for hyperspheres in dimensions $D \geqslant 8$ for third- and higher-order virial coefficients [28].

For convex figures in two dimensions and for oblate geometries in three dimensions, a nearly linear dependence of reduced virial coefficients $\tilde{B}_i = B_i/B_2^{i-1}$ on the inverse excess part of the excluded volume α appears especially for lower-order virial coefficients [23,46]. Employing Eq. (12), in four dimensions $\alpha = (B_2 - V_\mathrm{P})/(7V_\mathrm{P}) = (2S\tilde{R}/V_\mathrm{P} - 1)/7$ results,

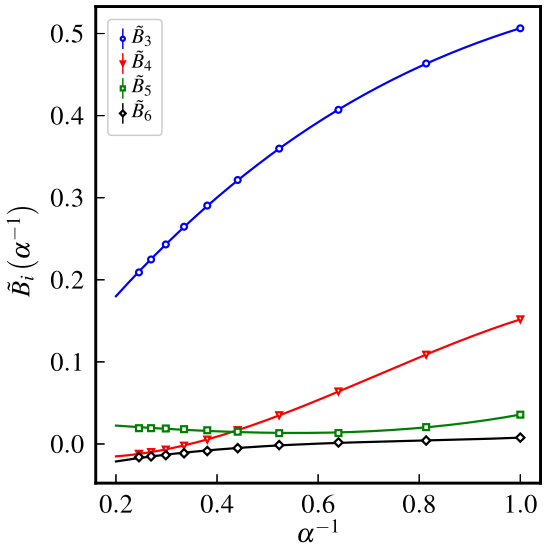

FIG. 2. Reduced virial coefficients $\tilde{B}_i = B_i/B_2^{i-1}$ in dependence on the inverse of the rescaled, excess part $\alpha = (2S\tilde{R}/V_\mathrm{P} - 1)/7$ of the excluded hypervolume. The solid lines are least-squares fits employing a third-order polynomial as a heuristic approach.

where the scaling factor $1/7$ guarantees $\alpha(\nu \to 1^+) = 1$ in the limit of a hypersphere.

In the case of four-dimensional hyperspherocylinders, consistent with results for three-dimensional spherocylinders [47], already for the third-order reduced virial coefficient $\tilde{B}_3$, a significant nonlinearity is observed (Fig. 2). However, the reduced virial coefficients $\tilde{B}_i$ of order 3–6 can excellently be described using a third-order polynomial in dependence on the aspect ratio ν and therewith reliably be interpolated.

IV. OUTLOOK

With the described approach, for the first time virial coefficients of four-dimensional, anisotropic objects are calculated. Using hard hyperspherocylinders exemplarily as a convex shape with tunable aspect ratio ν in $\mathbb{R}^4$, the impact of anisometry to the geometric measures of hypervolume, hypersurface, mean radius of curvature, and the quermassintegral W_2 can be analyzed and related to the second virial coefficient.

Our numerical results for B_2 agree with the analytical result employing mixed volumes and quermassintegrals [42]. A remaining task is the calculation of virial coefficients with order $i > 6$ for four-dimensional hyperspherocylinders and virial coefficients of differently shaped, hard anisotropic objects in $\mathbb{R}^4$.

ACKNOWLEDGMENTS

P.M. gratefully acknowledges financial support by the Universität Rostock within the Ph.D. scholarship program.

APPENDIX: EXPLORATION OF THE ROTATIONAL CONFIGURATION SPACE

Let $\mathbf{\Omega}_N = (\vartheta_N, \chi_N, \varphi_N)$ be generalized angular coordinates describing the orientation of an uniaxial solid of revolution in

$\mathbb{R}^4$ at step N. The orientation alternatively can be written as

$$\hat{\mathbf{u}}_N = \begin{pmatrix} \sin\vartheta_N \sin\chi_N \cos\varphi_N \\ \sin\vartheta_N \sin\chi_N \sin\varphi_N \\ \sin\vartheta_N \cos\chi_N \\ \cos\vartheta_N \end{pmatrix} \tag{A1}$$

using the Cartesian unit vector $\hat{\mathbf{u}}_N$. A random rotation in $\mathbb{R}^4$ can be achieved as follows.

(i) Generate a randomly oriented unit vector $\hat{\mathbf{u}}_\mathrm{r}$. Let $0 \leqslant \vartheta_\mathrm{r} \leqslant \pi$ be a random number with probability density $p(\vartheta_\mathrm{r}) = 2\sin^2\vartheta_\mathrm{r}/\pi$, $0 \leqslant \chi_\mathrm{r} \leqslant \pi$ a random number with probability density $p(\chi_\mathrm{r}) = \sin\chi_\mathrm{r}/2$, and $0 \leqslant \varphi_\mathrm{r} \leqslant 2\pi$ a random number with probability density $p(\varphi) = 1/(2\pi)$.

Using the definitions

$$d = \sin\vartheta_\mathrm{r} \sin\chi_\mathrm{r} \cos\varphi_\mathrm{r}, \tag{A2a}$$

$$c = \sin\vartheta_\mathrm{r} \sin\chi_\mathrm{r} \sin\varphi_\mathrm{r}, \tag{A2b}$$

$$b = \sin\vartheta_\mathrm{r} \cos\chi_\mathrm{r}, \tag{A2c}$$

$$a = \cos\vartheta_\mathrm{r}, \tag{A2d}$$

a left isoclinic rotation matrix in $\mathbb{R}^4$ [41] can be written as

$$\mathbf{R}(\mathbf{\Omega}_\mathrm{r}) = \begin{pmatrix} a & -b & c & -d \\ b & a & -d & -c \\ -c & d & a & -b \\ d & c & b & a \end{pmatrix} \tag{A3}$$

with the generalized angular coordinates $\mathbf{\Omega}_\mathrm{r} = (\vartheta_\mathrm{r}, \chi_\mathrm{r}, \varphi_\mathrm{r})$ and the corresponding unit vector $\hat{\mathbf{u}}_\mathrm{r} = (-d, -c, -b, a)^\mathrm{T}$. Using $\mathbf{R}^\mathrm{T}(\mathbf{\Omega}_\mathrm{r}) \cdot \hat{\mathbf{u}}_\mathrm{r}$, the random unit vector $\hat{\mathbf{u}}_\mathrm{r}$ is rotated, resulting in a unit vector in the positive z direction $\hat{\mathbf{u}}_z = (0, 0, 0, 1)^\mathrm{T}$.

(ii) Using an additional rotation matrix

$$\mathbf{\Psi}(\psi) = \mathbf{R}(\psi, 0, 0) = \begin{pmatrix} \cos\psi & -\sin\psi & 0 & 0 \\ \sin\psi & \cos\psi & 0 & 0 \\ 0 & 0 & \cos\psi & -\sin\psi \\ 0 & 0 & \sin\psi & \cos\psi \end{pmatrix}, \tag{A4}$$

describing a counterclockwise rotation by ψ, the unit vector $\hat{\mathbf{u}}_\psi = (0, 0, -\sin\psi, \cos\psi)^\mathrm{T}$ results from

$$\hat{\mathbf{u}}_\psi = (0, 0, -\sin\psi, \cos\psi)^\mathrm{T} = \mathbf{\Psi}(\psi) \cdot \hat{\mathbf{u}}_z. \tag{A5}$$

(iii) Applying

$$\hat{\mathbf{u}}_{\psi,\mathbf{\Omega}_\mathrm{r}} = \mathbf{R}(\mathbf{\Omega}_\mathrm{r}) \cdot \hat{\mathbf{u}}_\psi, \tag{A6}$$

the intermediate result $\hat{\mathbf{u}}_\psi$ is back-transformed to the initial coordinate system. Combining (i)–(iii)

$$\mathbf{\Xi}(\mathbf{\Omega}_\mathrm{r}, \psi) = \mathbf{R}(\mathbf{\Omega}_\mathrm{r}) \cdot \mathbf{\Psi}(\psi) \cdot \mathbf{R}^\mathrm{T}(\mathbf{\Omega}_\mathrm{r}) \tag{A7}$$

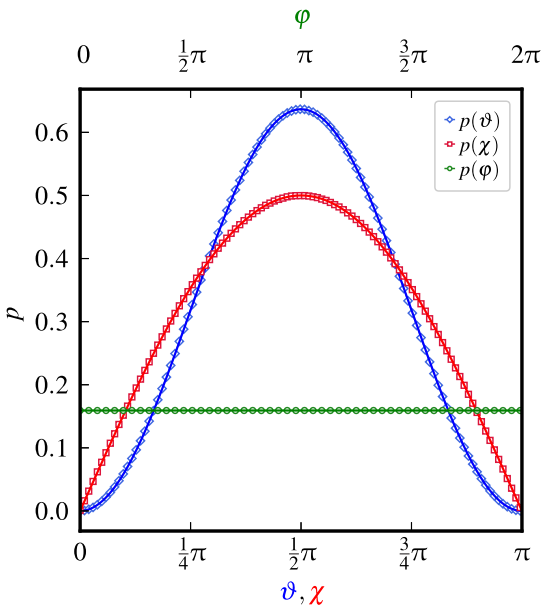

FIG. 3. Probability densities of polar angles ϑ, χ, and φ obtained during 10^{10} random rotations according to Eq. (A8) with $\Delta_\mathrm{rot} = 1/2$ starting from the initial orientation $\hat{\mathbf{u}}_1 = (0, 0, 0, 1)^\mathrm{T}$. The solid lines represent the theoretically expected probability densities.

results, which again is a rotation matrix in $\mathbb{R}^4$ with the properties $\mathbf{\Xi}^\mathrm{T}(\mathbf{\Omega}_\mathrm{r}, \psi) \cdot \mathbf{\Xi}(\mathbf{\Omega}_\mathrm{r}, \psi) = \mathbf{I}$ and $\det(\mathbf{\Xi}(\mathbf{\Omega}_\mathrm{r}, \psi)) = 1$, where $\mathbf{I}$ denotes the identity. Choosing a random orientation vector $\mathbf{\Omega}_\mathrm{r}$ and a random number $-\Delta_\mathrm{rot} \leqslant \psi \leqslant \Delta_\mathrm{rot}$ with probability density $p(\psi) = 1/(2\Delta_\mathrm{rot})$, a consecutive application of $\mathbf{\Xi}(\mathbf{\Omega}_\mathrm{r}, \psi)$

$$\hat{\mathbf{u}}_{N+1} = \mathbf{\Xi}(\mathbf{\Omega}_\mathrm{r}, \psi) \cdot \hat{\mathbf{u}}_N \tag{A8}$$

to a particles' orientation $\hat{\mathbf{u}}_N$ at step N leads to a homogeneous exploration of a unit hypersphere's hypersurface as shown in Fig. 3. The probability densities are obtained during 10^{10} random rotations employing Eq. (A8) using $\Delta_\mathrm{rot} = 1/2$ and starting from the initial orientation $\hat{\mathbf{u}}_1 = (0, 0, 0, 1)^\mathrm{T}$. The solid lines are the theoretical probability densities $p(\vartheta) = 2\sin^2\vartheta/\pi$, $p(\chi) = \sin\chi/2$, and $p(\varphi) = 1/(2\pi)$. The excellent agreement of the obtained probability densities with the theoretical predictions proves a homogeneous exploration of the rotational configuration space by the described method.

[1] S. Torquato, J. Chem. Phys. **149**, 020901 (2018).
[2] H. Kamerlingh Onnes, Proc. K. Ned. Akad. Wet. **4**, 125 (1902).
[3] B. Jäger, Sitzungsber. Akad. Wiss. Wien, Math.-Naturwiss. Kl., Abt. 2A **105**, 15 (1896).
[4] J. D. van der Waals, Proc. K. Ned. Akad. Wet. **1**, 138 (1899).
[5] L. Boltzmann, Sitzungsber. Akad. Wiss. Wien, Math.-Naturwiss. Kl., Abt. 2A **105**, 695 (1896).
[6] L. Boltzmann, Proc. K. Ned. Akad. Wet. **1**, 398 (1899).
[7] L. Onsager, Ann. NY Acad. Sci. **51**, 627 (1949).
[8] J. E. Mayer and M. G. Mayer, *Statistical Mechanics* (Wiley, New York, 1940)
[9] M. N. Rosenbluth and A. W. Rosenbluth, J. Chem. Phys. **22**, 881 (1954).
[10] F. H. Ree and W. G. Hoover, J. Chem. Phys. **40**, 939 (1964).

[11] F. H. Ree and W. G. Hoover, J. Chem. Phys. **46**, 4181 (1967).
[12] E. J. Janse van Rensburg, J. Phys. A: Math. Gen. **26**, 4805 (1993).
[13] S. Labík, J. Kolafa, and A. Malijevský, Phys. Rev. E **71**, 021105 (2005).
[14] R. J. Wheatley, Phys. Rev. Lett. **110**, 200601 (2013).
[15] A. J. Schultz and D. A. Kofke, Phys. Rev. E **90**, 023301 (2014).
[16] P. A. Monson and M. Rigby, Mol. Phys. **35**, 1337 (1978).
[17] D. Frenkel, J. Phys. Chem. **91**, 4912 (1987).
[18] M. Rigby, Mol. Phys. **66**, 1261 (1989).
[19] W. R. Cooney, S. M. Thompson, and K. E. Gubbins, Mol. Phys. **66**, 1269 (1989).
[20] J. A. C. Veerman and D. Frenkel, Phys. Rev. A **45**, 5632 (1992).
[21] C. Vega, Mol. Phys. **92**, 651 (1997).
[22] A. Y. Vlasov, X.-M. You, and A. J. Masters, Mol. Phys. **100**, 3313 (2002).
[23] P. Marienhagen, R. Hellmann, and J. Wagner, Phys. Rev. E **104**, 015308 (2021).
[24] P. Marienhagen and J. Wagner, Phys. Rev. E **105**, 014125 (2022).
[25] L. Tonks, Phys. Rev. **50**, 955 (1936).
[26] P. C. Hemmer, J. Chem. Phys. **42**, 1116 (1965).
[27] N. Metropolis, A. W. Rosenbluth, M. N. Rosenbluth, A. H. Teller, and E. Teller, J. Chem. Phys. **21**, 1087 (1953).
[28] C. Zhang and B. M. Pettitt, Mol. Phys. **112**, 1427 (2014).
[29] M. Á. G. Maestre, A. Santos, M. Robles, and M. L. de Haro, J. Chem. Phys. **134**, 084502 (2011).
[30] F. H. Ree and W. G. Hoover, J. Chem. Phys. **40**, 2048 (1964).
[31] M. Adda-Bedia, E. Katzav, and D. Vella, J. Chem. Phys. **129**, 144506 (2008).
[32] J. H. Conway and N. J. A. Sloane, *Sphere Packings, Lattices and Groups*, Vol. 290 (Springer, New York, 2013).
[33] N. Clisby and B. M. McCoy, J. Stat. Phys. **122**, 15 (2006).
[34] A. Isihara, J. Chem. Phys. **18**, 1446 (1950).
[35] A. Isihara and T. Hayashida, J. Phys. Soc. Jpn. **6**, 40 (1951).
[36] H. Hadwiger, Experientia **7**, 395 (1951).
[37] J. K. Singh and D. A. Kofke, Phys. Rev. Lett. **92**, 220601 (2004).
[38] S. Torquato and Y. Jiao, Phys. Rev. E **87**, 022111 (2013).
[39] E. Herold, R. Hellmann, and J. Wagner, J. Chem. Phys. **147**, 204102 (2017).
[40] C. Vega and S. Lago, Comput. Chem. **18**, 55 (1994).
[41] A. Perez-Gracia and F. Thomas, Adv. Appl. Clifford Algebras **27**, 523 (2017).
[42] S. Torquato and Y. Jiao, arXiv:2203.16764.
[43] R. Schneider, *Convex Bodies: The Brunn-Minkowski Theory*, Vol. 151 (Cambridge University Press, Cambridge, 2014).
[44] L. A. Santaló, *Integral Geometry and Geometric Probability* (Cambridge University Press, Cambridge, 2004).
[45] T. Boublík, Mol. Phys. **27**, 1415 (1974).
[46] M. Rigby, Mol. Phys. **78**, 21 (1993).
[47] M. Francová, J. Kolafa, P. Morávek, S. Labík, and A. Malijevský, Collect. Czech. Chem. Commun. **73**, 413 (2008).

5.4 Publication IV: Equation of state of hard lenses: A combined virial series and simulation approach

Philipp Marienhagen and Joachim Wagner,
Phys. Rev. E **106**, 014101 (2022).
DOI: 10.1103/PhysRevE.106.014101

Contribution:
This work was conceptualised by P.M. and J.W., P.M. implemented all algorithms, performed calculations, and analysed the results. The draft was written by P.M. and revised by P.M. and J.W. The work was supervised by J.W.

Equation of state of hard lenses: A combined virial series and simulation approach

Philipp Marienhagen and Joachim Wagner*
Institut für Chemie, Universität Rostock, 18051 Rostock, Germany

(Received 15 March 2022; accepted 23 May 2022; published 1 July 2022)

We provide highly accurate equation-of-state data for the isotropic phase of hard lenses obtained by means of cluster Monte Carlo simulations. This data is analyzed using a virial approach considering coefficients up to the order eight and Carnahan-Starling type closure relations for the virial series. The comparison with previously investigated systems consisting of hard, oblate ellipsoids of revolution allows insights into the detailed influence of the particle geometry. We propose a generalized Carnahan-Starling approach as a heuristic equation of state for the isotropic phase of hard lenses that in first approximation shows the same dependence on the excess part of the excluded volume as identified for oblate, hard lenses of revolution.

DOI: 10.1103/PhysRevE.106.014101

I. INTRODUCTION

Hard-body many-particle systems have served for more than a century as model systems for the self-organization of molecular matter [1] with impacts on colloidal soft matter [2–5] or granular systems [6] on the meso- or macroscale. Anisometric particles are of particular interest for the understanding of liquid crystals which attracted large scientific interest, both from the viewpoint of fundamental research and, due to manyfold technical applications, from the viewpoint of applied science [7,8].

While the aspect ratio ν, i.e., the ratio of the shortest to longest extent, is the property that essentially influences the phase behavior and equation of state of such systems, numerous studies are dedicated to the influence of the specific shape beyond the aspect ratio [9–11].

A comprehensive description for differently shaped hard particle systems' equations of state depending on their aspect ratio has often been in the focus of scientific work [12–15] with relevance for classical density functional theory [16]. In their seminal work, Isihara and Hadwiger independently showed that the second virial coefficient of convex hard bodies can be described analytically using fundamental geometric measures of the respective geometry [17–19].

Based on the knowledge of second virial coefficients B_2, we have previously reported that reduced higher-order virial coefficients $\tilde{B}_i = B_i/B_2^{i-1}$, where B_i is the virial coefficient of order i of hard, oblate, ellipsoids of revolution and hard lenses, show in first approximation a universal dependence on the excess part of the mutual excluded volume [20,21].

The aim of this contribution is to calculate equation-of-state data for hard lenses as a geometry similar to hard, oblate ellipsoids of revolution, however, exhibiting an equatorial singularity of surface curvature in contrast to ellipsoids. The comparison of hard, oblate ellipsoids of revolution and hard lenses is a suitable choice, since the phase behavior of both geometries is known and contains the same phases [22–24]. In the case of hard lenses metastable glassy phases have also been reported [25,26].

As previously shown for ellipsoids, cluster Monte Carlo simulations as a biased variant of the original Metropolis scheme are the method of choice for the computation of precise equation-of-state data of hard, anisotropic particles in the (N, p, T) ensemble at constant number of particles N, constant pressure p and constant temperature T. Since in the case of hard-body interaction, the potential energy is either infinite for overlaps or zero otherwise, deviations from the ideal-gas behavior are for such systems independent on the temperature and therewith the thermal energy $\beta^{-1} = k_B T$. Hence, the relevant quantity with impact on the real gas behavior is solely the particle number density ϱ and the related volume fraction $\varphi = V_P \varrho$, where V_P denotes the particle volume.

II. THEORETICAL BACKGROUND

In this paper, equation-of-state data of hard lenses is determined in the isobaric-isothermal (N, p, T) ensemble. As previously shown, employing a cluster Monte Carlo (MC) algorithm [27–29] gives access to precise equation-of-state data with comparatively small computational effort. In comparison to classical (N, p, T) MC, the cluster MC approach allows larger volume fluctuations leading to a better exploration of the configuration space.

The theoretical background of this biased MC technique is explicitly described in [29]. To adapt the cluster-MC approach to systems consisting of hard lenses, the closest surface distance for this geometry needs to be determined reliably with a fast method.

A. Closest surface distance of lenses

A lens is the section of two spheres with radius R_0 whose centers are less than $2R_0$ apart from each other. The generating spheres' radius R_0, depending on the equatorial radius r_{eq} and

*joachim.wagner@uni-rostock.de

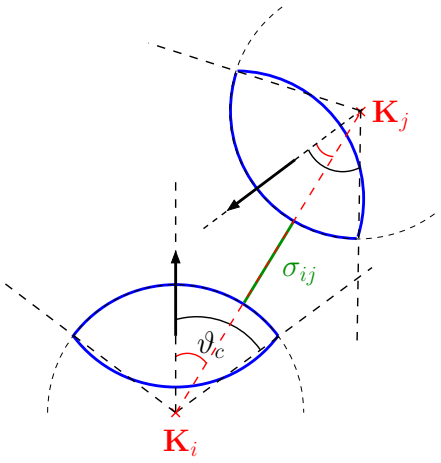

FIG. 1. Closest surface distance between undercritically inclined lenses. In this case (i) the closest surface distance is between the spherical caps of both lenses.

the aspect ratio ν, reads as

$$R_0 = \frac{1+\nu^2}{2\nu} r_{\mathrm{eq}}. \tag{1}$$

In principle, the presented algorithm to determine the closest surface distance σ_{ij} of lenses is an extension of the overlap algorithm of lenses in [21]. It assumes an overlap-free constellation of two lenses i and j with centers of mass $\mathbf{r}_i$ and $\mathbf{r}_j$ as well as orientations $\hat{\mathbf{u}}_i$ and $\hat{\mathbf{u}}_j$. The closest surface distance between two lenses can occur (i) between two spherical caps, (ii) between a spherical cap of one and the equatorial circle of the other lens, or (iii) between the equatorial circles of two lenses.

Let $\mathbf{K}_i$ and $\mathbf{K}_j$ be the centers of the most distant generating spheres and $\hat{\mathbf{u}}_\mathrm{s} = (\mathbf{K}_j - \mathbf{K}_i)/\|\mathbf{K}_j - \mathbf{K}_i\|$ the direction of their distance vector. Let us further define $\vartheta_\mathrm{c} = \arccos[(1-\nu^2)/(1+\nu^2)]$ as aperture of the critical cone. If the angles enclosed between the distance vector $\hat{\mathbf{u}}_s$ and both directors $\hat{\mathbf{u}}_i$ and $\hat{\mathbf{u}}_j$ are smaller than the critical angle ϑ_c, both lenses are undercritically inclined. In this case the closest surface distance is between two spherical caps and is given by

$$\sigma_{ij} = \|\mathbf{K}_j - \mathbf{K}_i\| - 2\,R_0 \tag{2}$$

as visualized in Fig. 1.

Otherwise at least one equatorial circle limits the closest surface distance. The point on the equator of lens j closest to $\mathbf{K}_i$ is

$$\mathbf{P}_j = \mathbf{r}_j + r_{\mathrm{eq}} \frac{\hat{\mathbf{u}}_j \times [(\mathbf{K}_i - \mathbf{r}_j) \times \hat{\mathbf{u}}_j]}{\|\hat{\mathbf{u}}_j \times [(\mathbf{K}_i - \mathbf{r}_j) \times \hat{\mathbf{u}}_j]\|}, \tag{3}$$

leading to the closest surface distance σ_{ij}

$$\sigma_{ij} = \|\mathbf{P}_j - \mathbf{K}_i\| - R_0 \tag{4}$$

under the condition

$$\frac{\mathbf{P}_j - \mathbf{K}_i}{\|\mathbf{P}_j - \mathbf{K}_i\|} \cdot \hat{\mathbf{u}}_i > \cos\vartheta_\mathrm{c}, \tag{5}$$

corresponding to case (ii). By interchanging the indices i and j in Eq. (3), Eq. (4) and the constraint Eq. (5), the closest surface distance between the equator of lens i and lens j is obtained (Fig. 2).

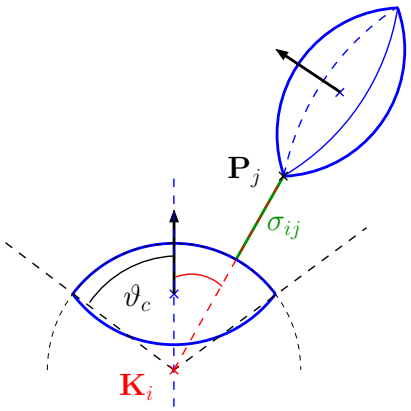

FIG. 2. Closest surface distance of critically inclined lenses case ii) fulfilling the constraint in Eq. (5). The closest surface distance occurs between the equator of one lens and the spherical cap of the other.

The remaining case (iii), i.e., the closest surface distance between both equators is illustrated in Fig. 3, where the constraint Eq. (5) is not fulfilled. The remaining problem is the closest distance between possibly incongruent circles in the three-dimensional space, which can be reliably determined using the algorithm of Vranek [30].

The described approach was validated by a numerical brute force routine using a parametrized surface and comparison to data computed by means of a standard (N, p, T) algorithm for different densities and aspect ratios.

B. Simulation details

Equation-of-state data for isotropic and nematic phases is calculated from compression simulations of systems typically with 1000 particles initialized from a cubic lattice with randomly aligned directors at a volume fraction of $\varphi = 0.05$. These are equilibrated for 10^6 steps and subsequently compressed to the pressure of interest. After an additional equilibration phase, a production run with 5×10^7 steps is performed. A step is hereby defined as N random particle displacement or rotation attempts and a single volume fluctuation attempt.

To determine the limits of the isotropic phase for aspect ratios that transition into a solid phase additional expansion simulations from dense monoclinic SM2 crystals containing between 972 and 1040 particles are performed. Here, addi-

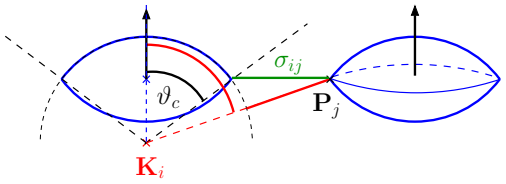

FIG. 3. Closest surface distance of critically inclined lenses case iii) which do not fulfill the constraint in Eq. (5). Here the closest surface distance lies between both equators and can be related to the closest distance between two possibly incongruent circles in the three-dimensional space.

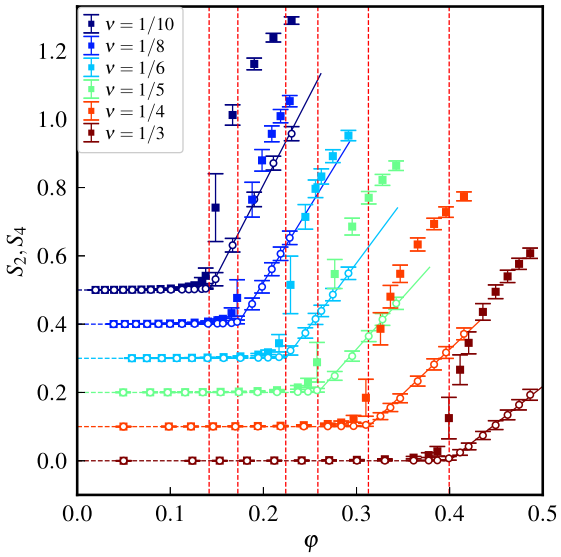

FIG. 4. Order parameters S_2 (closed squares) and S_4 (open circles) depending on the volume fraction φ for lenses of selected aspect ratios ν separated by arbitrary offsets. The vertical, dashed red lines represent the critical volume fractions φ_c determined by the roots of the linear increasing order parameters $S_4(\varphi)$ within the nematic phase.

tional shape fluctuations of the simulation box as described in [29] at constant volume are introduced whereby independent subsequent runs with at least 2×10^8 steps are performed.

The characteristic length δ steering the cluster formation probability is tuned during the second equilibration phase to obtain $N_b/N \approx 1/4$ where N_b is the number of created bonds. This guarantees percolation rejections to be less than 1 %, even for highly anisotropic particles.

III. RESULTS AND DISCUSSION

A. Phase boundaries in the hard-lens system

The aim of this work is the calculation of equation-of-state data in the isotropic phase of hard lenses. In the first step, the phase boundaries of the isotropic phase are determined. In analogy to oblate, hard ellipsoids of revolution, we expect transitions from the isotropic to nematic, plastic crystalline, and monoclinic crystalline phases. In the following, we map the phase diagram by evaluating characteristic observables.

The orientational correlation in nematic phases can be quantified by the nematic order parameters

$$S_2 = \left\langle \tfrac{1}{2}\left(3x_i^2 - 1\right)\right\rangle_{x_i} \tag{6}$$

and

$$S_4 = \left\langle \tfrac{1}{8}\left(35x_i^4 - 30x_i^2 + 3\right)\right\rangle_{x_i}. \tag{7}$$

To just identify the existence of nematic order, we use as previously described [29] the inner product $x_i = \hat{\mathbf{u}}_j.\hat{\mathbf{u}}_k$ of the particle orientations $\hat{\mathbf{u}}_j$ and $\hat{\mathbf{u}}_k$. To fulfill the minimum image convention, we again restrict the averages to the periodic boundary conditions. In Fig. 4, the order parameters S_2 and S_4 are displayed in dependence on the volume fraction φ. Since the increase of S_4 is more pronounced than that of S_2, we extrapolate S_4 to its root to determine the critical volume fraction φ_c for the isotropic-nematic phase transition. The critical volume fractions φ_c and reduced coexistence pressures $\beta p_c r_{eq}^3$ are compiled in Table I.

TABLE I. Phase boundaries for the isotropic phase of hard lenses.

ν	Phase Transition	φ_c	$\beta p_c r_{eq}^3$
1/10	I → N	0.142(2)	2.15(4)
1/8	I → N	0.173(2)	2.25(4)
1/6	I → N	0.224(2)	2.48(4)
1/5	I → N	0.258(2)	2.65(5)
1/4	I → N	0.313(2)	3.07(5)
1/3	I → N	0.400(2)	4.09(7)
1/2	I → SM2	0.555(3)	8.10(19)
2/3	I → PS	0.606(6)	7.9(4)
4/5	I → PS	0.505(6)	2.33(10)
10/11	I → PS	0.480(5)	1.54(7)

In analogy to the phase behavior of oblate, hard ellipsoids of revolution, for aspect ratios $\nu \geqslant 1/2$ transitions into solid phases exist. To map the phase boundaries between the isotropic phase and the monoclinic crystalline SM2 phase, expansion simulations starting from dense SM2 crystals are performed. While for aspect ratio $\nu = 1/2$ a direct transition from the crystalline SM2 phase to the isotropic phase is observed, for $\nu \geqslant 2/3$, first a transition to a plastic solid phase occurs, followed finally at lower densities by the transition to the isotropic fluid phase. The reduced coexistence pressures and respective uncertainties are displayed in Fig. 5 depending on the volume fraction φ for different aspect ratios ν. The

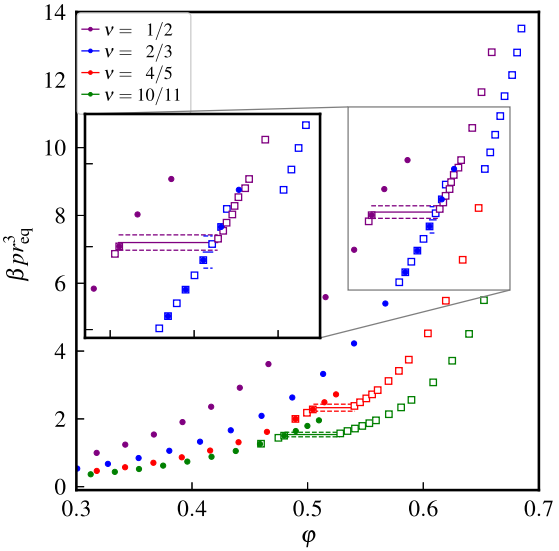

FIG. 5. Reduced pressure $\beta p r_{eq}^3$ depending on the volume fraction φ for hard lenses of selected aspect ratios ν. The closed circles represent data from compression simulations of the fluid phase, while open squares result from expansion simulations of solid monoclinic crystals. The horizontal solid lines represent the determined coexistence pressures with their uncertainties indicated by dashed horizontal lines.

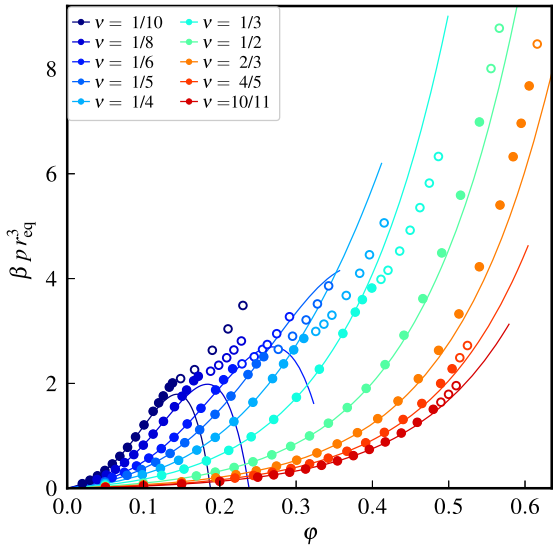

FIG. 6. Reduced pressure $\beta p r_{eq}^3$ depending on the volume fraction φ for hard lenses of selected aspect ratios ν. Closed circles represent equation-of-state data within the isotropic phase, while open circles display data beyond the phase transition. The solid lines represent the virial series using virial coefficients up to order eight from [21].

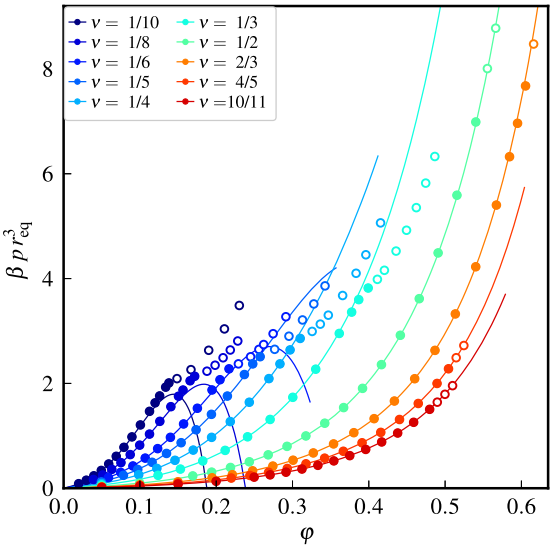

FIG. 7. Reduced pressure $\beta p r_{eq}^3$ depending on the volume fraction φ for hard lenses of selected aspect ratios ν. Closed circles represent equation-of-state data within the isotropic phase, while open circles display data beyond the phase transition. The solid lines represent the virial series up to order eight with a generalized Parsons-type truncation correction according to Eq. (11).

reduced coexistence pressures and critical volume fractions are additionally compiled in Table I.

B. Equation of state

Due to the absence of attractive interactions in the hard-lens system, the isotropic phase is supercritical and thus can be described using the virial approach

$$Z = \frac{p}{\varrho k_B T} = 1 + \sum_{i=2}^{\infty} B_i^* \varphi^{i-1} \tag{8}$$

in terms of the real gas factor Z. In this expansion in the volume fraction φ, the reduced virial coefficients B_i^* account for deviations from the ideal-gas equation of state. Here, the reduced virial coefficient B_i^* of order i accounts for real-gas effects induced by the formation of i-particle clusters.

As a first approach, we compare the simulation data, compiled in the Supplemental Material [31], with a virial approach using recently published hard-lens virial coefficients up to order $i = 8$ [21]. As displayed in Fig. 6, the initial departure from the ideal-gas behavior is excellently described for all aspect ratios in the low-density limit. Approaching the high-density limit of the isotropic phase, however, significant deviations can be observed when truncating the virial expansion for orders $i \geqslant 9$. This truncation even leads to unphysical, negative real gas factors for highly anisotropic particles.

Different approaches taking the contribution of so-far unknown, higher-order virial coefficients into account are discussed. Most of them are based on the Carnahan-Starling series [32] approximating the reduced virial coefficients of hard spheres as $B_i^* \approx i^2 + i - 2$. The reason why this approximation works surprisingly well for hard spheres is still not understood [33]. Inserting the Carnahan-Starling approximation in Eq. (8) leads to the closed expression

$$Z = \frac{1 + \varphi + \varphi^2 - \varphi^3}{(1-\varphi)^3} \tag{9}$$

for the real gas factor under the obvious constraint $\varphi < 1$. A common approach to correct for truncation effects is the use of all known virial coefficients up to order i_{max} for a given geometry and to approximate the contribution of the unknown ones by the complement of the Carnahan-Starling equation, where the factor $B_2^*/B_2^{*,HS}$ takes the specific shape into account. Here, B_2^* is the reduced, second virial coefficient of the respective geometry and $B_2^{*,HS} = 4$ is the reduced second virial coefficient of hard spheres [34,35]. This leads to the relation

$$Z = 1 + \sum_{i=2}^{i_{max}} B_i^* \varphi^{i-1} + \frac{B_2^*}{B_2^{*,HS}} \sum_{i=i_{max}+1}^{\infty} B_i^{*,HS} \varphi^{i-1} \tag{10}$$

for the real gas factor. In our case, using $i_{max} = 8$,

$$Z = 1 + \sum_{i=2}^{8} B_i^* \varphi^{i-1} + \frac{B_2^*}{4} \frac{2\varphi^8(35\varphi^2 - 78\varphi + 44)}{(1-\varphi)^3} \tag{11}$$

is obtained [29]. The solid lines in Fig. 7 represent the truncation-corrected equation of state Eq. (11). For moderately anisotropic lenses with aspect ratio $\nu \geqslant 1/5$ the simulation data are within the stability region of the isotropic phase indicated by closed symbols in good agreement to the suggested truncation correction. For higher anisotropic lenses, however, this correction fails. This is in accordance to the findings for oblate hard ellipsoids of revolution, where identically this correction works reasonably up to the same anisotropy parameter $\nu \geqslant 1/5$ as recently reported. This indicates that not the specific shape, but the extent of the short and long

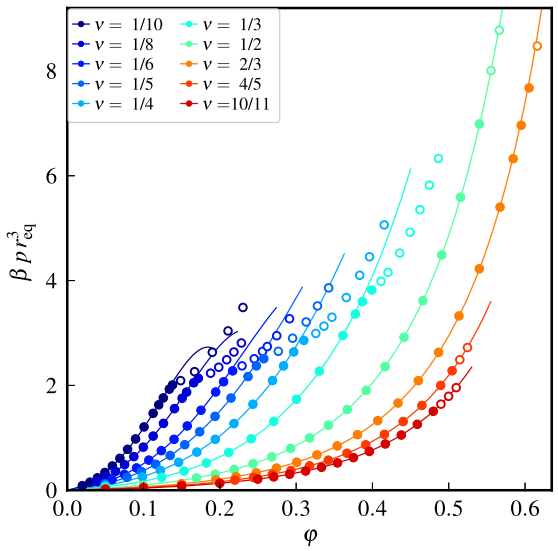

FIG. 8. Reduced pressure $\beta p r_{eq}^3$ depending on the volume fraction φ for selected aspect ratios of hard lenses. The solid lines represent least-squares fits of the proposed, generalized Carnahan-Starling equation of state [Eq. (12)] to the simulation data. Closed symbols represent equation-of-state data of the isotropic phase, while open symbols display data beyond the phase transition.

axes causes this effect and confirms our assumption that long-range orientational correlations not reflected by clusters of limited size, but intrinsically taken into account in simulations using several hundred particles are a plausible physical reason. The spatial extent of orientational correlations drastically increases for highly anisotropic particles and cannot be taken into account by the second virial coefficient B_2^* as a single shape-dependent correction factor: the second virial coefficient only reflects short-range orientational correlations in two-particle clusters. Here, the maximum interaction length, where the orientation plays a role, equals in the case of hard-body interaction the maximum contact distance, i.e., the particles largest extent.

To provide a simple, heuristic equation for the isotropic phase of hard lenses, we provide in analogy to hard, oblate ellipsoids of revolution, a generalized Carnahan-Starling approach, where the real gas factor Z reads as

$$Z = \frac{1 + \gamma_0\varphi + \gamma_1\varphi^2 - \gamma_2\varphi^3}{(1-\varphi)^3}. \tag{12}$$

Choosing the parameter $\gamma_0 = B_2^* - 3$, the virial expansion is asymptotically recovered in the low-density limit. Since the second virial coefficient B_2^* is analytically known for convex shapes, just two parameters γ_1 and γ_2 need to be determined from least-squares fits of simulation data in the isotropic phase employing Eq. (12). As visible in Fig. 8, the simulation data can be described excellently using this simple approach. The optimum parameters γ_1 and γ_2 are compiled in Table II depending on the aspect ratio ν.

C. Comparison with oblate ellipsoids

The dimensionless real gas factor Z is a quantity that describes the equation of state independent of topological

TABLE II. Optimium parameters γ_1 and γ_2 obtained from least-squares fits of the simulation data using the generalized Carnahan-Starling approach [Eq. (12)] depending on the aspect ratio ν. Additionally, the density limits of the data considered are indicated.

		Coefficients	
ν	Limits	γ_1	γ_2
1/10	$0.020 < \varphi < 0.142$	111.14681(13)	764.7883(13)
1/8	$0.039 < \varphi < 0.173$	67.73726(20)	382.6916(16)
1/6	$0.059 < \varphi < 0.224$	34.83358(16)	151.8094(10)
1/5	$0.049 < \varphi < 0.258$	21.57179(10)	77.6509(6)
1/4	$0.050 < \varphi < 0.313$	12.60231(9)	36.5776(4)
1/3	$0.050 < \varphi < 0.400$	6.17223(7)	13.15453(20)
1/2	$0.050 < \varphi < 0.555$	2.31013(13)	3.2334(4)
2/3	$0.050 < \varphi < 0.606$	1.45092(7)	1.75807(14)
4/5	$0.050 < \varphi < 0.505$	1.17826(10)	1.28442(25)
10/11	$0.050 < \varphi < 0.480$	1.07893(12)	1.1153(4)

parameters of the respective shape depending on the volume fraction φ. The comparison with our previously published data [29] shows that systematically at any volume fraction the real gas factor of lenses exceeds that of ellipsoids with the same aspect ratio (Fig. 9). Despite the shape of both oblate solids of revolution is quite similar, the detailed geometry has a significant impact on the equation of state already for moderately anisotropic particles. While at small anisotropies with $\nu \geqslant 4/5$ the real gas factors approximately coincide, already at $\nu = 1/2$ significant differences are observed. Even larger differences appear for aspect ratios where an isotropic-nematic phase transition occurs.

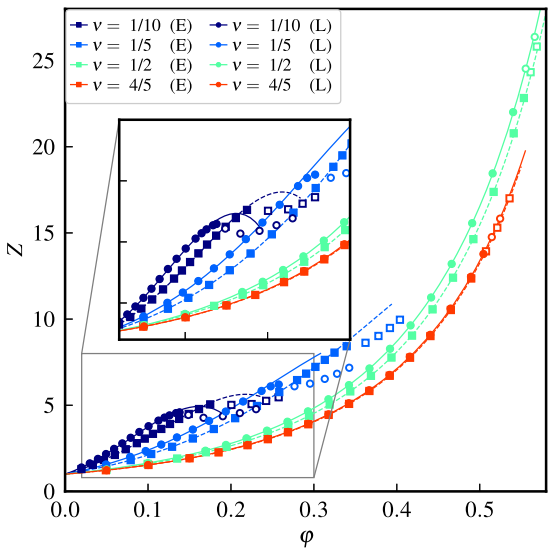

FIG. 9. Comparison of real gas factors Z for hard lenses and hard, oblate ellipsoids of revolution depending on the volume fraction φ for selected aspect ratios ν. The dashed lines with squares indicate data of ellipsoids, while that of lenses is displayed as circles with solid lines. Data for objects with the same aspect ratio are displayed with the same color. The data for ellipsoids are from [29].

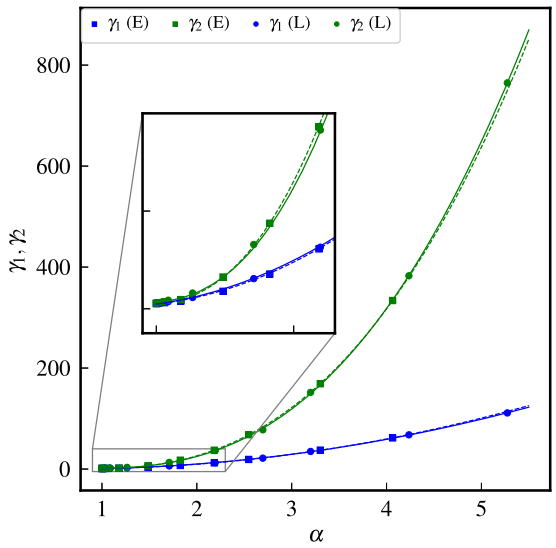

FIG. 10. Heuristic parameters γ_1 and γ_2 of the suggested, Carnahan-Starling type equation of state [Eq. (12)] depending on the excess part of the mutual excluded volume α [Eq. (13)]. Data of ellipsoids are displayed by dashed lines and squares, that of lenses by circles and solid lines.

This is in accordance to the orientationally averaged excluded volume equal to the second virial coefficient: The reduced second virial coefficient $B_2^* = B_2/V_\mathrm{P}$, i.e., the second virial coefficient normalized to the respective particle volume V_P, of lenses exceeds that of ellipsoids of revolution at the same aspect ratio ν. This is caused by the lenses' strongly increasing contribution of the equatorial singularity to the mean radius of curvature with rising anisometry [36]. As a further effect, a shift of the isotropic-nematic phase transition of lenses to lower critical volume fractions φ_c compared to oblate ellipsoids of revolution at the same aspect ratio ν is observed.

We have previously shown that reduced virial coefficients $\tilde{B}_i = B_i/B_2^{i-1}$ in first approximation show a universal behavior with respect to the rescaled excess part of the excluded volume, also known as nonsphericity parameter. The latter quantity is defined as

$$\alpha = \frac{B_2 - V_\mathrm{P}}{3V_\mathrm{P}} \tag{13}$$

with B_2 denoting the second virial coefficient and V_P the volume of the respective geometry. For both oblate shapes, the suggested generalized Carnahan-Starling relations with only two heuristic parameters γ_1 and γ_2 describe the equation-of-state data within the isotropic phase of both geometries surprisingly well.

Analyzing the dependence of both heuristic parameters on the rescaled excess part of the excluded volume α identically shows in first approximation a universal behavior, nearly independent on the specific particle shape (Fig. 10). This again indicates that the excess part of the mutual excluded volume is the essential quantity that determines the equation of state for oblate, hard solids of revolution. The solid and dashed lines as a guide to the eye are second-order polynomials in the case of γ_1 and fourth-order polynomials in the case of γ_2.

IV. SUMMARY AND OUTLOOK

As previously shown, cluster MC is an efficient method to calculate equation-of-state data of hard-body systems within the (N, p, T) ensemble with high accuracy and comparatively small numerical effort. The benefit of cluster MC increases especially in the case of anisotropic particles with the complexity of the overlap problem for the particle shape of interest. In addition to the contact problem, for cluster MC, however, at least an estimation for the closest surface distance is required.

We describe a method to exactly determine the closest surface distance for hard lenses based on our previously published contact algorithm [21]. Herewith, after tracing the phase boundaries of the isotropic phase of the hard-lens fluid, we calculated novel, precise equation-of-state data in the stability region of this phase. With access to equation-of-state data of both, hard, oblate ellipsoids of revolution and hard lenses, the influence of the detailed particle shape beyond the aspect ratio is analyzed.

The equation-of-state data for hard lenses is compared to a virial approach using recently published virial coefficients up to order eight and truncation effects, caused by so far unknown higher-order virial coefficients, are analyzed. For moderately anisotropic lenses with aspect ratio $\nu \geqslant 1/5$, a Parson-type correction is capable of reasonably describing the equation of state in the isotropic phase. Although this approach replaces unknown, higher virial coefficients by rescaled hard-sphere coefficients with a scaling factor taking only the second virial coefficient and thus two-particle interactions into account, the Parson correction is an excellent closure relation for moderately anisotropic particles within the isotropic phase. This correction, however, fails for highly anisotropic lenses as previously observed in the case of oblate, hard ellipsoids of revolution. As a heuristic approach, we suggest a generalized Carnahan-Starling ansatz with in addition to the analytically known second virial coeffiecient two adjustable parameters γ_1 and γ_2. This heuristic approach describes the equation of state within the isotropic phase surprisingly well despite its simplicity.

A significant shape dependence is observed for the real gas factor Z as a function of the volume fraction φ at identical aspect ratio ν. The parameters γ_1 and γ_2, however, show in first approximation for both oblate geometries a universal dependence on the rescaled excess part of the mutual excluded volume α. Hereby, a reliable interpolation for equation-of-state data for unknown aspect ratios is possible.

To gain further insights, if this seemingly universal behavior holds for different, possibly prolate geometries, additional equation-of-state data for such systems needs to be analyzed. Possible candidates could be prolate ellipsoids of revolution and spherocylinders, where the contact problem is already solved and differences in the phase behavior are known.

ACKNOWLEDGMENTS

P.M. gratefully acknowledges financial support by the Universität Rostock within the Ph.D. scholarship program.

[1] J. A. Barker and D. Henderson, Rev. Mod. Phys. **48**, 587 (1976).
[2] P. N. Pusey, *Colloidal Suspensions in Liquids, Freezing and Glass Transition* (Elsevier, 1991), pp. 765–942.
[3] S. Sacanna and D. J. Pine, Curr. Opin. Colloid Interface Sci. **16**, 96 (2011).
[4] M. J. Solomon, Curr. Opin. Colloid Interface Sci. **16**, 158 (2011).
[5] P. Tierno, Phys. Chem. Chem. Phys. **16**, 23515 (2014).
[6] P.-G. de Gennes, Rev. Mod. Phys. **71**, S374 (1999).
[7] I. Muševič, Materials **11**, 24 (2017).
[8] I. I. Smalyukh, Annu. Rev. Condens. Matter Phys. **9**, 207 (2018).
[9] D. Frenkel, B. M. Mulder, and J. P. McTague, Phys. Rev. Lett. **52**, 287 (1984).
[10] P. Bolhuis and D. Frenkel, J. Chem. Phys. **106**, 666 (1997).
[11] D. van der Beek and H. N. W. Lekkerkerker, Langmuir **20**, 8582 (2004).
[12] I. Nezbeda, Chem. Phys. Lett. **41**, 55 (1976).
[13] T. Boublík, Mol. Phys. **42**, 209 (1981).
[14] T. Boublík and I. Nezbeda, Collect. Czech. Chem. Commun. **51**, 2301 (1986).
[15] Y. Song and E. A. Mason, Phys. Rev. A **41**, 3121 (1990).
[16] Y. Singh, Phys. Rep. **207**, 351 (1991).
[17] A. Isihara, J. Chem. Phys. **18**, 1446 (1950).
[18] A. Isihara and T. Hayashida, J. Phys. Soc. Jpn. **6**, 40 (1951).
[19] H. Hadwiger, Experientia **7**, 395 (1951).
[20] T. Boublík, Mol. Phys. **27**, 1415 (1974).
[21] P. Marienhagen, R. Hellmann, and J. Wagner, Phys. Rev. E **104**, 015308 (2021).
[22] G. Odriozola, J. Chem. Phys. **136**, 134505 (2012).
[23] G. Bautista-Carbajal, A. Moncho-Jordá, and G. Odriozola, J. Chem. Phys. **138**, 064501 (2013).
[24] G. Cinacchi and S. Torquato, J. Chem. Phys. **143**, 224506 (2015).
[25] G. Cinacchi and S. Torquato, Soft Matter **14**, 8205 (2018).
[26] G. Cinacchi and S. Torquato, Phys. Rev. E **100**, 062902 (2019).
[27] N. G. Almarza, J. Chem. Phys. **130**, 184106 (2009).
[28] N. Tasios and M. Dijkstra, J. Chem. Phys. **146**, 144901 (2017).
[29] P. Marienhagen and J. Wagner, Phys. Rev. E **105**, 014125 (2022).
[30] D. Vranek, J. Graph. Tools **7**, 23 (2002).
[31] See Supplemental Material at http://link.aps.org/supplemental/10.1103/PhysRevE.106.014101 for the determined equation-of-state data of hard lenses.
[32] N. F. Carnahan and K. E. Starling, J. Chem. Phys. **51**, 635 (1969).
[33] Y. Song, E. A. Mason, and R. M. Stratt, J. Phys. Chem. **93**, 6916 (1989).
[34] J. D. Parsons, Phys. Rev. A **19**, 1225 (1979).
[35] C. Vega, Mol. Phys. **92**, 651 (1997).
[36] E. Herold, R. Hellmann, and J. Wagner, J. Chem. Phys. **147**, 204102 (2017).

Supplemental Material

Equation of state of hard lenses: A combined virial series and simulation approach

Philipp Marienhagen and Joachim Wagner*
Institut für Chemie, Universität Rostock, 18051 Rostock, Germany

CLUSTER-MC DATA

Data for reduced pressure $\beta p r_{\mathrm{eq}}^3$, volume fraction φ and related real gas factors Z are compiled in the subsequent tables for all investigated aspect ratios.

TABLE S-1. Equation-of-state data for hard lenses with aspect ratios $\nu = 1/10$, $\nu = 1/8$, and $\nu = 1/6$ determined by cluster-MC simulations.

$\nu = 1/10$			$\nu = 1/8$			$\nu = 1/6$		
$\beta p r_{\mathrm{eq}}^3$	φ	Z	$\beta p r_{\mathrm{eq}}^3$	φ	Z	$\beta p r_{\mathrm{eq}}^3$	φ	Z
0.0868	0.0197379(10)	1.38616(7)	0.1669	0.0391317(15)	1.68362(7)	0.2036	0.0587742(29)	1.83433(9)
0.1534	0.0297628(7)	1.62460(4)	0.2534	0.0511836(29)	1.95430(11)	0.3023	0.074808(5)	2.13980(13)
0.2370	0.0396151(15)	1.88574(7)	0.3598	0.063154(4)	2.24892(13)	0.4249	0.090826(5)	2.47719(11)
0.3395	0.049367(3)	2.16772(15)	0.4884	0.075149(5)	2.56548(15)	0.5747	0.106932(5)	2.84589(13)
0.4629	0.059116(5)	2.46816(21)	0.6418	0.087287(6)	2.90247(19)	0.7555	0.123268(6)	3.24541(14)
0.6093	0.068971(4)	2.78458(13)	0.8224	0.099708(6)	3.25591(20)	0.9713	0.139982(6)	3.67424(15)
0.7808	0.079064(5)	3.11285(18)	1.0331	0.112580(7)	3.62240(21)	1.2266	0.157252(10)	4.13040(24)
0.9795	0.089550(6)	3.44773(21)	1.2765	0.126103(6)	3.99588(18)	1.5260	0.175298(17)	4.6096(5)
1.2077	0.100633(6)	3.78282(21)	1.5557	0.140564(9)	4.36886(26)	1.8746	0.194509(19)	5.1033(5)
1.4675	0.112584(9)	4.1086(4)	1.7554	0.150568(15)	4.6022(5)	2.0701	0.204936(24)	5.3488(7)
1.6292	0.119883(13)	4.2836(5)	1.8735	0.156494(23)	4.7258(7)	2.2778	0.21679(11)	5.5638(28)
1.7613	0.125874(9)	4.4105(4)	2.0504	0.16577(4)	4.8826(12)	2.3728	0.2291(5)	5.485(12)
1.9287	0.13377(4)	4.5447(11)	2.1364	0.17179(21)	4.909(6)	2.5080	0.24507(14)	5.419(3)
2.0088	0.13801(7)	4.5881(23)	2.2330	0.18790(15)	4.691(4)	2.6489	0.25598(6)	5.4796(12)
2.0911	0.1486(5)	4.436(14)	2.3467	0.19854(8)	4.6658(18)	2.7416	0.26219(7)	5.5369(14)
2.2623	0.16692(4)	4.2721(10)	2.4891	0.20901(9)	4.7010(20)	2.9482	0.27456(7)	5.6859(13)
2.6320	0.19016(5)	4.3627(12)	2.6374	0.21844(5)	4.7662(11)	3.2719	0.29132(7)	5.9472(14)
3.0396	0.21075(5)	4.5461(10)	2.8092	0.22825(5)	4.8584(11)			
3.4870	0.23028(5)	4.7730(9)						

* joachim.wagner@uni-rostock.de

TABLE S-2. Equation-of-state data for hard lenses with aspect ratios $\nu = 1/5$, $\nu = 1/4$, and $\nu = 1/3$ determined by cluster-MC simulations.

$\nu = 1/5$			$\nu = 1/4$			$\nu = 1/3$		
$\beta p r_{\mathrm{eq}}^3$	φ	Z	$\beta p r_{\mathrm{eq}}^3$	φ	Z	$\beta p r_{\mathrm{eq}}^3$	φ	Z
0.1212	0.0494301(15)	1.56114(5)	0.0904	0.0496942(15)	1.45850(5)	0.0626	0.0498617(28)	1.36196(8)
0.2471	0.0784254(26)	2.00608(7)	0.2571	0.098426(6)	2.09429(11)	0.2464	0.123747(5)	2.16005(9)
0.3575	0.097170(4)	2.34249(9)	0.3784	0.122195(7)	2.48281(15)	0.3654	0.153071(8)	2.58961(14)
0.4950	0.115951(6)	2.71810(12)	0.5330	0.145957(7)	2.92784(14)	0.5209	0.182378(10)	3.09840(18)
0.6637	0.134852(6)	3.13363(14)	0.7279	0.169854(9)	3.43591(17)	0.7223	0.211706(10)	3.70120(18)
0.8687	0.154029(7)	3.59087(16)	0.9709	0.193974(10)	4.01307(20)	0.9813	0.241115(13)	4.41504(24)
1.1154	0.173595(10)	4.09097(24)	1.2716	0.218437(8)	4.66734(18)	1.3125	0.270649(11)	5.26078(22)
1.4098	0.193718(9)	4.63361(21)	1.6408	0.243367(14)	5.4055(3)	1.7347	0.300377(9)	6.26490(18)
1.7586	0.214620(14)	5.2171(4)	2.0916	0.269091(15)	6.2320(4)	2.2714	0.330426(13)	7.45722(29)
2.1693	0.236916(29)	5.8299(8)	2.3725	0.283535(24)	6.7088(6)	2.9533	0.361290(16)	8.8677(4)
2.3726	0.24788(6)	6.0942(14)	2.6392	0.29683(4)	7.1287(9)	3.3605	0.377527(29)	9.6564(8)
2.5096	0.2576(5)	6.203(11)	2.8583	0.3101(5)	7.391(11)	3.5985	0.38683(10)	10.0915(24)
2.6503	0.27660(18)	6.101(4)	2.9919	0.32574(25)	7.364(6)	3.8197	0.3992(6)	10.380(15)
2.9005	0.29534(7)	6.2529(13)	3.1308	0.33643(10)	7.4612(22)	3.9854	0.41124(24)	10.513(7)
3.2107	0.313097(18)	6.5291(4)	3.3019	0.34692(8)	7.6310(16)	4.1580	0.42043(17)	10.729(5)
3.5163	0.32792(5)	6.8274(11)	3.6771	0.36570(7)	8.0617(15)	4.5247	0.43572(8)	11.2651(19)
3.8608	0.34261(4)	7.1748(7)	4.1012	0.38332(6)	8.5783(12)	4.9223	0.44941(5)	11.8817(13)
			4.4542	0.39614(7)	9.0150(16)	5.3535	0.46226(7)	12.5635(18)
			5.0625	0.41540(5)	9.7710(12)	5.8214	0.47457(4)	13.3071(11)
						6.3293	0.48651(6)	14.1130(17)

TABLE S-3. Equation-of-state data for hard lenses with aspect ratios $\nu = 1/2$ and $\nu = 2/3$ determined by cluster-MC simulations.

$\nu = 1/2$			$\nu = 2/3$		
$\beta p r_{\rm eq}^3$	φ	Z	$\beta p r_{\rm eq}^3$	φ	Z
0.0375	0.0499836(27)	1.27669(7)	0.0258	0.0499350(17)	1.24321(5)
0.0963	0.099784(6)	1.64228(9)	0.0648	0.0999078(26)	1.56065(4)
0.2348	0.169250(6)	2.36076(8)	0.1231	0.149837(10)	1.97684(13)
0.3072	0.193997(11)	2.69469(15)	0.1992	0.194614(8)	2.46290(10)
0.3959	0.218722(7)	3.08018(10)	0.2588	0.221163(10)	2.81567(12)
0.5044	0.243422(9)	3.52613(12)	0.3323	0.247702(8)	3.22798(10)
0.6371	0.268131(12)	4.04337(18)	0.4229	0.274229(15)	3.71069(21)
0.7993	0.292843(9)	4.64469(15)	0.5348	0.300735(15)	4.27895(22)
0.9977	0.317546(11)	5.34656(18)	0.6734	0.327277(16)	4.95093(24)
1.2407	0.342281(18)	6.1683(4)	0.8454	0.353828(18)	5.74909(29)
1.5388	0.367022(13)	7.13464(24)	1.0595	0.380373(21)	6.7023(4)
1.9055	0.391793(23)	8.2763(5)	1.3273	0.406947(16)	7.84804(29)
2.358 0	0.416573(20)	9.6324(5)	1.6638	0.433528(23)	9.2345(5)
2.9186	0.441345(12)	11.2533(4)	2.0893	0.460141(22)	10.9254(6)
3.6164	0.466114(16)	13.2028(5)	2.6307	0.486731(22)	13.0050(6)
4.4898	0.490844(11)	15.56562(29)	3.3255	0.513398(28)	15.5859(9)
5.5904	0.51551(4)	18.4537(13)	4.2251	0.54015(4)	18.8216(12)
6.9877	0.54023(6)	22.0110(22)	5.4026	0.56722(5)	22.9181(18)
8.0070	0.55542(11)	24.532(5)	6.3250	0.58445(5)	26.0402(19)
8.7770	0.5663(6)	26.375(25)	6.9630	0.59495(8)	28.161(4)
9.6320	0.5864(5)	27.952(24)	7.6760	0.60544(13)	30.507(7)
			8.4750	0.61601(12)	33.104(7)
			9.3710	0.62664(28)	35.983(16)

TABLE S-4. Equation-of-state data for hard lenses with aspect ratios $\nu = 4/5$ and $\nu = 10/11$ determined by cluster-MC simulations.

$\nu = 4/5$			$\nu = 10/11$		
$\beta p r_{\rm eq}^3$	φ	Z	$\beta p r_{\rm eq}^3$	φ	Z
0.0202	0.0499909(18)	1.23220(5)	0.0169	0.0500912(26)	1.22884(7)
0.0503	0.100023(5)	1.53351(8)	0.0418	0.099940(4)	1.52336(6)
0.0947	0.149930(6)	1.92611(8)	0.0786	0.149982(4)	1.90877(5)
0.1941	0.219733(6)	2.69370(8)	0.1325	0.199879(11)	2.41445(13)
0.2438	0.244194(10)	3.04452(12)	0.2116	0.249739(8)	3.08601(10)
0.3040	0.268676(10)	3.45036(12)	0.2550	0.270634(9)	3.43185(12)
0.3770	0.293155(15)	3.92160(20)	0.3060	0.291481(13)	3.82367(17)
0.4657	0.317649(10)	4.47073(14)	0.3663	0.312389(13)	4.27082(18)
0.5736	0.342127(11)	5.11260(16)	0.4374	0.333254(15)	4.78050(21)
0.7054	0.366622(11)	5.86728(17)	0.5217	0.354158(12)	5.36529(18)
0.8670	0.391156(17)	6.75911(28)	0.6217	0.375042(11)	6.03769(17)
1.0658	0.415685(20)	7.8186(4)	0.7407	0.395942(15)	6.81365(25)
1.3115	0.440242(12)	9.08441(25)	0.8829	0.416885(13)	7.71373(24)
1.6171	0.464819(24)	10.6089(7)	1.0532	0.437839(19)	8.7613(4)
1.9992	0.489448(29)	12.4558(8)	1.2581	0.45880(4)	9.9877(8)
2.2790	0.504454(19)	13.7766(6)	1.5058	0.479760(24)	11.4317(7)
2.4900	0.514520(24)	14.7576(7)	1.6420	0.489757(28)	12.2113(8)
2.7230	0.52456(4)	15.8298(11)	1.7920	0.49979(4)	13.0593(9)
			1.9570	0.50977(4)	13.9824(12)

Bibliography

[1] C. C. Ho, A. Keller, J. A. Odell, and R. H. Ottewill, Colloid Polym. Sci. **271**, 469 (1993).

[2] M. Ozaki, S. Kratohvil, and E. Matijević, J. Colloid Interface Sci. **102**, 146 (1984).

[3] A. Kuijk, A. van Blaaderen, and A. Imhof, J. Am. Chem. Soc. **133**, 2346 (2011).

[4] P. M. Johnson, C. M. van Kats, and A. van Blaaderen, Langmuir **21**, 11510 (2005).

[5] S. C. Glotzer and M. J. Solomon, Nat. Mater. **6**, 557 (2007).

[6] K. J. Lee, J. Yoon, and J. Lahann, Curr. Opin. Colloid Interface Sci. **16**, 195 (2011).

[7] D. Zerrouki, J. Baudry, D. Pine, P. Chaikin, and J. Bibette, Nature **455**, 380 (2008).

[8] L. Onsager, Ann. NY Acad. Sci. **51**, 627 (1949).

[9] N. Metropolis, A. W. Rosenbluth, M. N. Rosenbluth, A. H. Teller, and E. Teller, J. Chem. Phys. **21**, 1087 (1953).

[10] M. N. Rosenbluth and A. W. Rosenbluth, J. Chem. Phys. **22**, 881 (1954).

[11] J. Vieillard-Baron, J. Chem. Phys. **56**, 4729 (1972).

[12] D. Frenkel and R. Eppenga, Phys. Rev. Lett. **49**, 1089 (1982).

[13] D. Frenkel, B. M. Mulder, and J. P. McTague, Phys. Rev. Lett. **52**, 287 (1984).

[14] D. Frenkel, Phys. World **6**, 24 (1993).

[15] J. Zhu, M. Li, R. Rogers, W. Meyer, R. H. Ottewill, STS-73 Space Shuttle Crew, W. B. Russel, and P. M. Chaikin, Nature **387**, 883 (1997).

[16] Z. Cheng, P. M. Chaikin, J. Zhu, W. B. Russel, and W. V. Meyer, Phys. Rev. Lett. **88**, 015501 (2001).

[17] Z. Cheng, P. M. Chaikin, W. B. Russel, W. V. Meyer, J. Zhu, R. B. Rogers, and R. H. Ottewill, Mater. Des. **22**, 529 (2001).

[18] M. Voggenreiter, J. Roller, J. Geiger, L. Ebner, A. Zumbusch, and J.-M. Meijer, Langmuir **36**, 13087 (2020).

[19] J. Roller, J. D. Geiger, M. Voggenreiter, J.-M. Meijer, and A. Zumbusch, Soft Matter **16**, 1021 (2020).

[20] J. Roller, A. Laganapan, J.-M. Meijer, M. Fuchs, and A. Zumbusch, Proc. Natl. Acad. Sci. U.S.A. **118**, e2018072118 (2021).

[21] D. Frenkel, B. M. Mulder, and J. P. McTague, Mol. Cryst. Liq. Cryst. **123**, 119 (1985).

[22] D. Frenkel and B. M. Mulder, Mol. Phys. **55**, 1171 (1985).

[23] B. M. Mulder and D. Frenkel, Mol. Phys. **55**, 1193 (1985).

[24] S.-D. Lee, J. Chem. Phys. **89**, 7036 (1988).

[25] M. P. Allen, Liq. Cryst. **8**, 499 (1990).

[26] B. Tjipto-Margo and G. T. Evans, J. Chem. Phys. **93**, 4254 (1990).

[27] M. P. Allen and C. P. Mason, Mol. Phys. **86**, 467 (1995).

[28] P. J. Camp, C. P. Mason, M. P. Allen, A. A. Khare, and D. A. Kofke, J. Chem. Phys. **105**, 2837 (1996).

[29] P. J. Camp and M. P. Allen, J. Chem. Phys. **106**, 6681 (1997).

[30] J. Vieillard-Baron, Mol. Phys. **28**, 809 (1974).

[31] P. A. Monson and M. Rigby, Mol. Phys. **35**, 1337 (1978).

[32] I. Nezbeda and T. Boublík, Czech. J. Phys. B **28**, 353 (1978).

[33] D. Frenkel, J. Phys. Chem. **91**, 4912 (1987).

[34] M. Francová, J. Kolafa, P. Morávek, S. Labík, and A. Malijevský, Collect. Czech. Chem. Commun. **73**, 413 (2008).

[35] P. Morávek, J. Kolafa, and M. Francová, Collect. Czech. Chem. Commun. **73**, 459 (2008).

[36] J. A. C. Veerman and D. Frenkel, Phys. Rev. A **41**, 3237 (1990).

[37] S. C. McGrother, D. C. Williamson, and G. Jackson, J. Chem. Phys. **104**, 6755 (1996).

[38] P. Bolhuis and D. Frenkel, J. Chem. Phys. **106**, 666 (1997).

[39] A. Donev, I. Cisse, D. Sachs, E. A. Variano, F. H. Stillinger, R. Connelly, S. Torquato, and P. M. Chaikin, Science **303**, 990 (2004).

[40] A. Donev, F. H. Stillinger, P. M. Chaikin, and S. Torquato, Phys. Rev. Lett. **92**, 255506 (2004).

[41] W. Man, A. Donev, F. H. Stillinger, M. T. Sullivan, W. B. Russel, D. Heeger, S. Inati, S. Torquato, and P. M. Chaikin, Phys. Rev. Lett. **94**, 198001 (2005).

[42] P. Pfleiderer and T. Schilling, Phys. Rev. E **75**, 020402 (2007).

[43] M. Radu, P. Pfleiderer, and T. Schilling, J. Chem. Phys. **131**, 164513 (2009).

[44] G. Odriozola and F. de J. Guevara-Rodríguez, J. Chem. Phys. **134**, 201103 (2011).

[45] G. Odriozola, J. Chem. Phys. **136**, 134505 (2012).

[46] G. Bautista-Carbajal, A. Moncho-Jordá, and G. Odriozola, J. Chem. Phys. **138**, 064501 (2013).

[47] N. Clisby and B. M. McCoy, J. Stat. Phys. **122**, 15 (2006).

[48] R. J. Wheatley, Phys. Rev. Lett. **110**, 200601 (2013).

[49] M. Rigby, Mol. Phys. **66**, 1261 (1989).

[50] C. Vega, Mol. Phys. **92**, 651 (1997).

[51] X.-M. You, A. Y. Vlasov, and A. J. Masters, J. Chem. Phys. **123**, 034510 (2005).

[52] A. Y. Vlasov, X.-M. You, and A. J. Masters, Mol. Phys. **100**, 3313 (2002).

[53] S. Labík, J. Kolafa, and A. Malijevský, Phys. Rev. E **71**, 021105 (2005).

[54] N. F. Carnahan and K. E. Starling, J. Chem. Phys. **51**, 635 (1969).

[55] J. D. Parsons, Phys. Rev. A **19**, 1225 (1979).

[56] I. Nezbeda, Chem. Phys. Lett. **41**, 55 (1976).

[57] T. Boublík, Mol. Phys. **42**, 209 (1981).

[58] Y. Song and E. A. Mason, Phys. Rev. A **41**, 3121 (1990).

[59] C. McBride and E. Lomba, Fl. Phase Equilib. **255**, 37 (2007).

[60] G. Cinacchi and S. Torquato, J. Chem. Phys. **143**, 224506 (2015).

[61] G. Cinacchi and S. Torquato, Soft Matter **14**, 8205 (2018).

[62] G. Cinacchi and S. Torquato, Phys. Rev. E **100**, 062902 (2019).

[63] E. Herold, R. Hellmann, and J. Wagner, J. Chem. Phys. **147**, 204102 (2017).

[64] J. K. Singh and D. A. Kofke, Phys. Rev. Lett. **92**, 220601 (2004).

[65] N. G. Almarza, J. Chem. Phys. **130**, 184106 (2009).

[66] P. Marienhagen, R. Hellmann, and J. Wagner, Phys. Rev. E **104**, 015308 (2021).

[67] P. Marienhagen and J. Wagner, Phys. Rev. E **105**, 014125 (2022).

[68] P. Marienhagen and J. Wagner, Phys. Rev. E **106**, 014101 (2022).

[69] M. Kulossa, P. Marienhagen, and J. Wagner, Phys. Rev. E **105**, 064121 (2022).

[70] H. Kamerlingh Onnes, Proc. K. Ned. Akad. Wet. **4**, 125 (1902).

[71] J. E. Mayer, J. Chem. Phys. **5**, 67 (1937).

[72] M. Born, Physica **4**, 1034 (1937).

[73] F. H. Ree and W. G. Hoover, J. Chem. Phys. **40**, 939 (1964).

[74] F. H. Ree and W. G. Hoover, J. Chem. Phys. **41**, 1635 (1964).

[75] F. H. Ree and W. G. Hoover, J. Chem. Phys. **46**, 4181 (1967).

[76] C. Zhang and B. Montgomery Pettitt, Mol. Phys. **112**, 1427 (2014).

[77] R. Hellmann and E. Bich, J. Chem. Phys. **135**, 084117 (2011).

[78] J. J. van Laar, Amsterdam Akad. Versl. **7**, 350 (1899).

[79] N. Clisby and B. M. McCoy, J. Stat. Phys. **114**, 1343 (2004).

[80] I. Lyberg, J. Stat. Phys. **119**, 747 (2005).

[81] A. Isihara, J. Chem. Phys. **18**, 1446 (1950).

[82] A. Isihara and T. Hayashida, J. Phys. Soc. Jpn. **6**, 40 (1951).

[83] A. Isihara and T. Hayashida, J. Phys. Soc. Jpn. **6**, 46 (1951).

[84] H. Hadwiger, Experientia **7**, 395 (1951).

[85] S. Rast, P. H. Fries, and H. Krienke, Mol. Phys. **96**, 1543 (1999).

[86] B. Jäger, R. Hellmann, E. Bich, and E. Vogel, J. Chem. Phys. **135**, 084308 (2011).

[87] K. M. Benjamin, J. K. Singh, A. J. Schultz, and D. A. Kofke, J. Phys. Chem. B **111**, 11463 (2007).

[88] A. Donev, S. Torquato, and F. H. Stillinger, J. Comput. Phys. **202**, 737 (2005).

[89] A. Donev, S. Torquato, and F. H. Stillinger, J. Comput. Phys. **202**, 765 (2005).

[90] G. Odriozola, J. Chem. Phys. **131**, 144107 (2009).

[91] N. G. Almarza and E. Lomba, J. Chem. Phys. **127**, 084116 (2007).

[92] N. Tasios and M. Dijkstra, J. Chem. Phys. **146**, 144901 (2017).

[93] E. P. Bernard, W. Krauth, and D. B. Wilson, Phys. Rev. E **80**, 056704 (2009).

[94] M. Engel, J. A. Anderson, S. C. Glotzer, M. Isobe, E. P. Bernard, and W. Krauth, Phys. Rev. E **87**, 042134 (2013).

[95] M. Isobe and W. Krauth, J. Chem. Phys. **143**, 084509 (2015).

[96] A. Donev, A. L. Garcia, and B. J. Alder, J. Comput. Phys. **227**, 2644 (2008).

[97] S. M. Woodley and R. Catlow, Nat. Mater. **7**, 937 (2008).

[98] J. de Graaf, L. Filion, M. Marechal, R. van Roij, and M. Dijkstra, J. Chem. Phys. **137**, 214101 (2012).

[99] D. Gottwald, G. Kahl, and C. N. Likos, J. Chem. Phys. **122**, 204503 (2005).

[100] E. A. Guggenheim, J. Chem. Phys. **7**, 103 (1939).

[101] K.-K. Han and H. S. Son, J. Chem. Phys. **115**, 7793 (2001).

[102] P. Ströker, R. Hellmann, and K. Meier, Phys. Rev. E **103**, 023305 (2021).

[103] M. P. Allen and D. J. Tildesley, *Computer Simulation of Liquids* (Oxford University Press, New York, 1987).

[104] D. Frenkel and B. Smit, *Understanding Molecular Simulation: From Algorithms to Applications* (Elsevier, San Diego, 2001).

[105] R. H. Swendsen and J.-S. Wang, Phys. Rev. Lett. **58**, 86 (1987).

[106] L. Verlet, Phys. Rev. **159**, 98 (1967).

[107] B. Quentrec and C. Brot, J. Comput. Phys. **13**, 430 (1973).

[108] C. Vega and E. G. Noya, J. Chem. Phys. **127**, 154113 (2007).

[109] P. J. Steinhardt, D. R. Nelson, and M. Ronchetti, Phys. Rev. Lett. **47**, 1297 (1981).

[110] H. Liu, Mol. Phys. **119**, e1886364 (2021).

[111] A. Mulero, C. Galán, and F. Cuadros, Phys. Chem. Chem. Phys. **3**, 4991 (2001).

[112] J. Kolafa, S. Labík, and A. Malijevský, Phys. Chem. Chem. Phys. **6**, 2335 (2004).

[113] J. Wu and Z. Li, Annu. Rev. Phys. Chem. **58**, 85 (2007).

[114] H. Hansen-Goos and K. Mecke, J. Phys.: Condens. Matter **22**, 364107 (2010).

[115] J. W. Perram and M. S. Wertheim, J. Comput. Phys. **58**, 409 (1985).

[116] W. H. Press, S. A. Teukolsky, W. T. Vetterling, and B. P. Flannery, *Numerical recipes in C* (Press Syndicate of the University of Cambridge, Cambridge, 1992).

[117] L. Paramonov and S. N. Yaliraki, J. Chem. Phys. **123**, 194111 (2005).

[118] D. Vranek, J. Graph. Tools **7**, 23 (2002).

[119] A. J. Schultz and D. A. Kofke, Phys. Rev. E **90**, 023301 (2014).

[120] F. H. Ree and W. G. Hoover, J. Chem. Phys. **40**, 2048 (1964).

[121] N. Clisby and B. M. McCoy, Pramana **64**, 775 (2005).

[122] C. Vega and S. Lago, Comput. Chem. **18**, 55 (1994).

[123] A. Perez-Gracia and F. Thomas, Adv. Appl. Clifford Alg. **27**, 523 (2017).

[124] S. Torquato and Y. Jiao, Phys. Rev. E **87**, 022111 (2013).

[125] T. Boublík, Mol. Phys. **27**, 1415 (1974).

[126] E. G. Noya, C. Vega, and E. de Miguel, J. Chem. Phys. **128**, 154507 (2008).

[127] R. Eppenga and D. Frenkel, Mol. Phys. **52**, 1303 (1984).

List of Symbols and Notation

Mathematical notation

a	scalar variable
$\underline{\mathbf{a}}$	vector
$\underline{\hat{\mathbf{a}}}$	unit vector
$\mathbf{A}$	matrix

Greek symbols

α	scaled excess part of excluded volume
β	inverse thermal energy
Δ_{rot}	maximum rotation angle
δ	cutoff distance
γ	integrand
γ_{ref}	reference integrand
γ_0	parameter of generalised Carnahan-Starling relation
γ_1	parameter of generalised Carnahan-Starling relation
γ_2	parameter of generalised Carnahan-Starling relation
θ	$3D$ angular coordinate
ϑ	$4D$ angular coordinate
ϑ_c	aperture of critical cone
ϑ_{r}	$4D$ angular coordinate of randomly orientated unit vector
Λ	thermal de Broglie wavelength
λ	variable parameter for spherocylinder
λ_{min}	parameter for spherocylinder with minimum distance
μ	variable parameter for spherocylinder
μ_{min}	parameter for spherocylinder with minimum distance
ν	aspect ratio
π	mathematical constant π
π	sampling distribution
π_{new}	new sampling distribution
π_{old}	old sampling distribution
$\pi(x'\|x)$	transition probability from x to x'
ϱ	particle number density
σ	closest surface distance
σ_{ij}	closest surface distance between particles i and j
σ_{ll}	lower limit for closest surface distance
σ_{ul}	upper limit for closest surface distance
ϕ	$3D$ angular coordinate
φ	volume fraction
φ	$4D$ angular coordinate
φ_{max}	maximum volume fraction
φ_{r}	$4D$ angular coordinate of randomly orientated unit vector
χ	$4D$ angular coordinate
χ_c	specific cluster realisation

χ_r	$4D$ angular coordinate of randomly orientated unit vector
$\mathbf{\Psi}$	rotation matrix
ψ	rotation angle
$\underline{\mathbf{\Omega}}$	angular coordinates
$\underline{\mathbf{\Omega}}_N$	angular coordinates of unit vector at step N
$\underline{\mathbf{\Omega}}_\mathrm{r}$	angular coordinates of randomly orientated unit vector
ω	proposal probability
ω_c	cluster probability
ω_V	volume change proposal probability

Latin symbols

$\mathbf{A}$	shape matrix of ellipsoid A
A	arbitrary observable
a	element of Hamilton quaternion
$a_{0,i}$	polynomial expansion coefficient
$a_{1,i}$	polynomial expansion coefficient
$a_{2,i}$	polynomial expansion coefficient
$\mathbf{B}$	shape matrix of ellipsoid B
B_i	virial coefficient of order i
B_i^*	virial coefficient of order i reduced by power of particle volume
$\tilde{B}_i$	virial coefficient of order i reduced by power of B_2
$B_i^{*,\mathrm{CS}}$	Carnahan Starling reduced virial coefficient of order i
$B_2^{*,(\mathrm{HS})}$	reduced second virial coefficient of a hard sphere
$B_{2,\mathrm{ana}}^*$	analytical value for reduced second virial coefficient
b	bond probability function
b	element of Hamilton quaternion
$\underline{\mathbf{c}}_i$	center of mass of particle i
c	element of Hamilton quaternion
c_G	Ree-Hoover star content of graph G
D	dimension
d	element of Hamilton quaternion
d	distance between centres of generating spheres
e_{ij}	e-function of Ree-Hoover graph for particles i and j
F	free energy
f_{ij}	Mayer f-function of particles i and j
G	free enthalpy
G	graph
$\mathbf{H}$	transformation matrix
$\mathcal{H}$	Hamiltonian
h	Planck's constant
$\mathbf{I}$	identity matrix
I_ref	reference integral
$I_{i,\mathrm{ref}}$	reference integral of order i
i	order of virial coefficient

i	index
j	index
$\underline{\mathbf{K}}_i$	centre of most distant generating sphere of lens i
$\underline{\mathbf{K}}_j$	centre of most distant generating sphere of lens j
$\mathcal{K}$	kinetic contribution to Hamiltonian $\mathcal{H}$
k_B	Boltzmann's constant
l	order of spherical harmonic or bond order parameter
$\mathbb{M}_i^\mathrm{L}$	set of labelled Mayer graphs of order i
$\mathbb{M}_i^\mathrm{U}$	set of unlabelled Mayer graphs of order i
m	mass
N	number of particles
$\tilde{N}$	apparent number of particles
N_b	number of cluster bonds
N_T	number of trees, cardinality of topological class of trees
$\mathcal{N}$	probability of system
n_e	number of e-bonds
n_f	number of f-bonds
P_Acc	acceptance probability
$\underline{\mathbf{p}}$	momentum
p	pressure
p	probability density function
$p_{N,p,T}$	normalised probability of the isobaric-isothermal ensemble
$p_{N,V,T}$	normalised probability of the canonical ensemble
Q_l	bond order parameter of order l
$Q_{N,p,T}$	partition function of the isobaric-isothermal ensemble
$Q_{N,V,T}$	partition function of the canonical ensemble
$\mathbf{R}$	rotation matrix
$\tilde{R}_\mathrm{P}$	mean radius of curvature of particle
R_0	radius of generating sphere
$\mathbb{R}^D$	D-dimensional Euclidean space
$\mathbb{R}_i^\mathrm{L}$	set of labelled Ree-Hoover graphs of order i
$\mathbb{R}_i^\mathrm{U}$	set of unlabelled Ree-Hoover graphs of order i
$\underline{\mathbf{r}}$	Cartesian coordinate
$\underline{\mathbf{r}}_1$	line segment 1
$\underline{\mathbf{r}}_2$	line segment 2
$\underline{\mathbf{r}}_i$	position vector of particle i
$\underline{\mathbf{r}}_{ij}$	center-of-mass distance vector from particle i to particle j
r	radius of sphere
r_c	contact distance
r_eq	equatorial radius
S	entropy
S_2	nematic order parameters of order 2
S_4	nematic order parameters of order 4
S_G	integral of graph G

S_P	surface area of particle
$\underline{\mathbf{s}}$	reduced coordinate
T	temperature
U	potential
$\mathcal{U}$	contribution of potential to Hamiltonian
$\mathcal{U}^{(i)}$	contribution of i-particle potential to Hamiltonian $\mathcal{H}$
$\mathcal{U}_{ij}$	contribution of potential between i and j to Hamiltonian $\mathcal{H}$
$\underline{\hat{\mathbf{u}}}_i$	orientation vector of particle i
$\underline{\hat{\mathbf{u}}}_j$	orientation vector of particle j
$\underline{\hat{\mathbf{u}}}_N$	orientation unit vector at step N
$\underline{\hat{\mathbf{u}}}_{N+1}$	orientation unit vector at step $N+1$
$\underline{\hat{\mathbf{u}}}_\mathrm{r}$	randomly orientated unit vector
V	system volume
V_P	particle volume
x_i	inner product i
$Y_{l,m}$	spherical harmonic of order l, m
Z	real gas factor
Z^CS	Carnahan Starling real gas factor
$Z_{N,p,T}$	configuration integral of isobaric-isothermal ensemble
$Z_{N,V,T}$	configuration integral of canonical ensemble

List of Figures

List of Tables

Acknowledgements

An dieser Stelle möchte ich mich bei allen Personen bedanken, die zum Gelingen dieser Arbeit beigetragen haben.
Ich bedanke mich bei Prof. Dr. Joachim Wagner für die Möglichkeit, unter seiner Betreuung eine Promotionsarbeit anzufertigen zu dürfen. Ich konnte in den vergangenen Jahren dank der sehr breit aufgestellten Ausbildung viele Sachen auch über die Grenzen der Wissenschaft hinaus erlernen. Besonders bedanken möchte ich mich für die mir gegebene wissenschaftliche Freiheit, das mir entgegengebrachte Vertrauen und die vielen hilfreichen Diskussionen.
Ich möchte mich bei den Gutachtern bedanken für die investierte Zeit und die Bereitschaft, sich mit meiner Arbeit auseinanderzusetzen.
Für die finanzielle Unterstützung im Rahmen des Promotionsstipendienprogramms "Unsere Besten promovieren in Rostock" möchte ich mich bei der Universität Rostock bedanken.
Meinen Koauthoren Robert Hellmann und Markus Kulossa gilt mein Dank für die fruchtbare Zusammenarbeit.
Ich bedanke mich bei meinem langjährigen Bürokollegen Joel Diaz Maier für die vielen anregenden und hilfreichen Gespräche. Auch bei den aktuellen und ehemaligen Mitgliedern der Arbeitsgruppe Wagner, insbesondere Nele Leopold, Paul Tümmler und Daniel Weidig möchte ich mich unter anderem für die angenehme Arbeitsatmosphäre bedanken.
Abschließend möchte ich mich bei meiner Familie und meinen Freunden für die Geduld und Unterstützung in den vergangenen Jahren bedanken.

Declaration of Authorship

Ich versichere hiermit an Eides statt, dass ich die vorliegende Arbeit selbstständig angefertigt und ohne fremde Hilfe verfasst habe. Dazu habe ich keine außer den von mir angegebenen Hilfsmitteln und Quellen verwendet und die den benutzten Werken inhaltlich und wörtlich entnommenen Stellen habe ich als solche kenntlich gemacht.

_____

Philipp Marienhagen
Rostock, 16.03.2022